Beyond the common view of Bi cuprates: Exploiting matrix element effects in XAS and ARPES

D I S S E R T A T I O N

zur Erlangung des akademischen Grades

doctor rerum naturalium
(Dr. rer. nat.)
im Fach Physik

eingereicht an der
Mathematisch-Naturwissenschaftlichen Fakultät I
Humboldt-Universität zu Berlin

von
Frau Dipl.-Phys. Beate Müller

Abstract

In this PhD work the electronic structure of Bi cuprates from the normal state down to the superconducting state is investigated. The normal state electronic structure is probed by polarization dependent x-ray absorption spectroscopy (XAS) on single layer Bi cuprates. With the x-ray beam being incident normal to the CuO_2 plane the azimuthal angle was varied to explore the polarization effects on orbitals within the plane. In the CuL_3- as well as the OK-edge spectra, the spectral features related to the doped holes showed a distinct polarization dependence which probably became observable through the inhomogeneities present in this system. The revealed polarization dependence is more complex than expected from hybridization of $Cu3d_{x^2-y^2}$ and $O2p_{x,y}$ orbitals only. Thus, the results support the inclusion of out-of-plane orbitals into the description of the electronic structure as has been previously theoretically proposed. Furthermore, the implications of the results on the electronic structure are discussed. The obtained XAS spectra can be interpreted within the charge-transfer picture. However, the charge transfer gap has been observed to rise with rising hole concentration which supports theories of the instability of Zhang-Rice-singlets in the overdoped regime.

By angle resolved photoemission (ARPES) the excitations close to the Fermi surface in the antinodal region of double layer Bi cuprates have been investigated. The complex lineshape in double layer Bi cuprates that results from interlayer effects has been disentangled by exploiting matrix element effects. In combination with distinct polarization settings this enabled to unify seemingly inconsistent observations made on single and double layer Bi cuprates. The existence of an excitation additional to antibonding and bonding band could be shown in the double layer Bi cuprate. This additional excitation is probably connected to the antibonding band. It furthermore shows similarities to the sharp peak observed in single layer Bi cuprates. It persists to temperatures above the superconducting temperature T_c, and presumably vanishes at or above the pseudogap temperature T^*. The ARPES results could be best explained within the model of electronic inhomogeneity which derives superconductivity from stripes.

Zusammenfassung

Die vorliegende Arbeit befasst sich mit der elektronischen Struktur von Bi-Kupraten vom Normalzustand bis in den supraleitenden Zustand. Der Normalzustand von einschichtigen Bi-Kupraten wurde mittels polarisationsabhängiger Röntgenabsorptionsspektroskopie untersucht. Dabei wurden die Röntgenphotonen senkrecht zur Probennormale, und damit auch senkrecht zur CuO_2-Ebene eingestrahlt, und der azimuthale Winkel variiert, um Polarisationseffekte innerhalb der Ebene zu erforschen. Die Absorptionsspektren der CuL_3- und OK-Kante zeigen deutlich eine Polarisationsabhängigkeit in den Merkmalen, die den dotierten Löchern zugeordnet werden. Diese Polarisationsabhängigkeit innerhalb der CuO_2-Ebene wird wahrscheinlich durch Inhomogenitäten, die für Bi-Kuprate typisch sind, beobachtbar. Die Winkelabhängigkeit dieser Polarisationsabhängigkeit geht über die erwartete Hybridisierung von $Cu3d_{x^2-y^2}$- und $O2p_{x,y}$-Orbitalen hinaus. Die Resultate unterstützen also Theorien, die auch Orbitale ausserhalb der CuO_2-Ebene zur Beschreibung der elektronischen Struktur einbeziehen. Desweiteren werden Schlussfolgerungen für die elektronische Struktur diskutiert. Die XAS Spektren lassen sich innerhalb der Theorie zum Ladungs-Transfer-Isolator interpretieren. Allerdings wurde auch beobachtet, dass die Ladungs-Transfer-Lücke sich mit steigender Lochkonzentration vergrößert, was von Theorien zum Zusammenbruch der Zhang-Rice-Singuletts im überdotierten Bereich vorhergesagt wurde.

Mittels winkelaufgelöster Photoemission (ARPES) wurden die Anregungen nahe der Fermikante in antinodaler Richtung an zweischichtigen Bi-Kupraten untersucht. Die komplexe Linienform im zweischichtigen Bi-Kuprat, die aus Interlageneffekten resultiert, wurde durch die gezielte Ausnutzung von Matrixelementeffekten vereinfacht. Dadurch konnten, in Kombination mit der spezifischen Ausrichtung der Polarisation, vorherige, sich scheinbar widersprechende Beobachtungen am einschichtigen und zweischichtigen Bi-Kuprat in Einklang gebracht werden. Es konnte gezeigt werden, dass im zweischichtigen Bi-Kuprat eine Anregung zusätzlich zum bindenden und antibindenden Band existiert, welche mit dem antibindenden Band korreliert zu sein scheint. Außerdem zeigt es Gemeinsamkeiten mit dem scharfen Peak, der im einschichtigen Bi-Kuprat gefunden wurde. So besteht es über die supraleitende Sprungtemperatur T_c hinaus, und verschwindet vermutlich bei oder über der Pseudolücken-Temperatur T^*. Die ARPES Messungen lassen sich am Besten innerhalb des Modells elektronischer Inhomogenitäten erklären, welches Hochtemperatursupraleitung aus Streifen ableitet.

Contents

1

Introduction

One of the persisting problems in condensed matter physics is the explanation of high temperature superconductivity - even more than 20 years after its discovery[1]. Two central issues for solving high temperature superconductivity are the description of the electronic structure of the cuprates, especially the incorporation of their strong correlations, and most of all the mechanism of pairing.

However, by now, some views and experimental techniques have become common which led to omitting information that could possibly clarify the matter. Regarding the electronic structure the modeling with two-band Hamiltonians accounting only for in-plane Cu and oxygen orbitals has become a generally accepted fact, although there is experimental[2,3] and theoretical work[4–8], that emphasizes the importance of the surrounding of the CuO_2 plane. Furthermore, concerning the pairing mechanism proposed models have been, especially in ARPES, probed with similar experimental settings and on mostly the same material, the double layer Bi cuprate[9,10]. However, on single layer Bi cuprates contrary observations to those in the double layer have been reported[11,12]. For deriving a uniform picture of cuprates, material dependent features have to be discerned from those universal to all cuprates. In this vein, it would certainly be helpful to first coalesce the experimental observations within one cuprate family, namely the investigations on the single and double layer Bi cuprates.

Within this thesis the two questions raised above shall be investigated obtaining additional information by varying matrix elements. By polarization dependent x-ray absorption spectroscopy the unoccupied density of states and the orbital occupation within the CuO_2 plane is probed on a very local scale, looking at the in-plane polarization which has not been done so far. In angle resolved photoemission measurements, the complex lineshape of double layer Bi cuprates is disentangled by exploiting matrix element dependencies on photon energy, but also specific polarization settings. Thus, seemingly differing observations on the single and double layer Bi cuprate have been unified by the exploration of excitations additional to the commonly accepted ones.

The following introductory chapter intends to present the concepts of the physics of high-T_c cuprates that are by now generally accepted, but also, to indicate the challenges
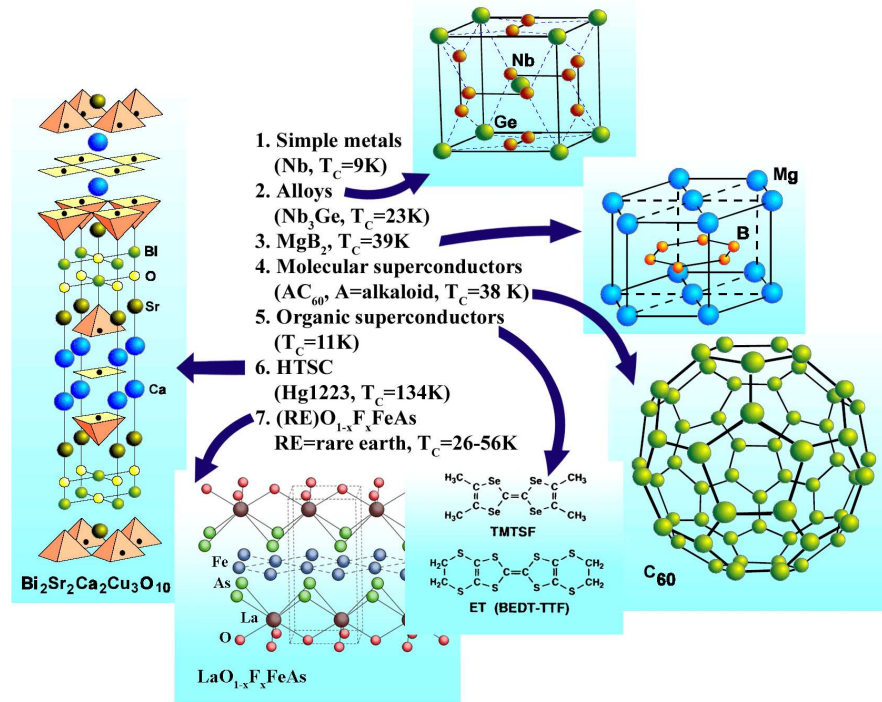
Figure 1.1: *The figure*[13] *shows the various families of superconductors each with the structure of one characteristic example and the highest T_c indicated. For details see the text.*

that these commonly agreed upon models still hold. First, the way from conventional to unconventional superconductivity is laid out following the route to high temperature superconductivity. Then, the unifying element of the high-T_c cuprates, the CuO_2 plane, is focused on regarding its electronic structure with emphasis on the physics of strong correlations. This will lead to the introduction of the general phase diagram of the cuprates. Finally, the most discussed models for the mechanism of high temperature superconductivity in cuprates are introduced. At the end of this chapter, the scope and layout of this thesis are specified.

1.1 From conventional to unconventional superconductivity

Superconductivity was first discovered in mercury by Kamerlingh Onnes[14] in 1911. This discovery was made possible by the ability to liquify Helium and thus reach temperatures in the very low Kelvin regime. Kamerlingh Onnes reported a sharp drop to zero in the resistivity at T≈4.3 K which could not be reconciled with the Drude theory of metals, where the resistivity drops continuously like T^5 down to ρ_0, the residual resistivity due to impurities. Meissner and Ochsenfeld[15] showed in 1933 that the superconductor differs from the ideal conductor in that the superconductor will expel an applied magnetic field when cooled below the superconducting transition temperature T_c regardless of the

field being applied before or after T_c is reached. Hence, superconductors are perfect diamagnets. The expulsion of the magnetic field was named Meissner-Ochsenfeld effect. With the latter it could be shown that the superconducting state is a true thermodynamic state and not just one of infinte conductance. Various metals and metallic alloys show so-called conventional superconductivity. The term refers to them being explained within the theory of Bardeen, Cooper and Schrieffer, the BCS theory[16]. The key ingredient to conventional superconductivity is the interaction of two electrons via a virtual phonon. This interaction creates a bound pair, the so-called Cooper pair. The initial idea was inspired by the isotope effect found in mercury by Maxwell[17] and Reynolds et al.[18] in 1950. Fröhlich then predicted that the electron phonon interaction is the key for the occurence of superconductivity[19]. Finally in 1957 the BCS theory provided an understanding of superconductivity and all its features on a microscopic level. Previous theories were phenomenological and only able to account for single effects. One of those theories is that of London and London[20] which describes the Meissner-Ochsenfeld effect by deriving equations for the electrodynamics of a superconductor. They concluded that the field is not expelled totally from within a superconductor. Instead the London penetration depths can be defined within which the field is reduced to zero exponentially. Another early phenomenological theory is that of Ginzburg and Landau[21]. They described superconductivity as a second order phase transition within the framework of the Landau theory of such phase transitions. Now the existence of type I and type II superconductors could be explained. While the first exhibit a pure Meissner phase, type II superconductors also show a Shubnikov phase with rising magnetic field, where the magnetic field penetrates the superconductor in vortices.

The most prominent superconductors are sketched in fig. 1.1. A variety of metals exhibit conventional superconductivity (Burns see e.g.[22], Buzea and Yamashita see e.g.[23], and references therein). Conventional meaning not only being well explained within BCS theory, but also: having a Fermi liquid-like normal state, high superfluid density, long coherence length, and no magnetic correlations. Also some metallic alloys are conventional superconductors. Although most, as e. g. the A-15 compounds sketched in the figure, show also some unconventional behavior, like their comparably high T_c, and the short coherence length. Nevertheless their pairing mechanism is phononic.

More promising for practical applications are MgB_2[24] and fullerenes, like C_{60}[25]. Both have a higher T_c than the materials discussed before. It is still under debate, if MgB_2 is a real exponent of conventional phonon-mediated BCS supercondutivity[23,26]. Also for C_{60} the mechanism of superconductivity is still disputed, although it is widely believed to be BCS-like pairing[26–28].

Also the Bechgaard (TMTSF) and organic (BEDT-TTF) salts shown in fig. 1.1 are highly unconventional. They are layered, quasi-two-dimensional materials. The electron transport, however, is one-dimensional. They exhibit magnetic correlations and low superfluid density.

In 1986, the most famous unconventional superconductors, the high-T_c cuprates, were discovered by Bednorz and Müller[1]. They are the only true high-T_c superconductors. For completeness it shall be mentioned here that there exist electron and hole doped cuprates. The electron doped cuprates exhibit some physical properties distinctly dif-

ferent to the hole doped cuprates and have a much lower T_c[29]. This thesis, however, will only deal with hole doped cuprates, and therefore the term cuprates will be used as refering to the hole doped materials, unless otherwise stated. There exist various cuprate families, all of which are layered compounds with one or more CuO_2 planes within one unit cell. The individual members of each family are called single, double and triple layer accordingly. T_c is higher in triple than in double, and in double than in single layers. However, adding more than three CuO_2 planes does in most cases not raise T_c any higher. Some widely known cuprate families and their T_c are shown in fig. 1.2.
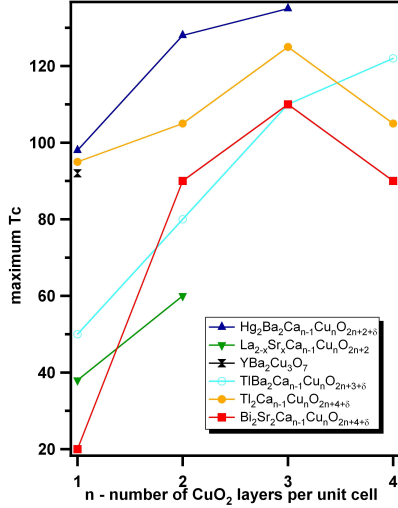

Figure 1.2: *Maximum superconducting transition temperature T_c^{max} over number of adjacent CuO_2 layers of different cuprate families.*[22,26]

The cuprates are unconventional in many respects. While the normal state of the conventional metallic superconductors can be well described within Fermi liquid theory, the cuprate parent compounds are antiferromagnetic insulators. This was suprising since in conventional superconductors any magnetically long-ranged ordered state was believed to be incompatible with superconductivity. When doping the cuprates with holes, the superconducting state arises. Even in doped cuprates, however, the normal state is a so-called bad metal state. Only with higher hole concentrations the cuprates begin to exhibit Fermi liquid like behavior in their normal state. Furthermore, the cuprates have a superconducting gap with d-wave symmetry, in contrast to the s-wave gap of conventional superconductors. Another up to now strongly debated and not understood characteristics is the opening of a gap above the superconducting transition temperature T_c. This so-called pseudogap exists only in the underdoped regime. This rich phase diagram, where superconductivity is only one phase with unusual properties, is outlined in general in section 1.2.3 of this chapter.

The mystery of superconductivity in the high-T_c cuprates has pushed forward solid state research. It has been a driving force for the development and advancement of novel experimental techniques as e.g. angle resolved photoemission spectroscopy (ARPES) and scanning tunneling microscopy (STM) and spectroscopy (STS), but also THz time-domain spectroscopy, IR ellipsometry etc. Furthermore, it has triggered new insights into the physics of strongly correlated electrons.

Finally, it shall be mentioned that another group of unconventional superconductors has been discovered recently, the pnictides[30]. They have some characteristics similar to the cuprates. They are layered iron arsenids with spacer layers in which substitution of atoms results in doping. Only doped compounds become superconducting within a certain range of dopants concentration. The parent compounds are antiferromagnets and doping destroys the magnetic order. However, they are not Mott insulators like the cuprates, but an antiferromagnetic "spin-density-wave" metal. Although there have

been a multidude of publications since the initial paper, it is yet too early to make definite statements about the mechanism of superconductivity other than that it is not conventional but also different from that in the cuprates[31]. The highest T_c reached so far has been 55 K reached in $SmFeAsO_{1-x}$[32].

1.2 The Cuprates

The most promising high-T_c candidate among the unconventional superconductors are the superconducting hole doped cuprates. The cuprates derive their name from the CuO_4 unit which is common to all of them. They can be systematized according to the organization of those CuO_4 units. Among them are one- and two-dimensional systems, as well as ladder systems. They all show interesting physics like e.g. the realization of one-dimensional quantum spin chains[33] or spin-Peierls behavior[34]. However, only the two-dimensional cuprates whose CuO_4 unit link their edges to form a CuO_2 plane as shown in fig. 1.3(a) exhibit high-T_c superconductivity. The CuO_2 plane is the most important ingredient for high-T_c behavior in those layered cuprate systems. It is surrounded by rare earth oxide layers. Each cuprate family has its own characteristic combination of those spacer layers which act as a charge reservoir. This last point will be more closely looked at when the doping mechanism is discussed. Here it shall only be noted that, in an ionic model, the CuO_2 plane has Cu^{2+} and O^{2-} and therefore accepts electrons which is true for the electron doped cuprates like for instance $Nd_{2-x}Ce_xCuO_{4+\delta}$ (NCCO)). In the hole doped cuprates, however, the arrangement of the spacer layers closest to the CuO_2 plane leads to a perovskite structure. This means that there exist apical oxygens in an octahedral coordination as illustrated in fig. 1.3(b). In hole doped cuprates with more than one CuO_2 plane per unit cell those CuO_2 planes are separated by an insulating layer like e.g. Ca in the multilayer Bi cuprates. Then the CuO_6 octaheder reduces to a CuO_5 unit with one apical oxygen (see fig. 1.3(c)). In the ionic picture from above, both, the CuO_5 and the CuO_6 unit are more negative than the CuO_4 and therefore holes are accepted into the CuO_2 plane. Thus the possibility of hole doping opposed to electron doping depends strongly on the existence of apical oxygen.

1.2.1 The CuO_6 octaheder

The cuprates belong to the transition metal oxides. As discussed above the hole doped cuprates have, because of their perovskite structure, an octahedral CuO_6 unit where six oxygen atoms surround one Cu atom forming an octaheder which is, however, elongated perpendicular to the CuO_2 plane. For deriving the physics of the CuO_2 plane a first look shall be given to the energy levels in this small unit of the cuprates. As a transition metal, Cu has its valence electrons in the 3d-shell where the energy levels are five-fold degenerate. This degeneracy is lifted by the ligand field of the surrounding oxygen atoms. First, six equidistant oxygen atoms forming an octaheder with cubic symmetry shall be considered. Looking at the region in space occupied by the radial functions of the d-orbitals, it is evident that the d_{z^2} and the $d_{x^2-y^2}$ point directly towards the oxygen atoms. Therefore, the electrons in those orbitals will spend more time close to
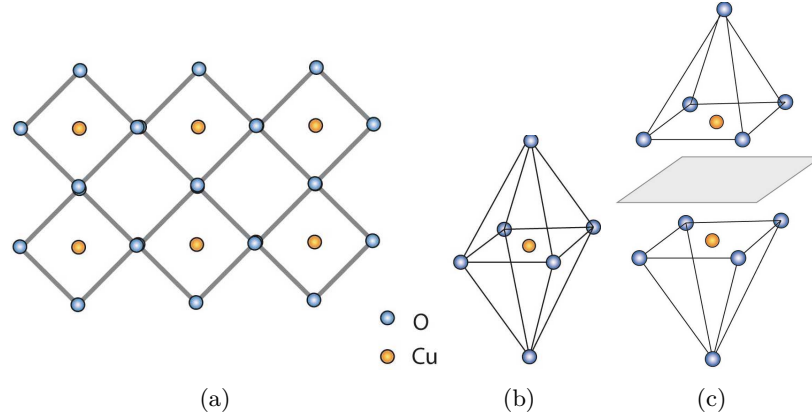
Figure 1.3: **(a)** *The CuO_2 plane in cuprates is formed by CuO_4 units which connect at the edges as indicated by the lines.* **(b)** *CuO_6 octaheder. Here already with Jahn-Teller distortion. The distance to the apical oxygenes is larger than that to the planar oxygen.* **(c)** *Cuprates with multiple CuO_2 planes per unit cell contain CuO_5 units instead of octaheders as in (b). The dividing plane between the two CuO_5 units is symbolized.*
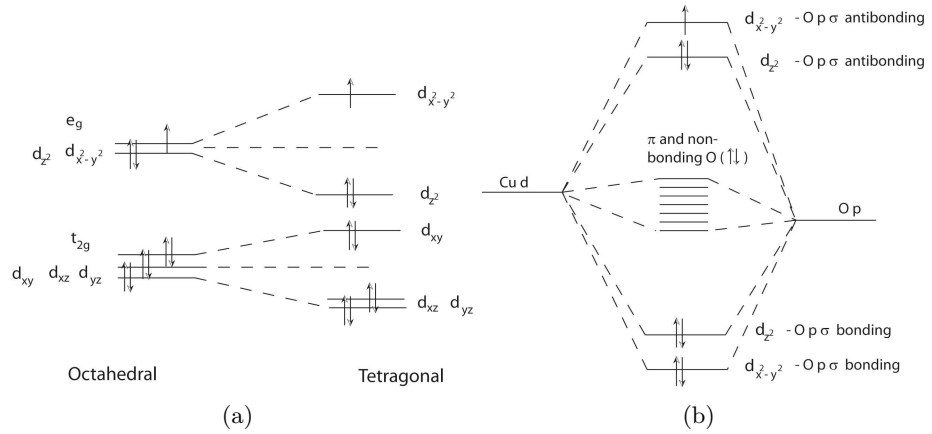
Figure 1.4: **(a)** *The degeneracy of the Cu3d orbitals is lifted by the crystal field of the 6 surrounding oxygen. The levels split into e_g and t_{2g}, which are additionally split by the Jahn-Teller distortion which leads to tetragonal symmetry.* **(b)** *Because of covalency between Cu3d and O2p, those orbitals hybridize. The antibonding $d_{x^2-y^2}$-Opσ becomes the upper half-filled level.*

the oxygen than the ones in the d_{xy}, d_{xz} or d_{yz} orbitals. The d_{z^2} and the $d_{x^2-y^2}$ will move up to higher energies resulting in a splitting into t_{2g} and e_g levels as shown in fig. 1.4(a) for the octahedral case. As mentioned, in the cuprates this octaheder is elongated in the z-direction. The apical oxygen are further away from the copper atom as the planar ones resulting in a Jahn-Teller distortion (see also fig. 1.3(b)). This lowers the symmetry to tetragonal and lifts the degeneracy even further as also shown in fig. 1.4(a). It is now evident that the valence electrons of the Cu3d^9 configuration leave one hole in the $d_{x^2-y^2}$ orbital. So far, a purely ionic model has been used to determine the electronic structure of the Cu ion in the crystal field. For deriving the same for the whole CuO$_6$ octahedral unit the covalency between oxygen and copper has to be taken into account. Looking at the orbitals with significant overlap - O2p and Cu3d - regarding their energy position and symmetry the resulting orbitals can be derived within molecular orbital theory. As illustrated in fig. 1.4(b) the highest orbitals are antibonding hybrids of O2pσ and e_g orbitals of the Cu3d shell.

Within the CuO$_2$ plane consisting of many CuO$_6$ units bands are formed. The electronic structure of the double layer Bi cuprate Bi2212 as derived by Pickett and Krakauer[35] using Local Densitiy Approximation (LDA) is given in fig. 1.5. Here, not only the CuO$_2$ plane, but also the charge reservoir planes are included into the calculation.
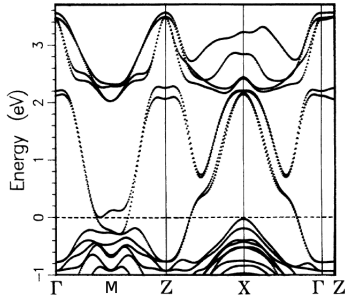

Figure 1.5: *LDA derived band structure of Bi2212 by Pickett and Krakauer[35]. The broken line refers to the Fermi level. Notation of high symmetry as defined in fig. 2.3(a) of chapter 2.2. The LDA calculated bands crossing the Fermi surface predict a metal.*

The two-dimensionality of the cuprates can be seen already in the LDA calculated bands. Dispersion exists only within the plane (Γ-M-Z-X-Γ), but perpendicular to it (Γ-Z) there is only small dispersion. Furthermore, all bands around the Fermi energy result mostly from Cu3d and O2p. The CuO$_2$ plane governs the electronic structure. However at this point special interest shall be given to the fact that the LDA derived bands predict metallic behavior. There are bands crossing the Fermi energy, and already from the ionic model in fig. 1.4(b) a half filled band at the Fermi energy can be deduced. This theoretical prediction is in strong contrast to the experimentally determined insulating behavior of the undoped cuprate parent compounds which represent the here considered half filled CuO$_2$ plane.

1.2.2 Strong correlations in the CuO$_2$ plane

The key to the physics in the cuprates are the strong correlations between the electrons. The Coulomb repulsion behaving as $\sim \frac{1}{r}$ is usually screened by the electrons of the system and becomes significant only at small distances. Therefore, by trying to put two electrons into the same orbital an energy penalty U for double occupancy has to
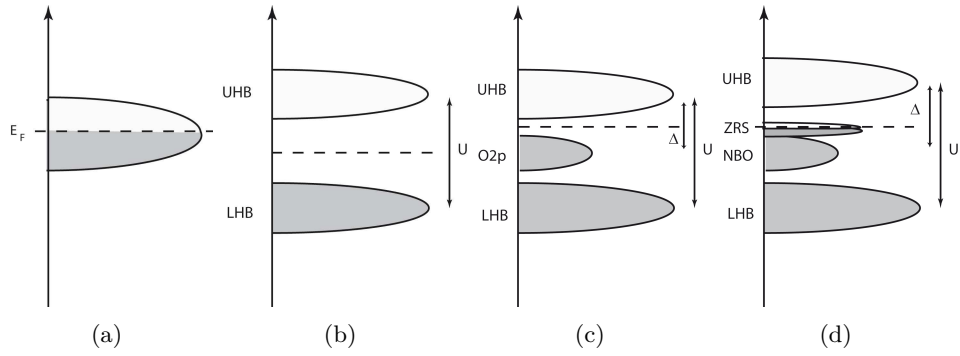
Figure 1.6: **(a)** *A half-filled band yields a metal from standard band theory. The Fermi level is indicated by the broken line in all sketches but only here denoted by E_F.* **(b)** *Strong correlations between electrons leads to a large U and thus to a gapped system. The Mott insulator with the upper (UHB) and lower (LHB) Hubbard band develops.* **(c)** *Since the non-bonding oxygen (NBO) lie between the two Hubbard bands, the gap Δ between oxygen and upper Hubbard band is smaller than U. The system becomes a charge-transfer insulator.* **(d)** *The doped hole at the oxygen will hybridize with a hole on a neighboring Cu forming a Zhang Rice Singlet (ZRS).*

be given. In the d-electron metal copper the orbitals are spatially small and U becomes so large that double occupancy is forbidden. The system develops a gap and changes from a metal (fig. 1.6(a)) to a so-called Mott insulator[36] (fig. 1.6(b)). Such systems exhibiting strong correlations, i.e. Mott insulators, can be described within the Hubbard model[37]. Therefore, the two developing bands are named the upper and lower Hubbard band.

This concept applies to the CuO_2 plane of the cuprates. However, here the physics is more complicated because of the oxygen ions. As illustrated in fig. 1.6(c) the O2p band lies energetically between the upper and lower Hubbard band. The energy Δ required for the transfer of an electron from an oxygen ion to a copper ion is 2-3 eV in the cuprates, and therefore much smaller than U which is 6-8 eV. The case $\Delta < U$ describes the so-called charge-transfer insulator as opposed to the Mott insulator with $\Delta > U$ as classified in the Zaanen-Sawatzky-Allen scheme by Zaanen et al.[38]. The topic of metal-insulator transitions is reviewed in great detail in Imada et al.[39].

Now, the Hubbard-Hamiltonian for the cuprates shall be derived. In the discussion above the important orbitals were identified as the hybridizing Cu $3d_{x^2-y^2}$ and O2p$_{x,y}$. The three-band model as derived Emery[40–42] captures most of the physics of the CuO_2

plane by incorporating only these orbitals:

$$
\begin{aligned}
H = &-t_{pd} \sum_{<ij>\sigma} \alpha_{i,j,\sigma}(p^+_{j\sigma}d_{i\sigma} + d^+_{i\sigma}p_{j\sigma}) - t_{pp} \sum_{<ij>\sigma} \alpha_{i,j,\sigma}(p^+_{i\sigma}p_{j\sigma} + p^+_{j\sigma}p_{i\sigma}) \\
&+ \epsilon_d \sum_{i,\sigma} d^+_{i\sigma}d_{i\sigma} + (\epsilon_d + \Delta)\sum_{i,\sigma} p^+_{i\sigma}p_{i\sigma} \\
&+ \frac{U_d}{2} \sum_{i,\sigma} n^d_{i,\sigma}n^d_{i,-\sigma} + \frac{U_p}{2} \sum_{\delta=x,y}\sum_{i,\sigma} n^{p_\delta}_{i,\sigma}n^{p_\delta}_{i,-\sigma} \\
&+ \frac{U_{pd}}{2} \sum_{\delta=x,y}\sum_{i,\sigma} n^{p_\delta}_{<ij>\sigma\sigma'}\cdot n^{p_\delta}_{j,\sigma'}
\end{aligned}
\tag{1.1}
$$

- $d^+_{i\sigma}$ creates a hole on the $d_{x^2-y^2}$ orbital

- $p^+_{j\sigma}$ creates a hole in the p_x or p_y orbital

- t_{pd} represents hopping between $d_{x^2-y^2}$ and p_σ orbitals

- t_{pp} hopping between p orbitals

- ϵ_d and $\epsilon_d + \Delta$ are the on-site energies of copper and oxygen respectively, with the charge-transfer gap Δ

- U_d, U_p, U_{dp} give the Coulomb repulsion in the d-, p-, and dp-orbitals respectively

In the limit of half-filling and $\Delta > U_d$ holes reside only on copper and the O2p bands can be neglected. Thus one arrives at the one-band Hubbard model which was first discussed by Anderson[43] as capturing the essential physics of the CuO$_2$ plane.

$$
H = -t \sum_\sigma \sum_{<ij>} (c^+_{i,\sigma}c_{j,\sigma} + c^+_{j,\sigma}c_{i,\sigma}) + U \sum_i n_{i\uparrow}n_{i\downarrow}
\tag{1.2}
$$

Note that at half-filling and for $U = 0$ eq. (1.2) reduces to the metallic tight-binding result.
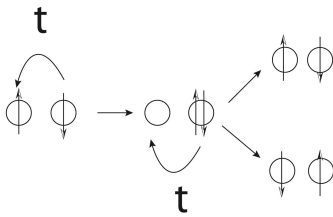
Figure 1.7: *Process of superexchange interaction.*

In the half-filled case each copper ion is occupied by one electron. Thus each ion can be simplified to one orbital. Looking at the hopping mechanism within the plane illustrated in fig. 1.7 it becomes evident that only electrons with antiparallel spin can hop because of the Pauli principle. This antiferromagnetic insulating state is characteristic for the Mott insulator. As discussed previously, ionic bonds between Cu and oxygen exhibit a significant amount of covalency. This is displayed not only in the electronic structure of the CuO$_2$ planes, also

the interaction of spins is mediated by oxygen via the superexchange interaction J as discussed by Anderson[44]. This process of hopping can be written in terms of spin operators. If additionally projecting out double occupancy, one arrives at the famous t-J-model[45]:

$$H = -t \sum_{<ij>} \sum_{\sigma} (1 - c_{i,\sigma'}^+ c_{i,\sigma'}) c_{i,\sigma}^+ c_{j,\sigma} (1 - c_{j,\sigma'}^+ c_{j,\sigma'})$$
$$+ J \sum_{<ij>} (\mathbf{S}_i \mathbf{S}_j - \frac{1}{4} n_i n_j)$$

(1.3)

The projecting out of double occupancy leads for half-filling to an insulating state and eq. (1.3) reduces to the Heisenberg antiferromagnet. This resembles the antiferromagnetic insulating ground state of the cuprate parent compounds. The strong and two-dimensional antiferromagnetic correlations in the cuprates could be shown experimentally determining J = 130meV[46–52]. Furthermore, it can be shown that with $J = 4\frac{t^2}{U}$ the t-J-model is the effective one-band Hamiltonian of eq. (1.2) and thus basically a strong coupling version of the Hubbard model.

In the following the doped CuO_2 plane shall be discussed. Since $\Delta < U$ in the cuprates doped holes go preferably into the O2p band. In their pioneering work Zhang and Rice[53] found that within a CuO_4 plaquette a hole located on the Cu site will hybridize most strongly with a doped hole in the surrounding oxygen forming a singlet and a triplet state. Eskes and Sawatzky[54,55] calculated the large energy difference of 3.5 eV and thereby showed that the triplet state can be neglected. The low energy excitation of the CuO_2 plane, the "Zhang Rice singlet" (ZRS), has the ability to hop from one CuO_4 plaquette to the other. The effective one-band Hamiltonian results again to the t-J model of eq. (1.3). The band scheme of a charge-transfer insulator with a ZRS state is shown in fig. (1.6(d)).

The derived electronic structure of the CuO_2 plane is summarized in fig. 1.8(a) which shows again the two-dimensional CuO_2 plane made up of square unit cells of Cu and four surrounding oxygen. Included are also the Cu $3d_{x^2-y^2}$ and $O2p_{x,y}$ orbitals. Furthermore on each Cu ion the spin is depicted. The spins order antiferromagnetically. In the central unit cell the concept of the ZRS is illustrated. For a review of the electronic structure in the CuO_2 plane and experiments see for instance Orenstein and Millis[56], and Norman and Pepin[57].

As stated, the ZRS is represented by the Hamiltonian of eq. (1.3). By comparison with experiment it became clear that the t-J-model fails to predict the characteristic rounded squares of the Fermi surface of the CuO_2 plane. This could be resolved by including long-range hopping t′ and t″ which denote second and third nearest neighbor hopping respectively and are sketched in fig. 1.8(a). The conduction band can be expressed within a tight-binding model for one $Cud_{x^2-y^2}$ orbital per unit cell as:

$$\epsilon(\boldsymbol{k}) = -2t(cosk_x + cosk_y) + 4t'cosk_xcosk_y - 2t''(cos2k_x + cos2k_y) + ...$$

(1.4)

The resulting band that corresponds well with experiments is shown in fig. 1.8(b). The

(a)   (b)

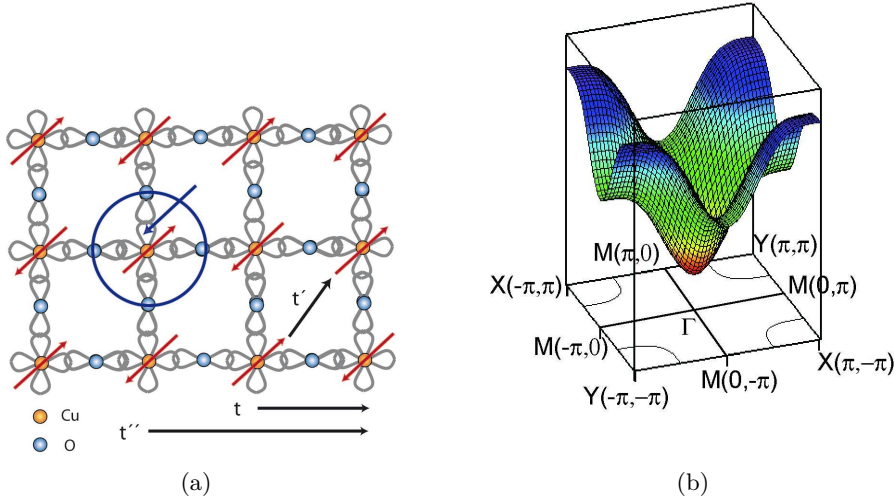Figure 1.8: *Summary of the CuO$_2$ plane:* **(a)** *CuO$_4$ units form the CuO$_2$ plane. The hybridizing orbitals are the Cu3d$_{x^2-y^2}$ and O2p$_{x,y}$. On each copper site sits a spin which points along the diagonal of the Brillouin zone. The spins align antiferromagnetically. An additional hole at an oxygen site gives another spin. The doped hole couples to the hole on the copper. The ZRS is formed. Furthermore included are the hoppping terms t, t' and t''.* **(b)** *The band derived from the hybridized Cu3d$_{x^2-y^2}$ and O2p$_{x,y}$. On the bottom the resulting hole-like Fermi surface is depicted within the Brillouin zone of the CuO$_2$ plane. Included are high symmertry points and their coordinates scaled to π. Note the flat band along ΓM and the Fermi surface barrels around the X/Y points.*

tight-binding derived band has a hole like Fermi surface (fig. 1.8(b)) with barrels around the X and Y points.

From the beginning of research on cuprates the modeling of the CuO$_2$ plane with only in-plane orbitals has been questioned. Lately the incorporation of out-of-plane orbitals has become more and more important. Andersen et al.[58] emphasized the importance of axial orbitals and included Cu$_{z^2}$, apical O2p$_z$, as well as Cu4s which acts as bridge for nearest neighbor and interplane hopping. Tanaka et al.[59] observed the impact on the Fermi surface of the changes in the second nearest neighbor hopping term t' among different cuprate families. A so-called range parameter r$\propto$t'/t can be connected to the material dependence in T$_c^{max}$ as Pavarini et al.[8] showed. As is illustrated in fig. 1.9(a) within this model the difference in T$_c^{max}$ for cuprates from different cuprate families, but with the same number of CuO$_2$ planes (fig. 1.2) per unit cell is derived from the surroundings of the CuO$_2$ plane. Another effect of the axial hybrid orbital is a k$_z$ dispersion of the conduction band[58] which results in extra nodes of the three-dimensional Fermi surface which were experimentally observed by Hussey et al.[60] using angle resolved magneto resistance (AMRO). The three-dimensional Fermi surface as deduced for the
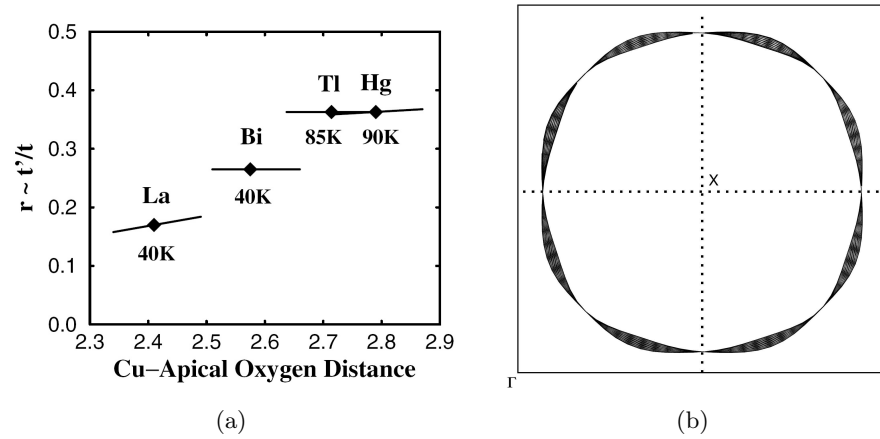
(a)   (b)

Figure 1.9: **(a)** *Pavarini et al.*[8] *calculated the range parameter r which is related to the nearest and second nearest neighbor hopping t and t′. Plotted over distance between Cu and apical oxygen in single layer cuprates it scales with $T_{c,max}$ in those materials. Both pictures are taken out of the respective cited work.* **(b)** *Projection of the three-dimensional Fermi surface of the one layer cuprate Tl2201 onto the **a,b**-plane. The shape of the Fermi surface was deduced by Hussey et al.*[60] *from AMRO measurements.*

single layer cuprate Tl2201 is shown for reference in fig. 1.9(b). Within these studies the three-dimensional Fermi surface was shown to be coherent, thus questioning theories for high-T_c superconductivity that rely on two-dimensional physics only. The existence of this axial hybrid orbital has also been indirectly observed by Xiang and Wheatley[61].

1.2.3 Phase diagram of doped cuprates

Substitution of rare earth elements as well as adding or removing non-stochiometric oxygen changes the hole content within the CuO_2 planes of cuprates. In most compounds a combination of both is used to reach the desired doping level. The substitution of cations takes place in layers adjacent to the CuO_2 plane, which are hence called charge reservoir layers.As mentioned earlier the undoped parent compounds are antiferromagnetic insulators. Additional, doped holes drive the cuprates through a phase diagram which seems to be universal in most regards for all cuprates. Therefore, it is widely viewed as the phase diagram of the CuO_2 plane. Fig. 1.10 gives a schematic illustration of this phase diagram. At low hole concentrations there is the antiferromagnetic insulator. It exists below the Néel temperature T_N. Towards higher hole concentrations the cuprates become more and more metallic in their normal state, i.e. at high temperatures. They evolve through a bad or "strange" metal state[62,63] to a Fermi liquid like behavior at very high hole concentrations. The most prominent characteristic of the strange metal state is the resistivity being linear in T in contrast to the T^2 dependence in Fermi liquid theory.[64]
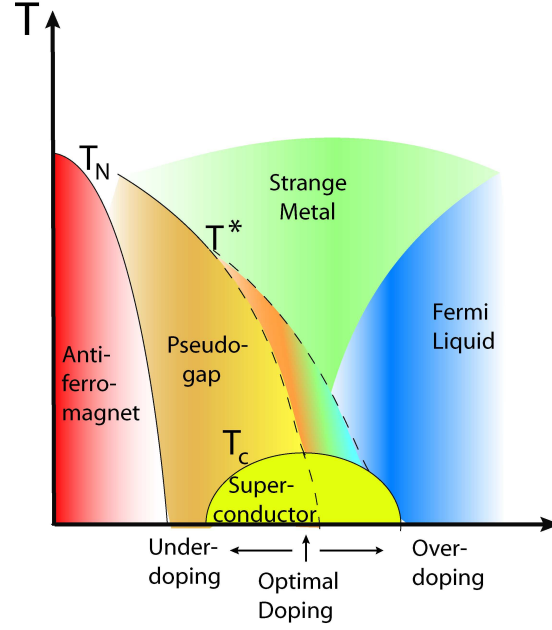
Figure 1.10: *Schematic phase diagram of the cuprates as described in the text. T_N gives the Néel temperature. T_c the superconducting transition temperature and T^* the temperature below which the pseudogap exists. The dashed lines of T^* show the three proposed possibilities of the evolution of T^* with hole concentration.*

At low temperatures the cuprates pass through a superconducting dome with growing hole concentration. Within this region they show d-wave superconductivity, where the superconducting gap changes sign upon a 90° rotation. This d-wave symmetry was deduced by theory[65] and later proven by experiments[66,67]. The superconducting transition temperature T_c becomes higher and higher with rising hole concentration until it reaches its maximum. This is called the optimal doping. Cuprates with a lower hole concentration are called underdoped. Upon further hole doping T_c falls again. The cuprates are then overdoped. Finally the superconducting phase ends and the cuprates become metallic also in this temperature region at very high doping levels. Presland et al.[68] established the concept of a 'universal' curve for the superconducting dome expressed by the relation:

$$\frac{T_c}{T_{c,max}} = 1 - 82.6 \cdot (n_h - 0.16)^2 \tag{1.5}$$

where $T_{c,max}$ gives the maximum T_c at optimal hole concentration n_h. The idea of this universal phase diagram is to describe the superconcucting characteristics upon hole doping of the CuO_2 plane itself. Thus, the superconducting dome as given from eq. (1.5) should apply to all cuprates, and at certain hole concentrations physical properties should change, as e.g. the setting in of high-T_c superconductivity at $n_h = 0.05$, the occurrence of maximum T_c at $n_h = 0.16$, and the total breakdown of superconductivity at around 0.27 holes per Cu. The only parameter changing between the compounds

should be $T_{c,max}$.

A phase of great interest but also a lot of controversy is the pseudogap phase in the underdoped region. The pseudogap, which is unprecedented before the cuprates, had been observed in angle resolved photoemission, tunneling, nuclear magnetoresistance, resistivity, specific heat, infrared conductivity and inelastic neutron scattering[69,70]. Below the pseudogap temperature T^* a gap opens in the single particle spectral weight, but the system is not yet superconducting. The pseudogap has been discussed to result from various fluctuation phenomena present in the cuprates, such as antiferromagnetic or superconducting fluctuations, as well as fluctuations in spin and charge density (stripe phenomena). Since the pseudogap resembles the superconducting gap in magnitude and phase it is often viewed as arising from effects related to superconductivity. But, the pseudogap is also seen as originating from states competing with superconductivity. Thus, the line of T^* is drawn differently in the phase diagram. It either envelops the superconducting dome, ends at the point of optimum hole doping, or cuts through the superconducting dome. These three variants are shown in fig. 1.10 by the dashed lines. They are extensively discussed in Hüfner et al.[71] and Norman et al.[72]. Here, it shall only be mentioned that a pseudogap region that is related to superconductivity, i.e. marks the onset of pairing without phase coherence, has to cover the whole superconducting dome which is according to Carlson et al.[73] and Hüfner et al.[71] the case when looking at the experimental data.

1.3 Proposed mechanisms of superconductivity in cuprates

It was already stated that cuprates are unconventional superconductors. They cannot be explained within the BCS derived phononic mechanism. BCS theory is based on a Fermi liquid normal state which is not present at least in the underdoped cuprates. Furthermore, the phononic BCS mechanism cannot account for such high transition temperatures T_c as found in the cuprates. In fact it was theoretically deduced that transition temperatures higher than 30 K will not be possible, since strong coupling leads to renormalization effects which let T_c saturate. Additionally, Migdal[74] showed that strong electron-phonon interaction leads to a lattice instability. More evidence of the failure of BCS theory in cuprates in a theoretically detailed manner can be found in Carlson et al.[73] and in most text books discussing high-T_c superconductivity and superconductivity in general, as e.g.[75].

Over time, a variety of models has been proposed of which only a selected few shall be mentioned in the following. Some start from the overdoped side imposing a Fermi liquid like normal state. They consider a BCS type model of superconductivity looking for a bosonic pairing mode, the "glue" of the Cooper pairs. Others start from the underdoped side emphasizing the strong correlations and the strange metal phase. The pairing occurs here as a characteristic of the correlated electron system itself.

1.3.1 Polarons and Bipolarons

Although cuprates cannot be explained within the BCS phonon mechanism, it could be shown that increasing the electron phonon interaction a small, heavy quasiparticle, the small polaron, can be formed. Further studies revealed that two electrons on opposite sides of a lattice distortion can form small bipolarons reminiscent of a collapsed Cooper pair. Bose condensation of the bipolaron gas leads to superconductivity. Within this theory critical temperatures around 100 K are possible. A review of polaronic behavior and phonons in cuprates can be found in Shen and Shen[76] and Zhou et al.[10]. Furthermore, Müller[77] discusses high-T_c superconductivity within a bipolaronic picture.

1.3.2 Spin waves and spin fluctuations

The spectrum of magnetic excitations has been widely studied in cuprates via Magnetic Resonance[78] and Neutron Scattering[79]. Some theories try to microscopically explain superconductivity in a strong-coupling version of BCS theory by using an Eliashberg or Eliashberg-type theoretical framework. The bosonic excitation responsible for pairing is, however, not a phonon, but has magnetic origin. Chubukov et al.[80] for instance tried to explain high-T_c superconductivity with spin fluctuations. Manske et al.[81] uses an Eliashberg type model incorporating the magnetic spectrum to give a microscopic account of superconductivity in cuprates.

1.3.3 Theory of high temperature superconductivity based on SO(5) symmetry

Zhang[82] proposed a unified theory of antiferromagnetism and superconductivity by introducing the superspin, a five component vector. The real and imaginery d-wave superconducting order parameters compose the two superconducting components. Furthermore, there are three spin components describing the antiferromagnetic order. This leads to an SO(5) symmetry group within which the phase diagram of the cuprates and especially the magnetic experiments can be explained. The phase transition from antiferromagnet to superconductor takes place by a superspin flop.

1.3.4 Hubbard Model in 2D

The two-dimensional Hubbard model not only describes the strong correlations present in the CuO_2 plane, it also captures the basic phenomena of the cuprate's phase diagram. At half filling which represents the undoped cuprate the two-dimensional Hubbard model shows an antiferromagnetic ground state and upon doping it develops a pseudogap phase. For the doped case d-wave pairing as well as striped states have been found at low temperatures. The problem of studying the doped cuprate within this model lies in the fact that only the half-filled case can be computed straightforwardly[83]. For numerically studying the doped Mott insulator variational methods have been developed. They, however, require different boundary conditions and assumptions which lead to a variety of results. Thus, the lightly doped case can exhibit stripes but changing the second
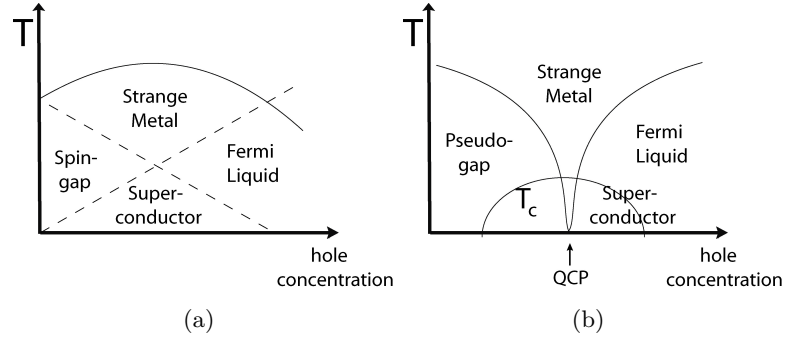
Figure 1.11: *Schematic phase diagramm of the Resonating Valence Bond model **(a)** and Quantum Critical Point scenario **(b)**. For details see text.*

nearest neighbor hopping t' or the strength of U favors $d_{x^2-y^2}$ pairing over stripes. A detailed review hereof is given by Scalapino[84].

1.3.5 Resonating Valence Bonds

The Resonting Valence Bond (RVB) model approaches the cuprates from the viewpoint of doping a Mott insulator and uses the t-J-Hamiltonian. The essential problem of treating a hole in an antiferromagnetic background is the competition between lowering the kinetic energy on the scale of t and maintaining the antiferromagnetic order governed by the size of J. For reducing its kinetic energy the hole wants to hop on a neighboring site. Then, however, the neighboring spin is in an ferromagnetic environment. The question is now, how the superconducting state emerges as the best compromise. Anderson[43] proposed a spin liquid as ground state. Here, in a simple picture, electrons are bound together in pairs at neighboring sites in singlet states comparable to the Heitler-London-covalent bond. They lower their energy when allowed to resonate, which gives a linear combination of all such configurations. Thus, one has the resonating valence bond. A very important aspect of the RVB model is the existence of spin-charge separation. This phenomenon was not known before to occur in a two-dimensional system. The phase diagram of the cuprates can be captured within a mean-field approach where the d-wave state has the lowest energy. The gap of this state applies to the spins and decreases with increasing doping. Thus, it can be associated with the pseudogap. The phase coherence of the holons, however, grows with rising doping. Bose condensation of holons leads to superconductivity. As shown in fig. 1.11(a), this gives two crossover lines with doping, where there is the spin gap phase on the left, the Fermi liquid on the right, the super-conducting phase on the bottom and the strange metal phase on the top. A review of current developments regarding the RVB theory is given by Lee[85].
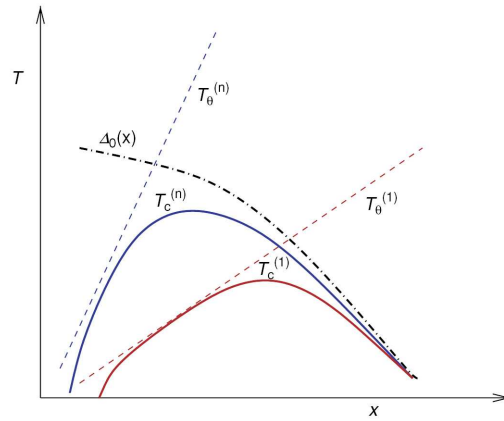
Figure 1.12: *Schematic phase diagram of "dynamic inhomogeneity-induced pairing" taken from Kivelson and Fradkin [87]. The dashed-dotted line gives the superconducting gap magnitude $\Delta_0(x)$, while dashed line shows the phase ordering temperature T_θ for the case of a single layer, $T_\theta^{(1)}$, and a multi-layer, $T_\theta^{(n)}$, cuprate. The onset of superconductivity, $T_c^{(1,n)}$, is represented by the colored lines.*

1.3.6 Marginal Fermi liquid and Quantum criticality

The strange metal phase led to the proposition of the Marginal Fermi liquid [86]. The Marginal Fermi liquid describes a system with correlations strong enough to let Fermi liquid theory break down, but just barely. Thus, some properties of the Fermi liquid still apply. The phenomenological model lets electrons scatter off a bosonic spectrum which has no other energy scale than temperature and hence exhibits quantum critical scaling. The Marginal Fermi liquid accounts for many properties of the strange metal phase as for instance the linear temperature dependence of in-plane resistivity. But, there is no explanation from where d-wave superconductivity should occur. The quantum critical scaling has led to the proposition of explaining the phase diagram based on a quantum critical point occuring at optimal doping at T=0K as illustrated in fig. 1.11(b). Above it lies the quantum critical regime associated with the strange metal. This separates two phases, the pseudogap to its left from the Fermi liquid to its right. The superconducting dome covers this quantum critical point.

1.3.7 Electronic inhomogeneity and stripes

Within the model of "dynamic inhomogeneity-inced pairing" [73,87] pairing results from the strong repulsive interactions. The main idea is that cuprates have an intrinsic electronic inhomogeneity which is strong enough for pairing, but too weak to totally destroy phase coherence. Superconductivity is then a crossover of the homogenous regime where pairing occurs and a granular regime with phase coherence exhibiting a pseudogap (see also fig. 1.12). The superconducting gap magnitude $\Delta_0(x)$ is a falling function of the hole concentration x. Since it resembles the scale of pairing, which in turn happens

on short distances in cuprates, $\Delta_0(x)$ is assumed to be a property of the CuO_2 plane only. The phase ordering temperature T_θ, however, is governed by long-wave-length-fluctuations. Hence, it is dependent on the number of CuO_2 layers per unit cell n, and on the charge-reservoir layers, and thus on the cuprate family. Therefore, in fig. 1.12 the two curves for single and multi-layers behave differently over hole concentration. T_c is limited by the pairing scale and the phase coherence temperature.

This model could be realized by stripes, the unidirectional ordering of charge and spin, which have been observed in cuprates[88]. Then the cuprates could be seen as quasi-one-dimensional systems where there is naturally non-Fermi liquid behavior and spin-charge separation. The pseudogap is identified with a spin-gap and holes can pair by virtual hopping through the antiferromagnetic domains. Below a critical temperature superconductivity emerges because of coherence between the stripes realized by Josephson coupling.

1.4 Scope of thesis

From the models and experimental evidence presented in the introduction it can be deduced that while the CuO_2 plane common to all cuprates is the origin of high temperature superconductivity, the differences in superconducting characteristics, i.e. maximum T_c, among the families can only be accounted for when looking at the surrounding of the CuO_2 plane. Here, among others, especially the incorporation of axial orbitals has led to a theoretical argumentation for the differences in maximum T_c[8]. Within the model of charge inhomogeneity (sec. 1.3.7) the idea was briefly discussed that pairing may be confined to the CuO_2 plane, and thus, is independent of the spacer layers, while phase coherence is a more long-range quality, and may also depend on the structure outside the CuO_2 plane. Hence, although three-dimensionality is most likely not the key point for pairing, it probably is critical for maximizing T_c. The question remains whether there is any influence of the axial orbitals on the orbitals within the CuO_2 plane, and how this in turn impacts the description of electronic structure, that, as has been seen in the previous section, mostly relies on the two-dimensional electronic structure of the CuO_2 plane. This issue will be approached within this work by polarization dependent x-ray absorption measurements. Contrary, to past x-ray absorption research done on cuprates, the polarization has been varied within the plane and an unexpected polarization dependence has been revealed that indeed shows signatures of the in-plane part of the axial hybrid orbital.

The basic question of high temperature superconductivity surely is the one regarding the pairing mechanism. To solve this problem predictions of proposed models have to be checked by experiments. Within this thesis the excitations close to the Fermi surface in the antinodal region are probed by angle resolved photoemission. In the past, contradicting observations have been made on the commonly investigated double layer Bi cuprate and the less often experimentally probed single layer Bi cuprate: While in the double layer Bi cuprate the spectral weight close to the Fermi surface has been reported to develop the so called sharp peak at low temperatures that vanishes above T_c[89], a

similar sharp emission has been reported in the single layer Bi cuprate to persist up to higher temperatures than T_c[11]. Furthermore, in the antinodal region of the double layer Bi cuprate a so-called kink, a renormalization of the dispersion, has been observed[10,90], while in the single layer Bi cuprate such a renormalization has not been unequivocally reported yet. These observations seemingly point towards different models. Although, the double layer Bi cuprate is the most investigated cuprate by photoemission, its lineshape is complex due to interlayer effects. The measurements conducted within this thesis exploit differing matrix element dependencies on photon energy of bonding and antibonding band combined with defined polarization settings to distinguish between both bands, and unify the experimental observation on the single and double layer Bi cuprate. These experiments show that additional excitations exist. If these are taken into account the seeming contradictions can be resolved.

Before exploring the issues laid out above, the investigated samples will be discussed in chapter 2, and then the experimental techniques of angle resolved photoemission and x-ray absorption will be introduced in chapter 3 and chapter 4, respectively. In chapter 5 the XAS measurements will be presented and the in-plane polarization dependence analyzed in detail. Then, implications of the XAS results for the electronic structure will be discussed. Furthermore, the determination of hole content by XAS in single- and polycrystalline single layer Bi cuprates is explained. This will enable to lay out a specific phase diagram for the single and double layer Bi cuprates. Finally, the angle resolved photoemission experiments are described, analyzed and discussed within the proposed models for high temperature superconductivity in chapter 6. And in chapter 7 the results obtained within this thesis will be summarized.

2

Details on the Bi cuprates

In this chapter the samples investigated within this thesis, the single and double layer Bi cuprates, will be introduced. The crystal structure in real and reciprocal space, the specific doping mechanism in Bi cuprats, crystal growth and sample characterization will be explained. The section on crystal structure in real space will also treat known superstructures of the Bi cuprates which will be become important to consider when interpreting experiments. It will be seen that the adding of dopants causes inhomogeneity on the nanoscale. Hence, also the section on doping will extend the discussion of the real crystal structure. Since great long-term experience of Bi cuprates synthesis exists in our group, the details of crystal growth have been described several times previously, and will here only be briefly described. Finally, details of sample characterization as done after growth will be given. Thus, sample quality regarding compositional, structural, and superconducting properties is secured.

2.1 The ideal crystal and reality

The ideal structure of the single and double layer Bi cuprates is shown in fig. 2.1. The layered structure is the same in both materials except for the number of CuO_2 planes of which the one layer material possesses one, and the double layer two. The adjacent CuO_2 planes in the double layer material are separated by a Ca layer. Otherwise the unit cell consists of two BiO planes and a perovskite block containing the CuO_2 layer(s) enveloped by SrO planes. Within this perovskite block the CuO_6 octaheder is composed out of a CuO_4 unit and an apical oxygen from the SrO layer. The BiO planes are only weakly van der Waals bonded. Therefore the crystal cleaves between those two layers giving a well defined and inactive surface.

The adjacent BiO planes exhibit a rocksalt structure and are thus shifted against each other by half a diagonal of a BiO plaquette (see fig. 2.1(a)). This leads to the true unit cell being face centered orthorombic which is shown in fig. 2.1(b) and fig. 2.1(c) for the single and double layer Bi cuprate respectively. But, the unit cell can be
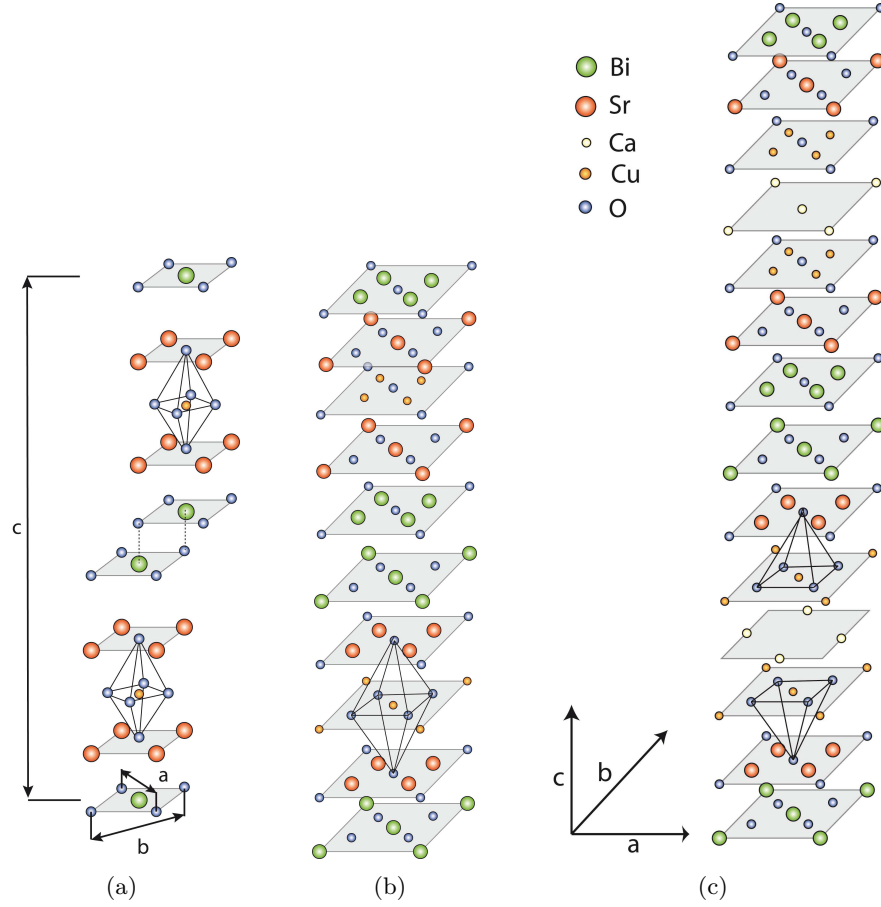
Figure 2.1: **(a)** *Tetragonal unit cell of Bi2201. For better visibility the second half of the cell is shown shifted as explained in the text. Therefore, the illustration does not show the true unit cell.* **(b)** *Orthorombic unit cell of the single layer Bi-cuprate Bi2201.* **(c)** *Orthorombic unit cell of the double layer Bi cuprate Bi2212.*

simplified as illustrated in fig. 2.1(a) to body centered tetragonal which is then often called pseudo-tetragonal.

From the considerations above and fig. 2.1 the chemical formula of the Bi-cuprates can be deduced which is generally $Bi_2Sr_2Ca_{n-1}Cu_nO_{4+2n+\delta}$ where n denotes the number of CuO_2 planes. Hence, it becomes $Bi_2Sr_2CuO_{6+\delta}$ for the single layer and $Bi_2Sr_2CaCu_2O_{8+\delta}$ for the double layer compound. Mostly the short notation Bi2201 and Bi2212, giving the combination of Bi-Sr-Ca-Cu in the chemical formula, is used which will be adopted within this thesis.

However, the real crystal structure of the Bi cuprates deviates from this ideal situation. In single and double layer Bi curpates an $\approx$ 5x1 superstructure exists along the crystallographic **b** direction. This superstructure modulation has orthorombic symmetry in the double layer Bi cuprate Bi2212 and monoclinic symmetry in the single layer
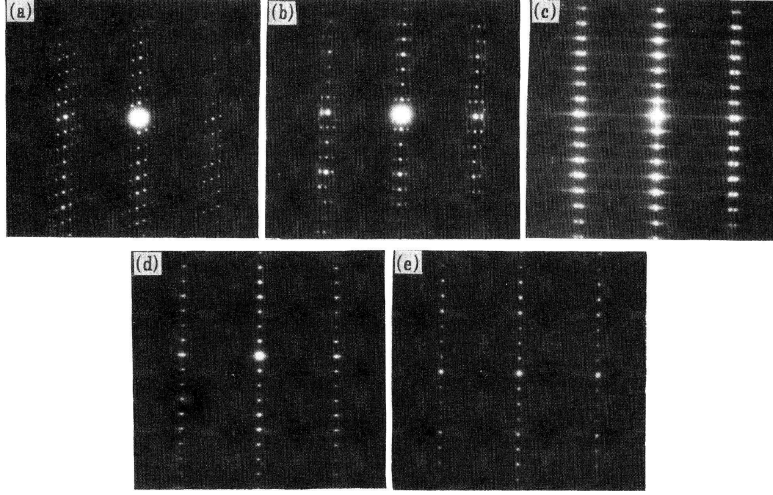
Figure 2.2: *Electron diffraction pattern of $Bi_{2-y}Pb_ySr_2CuO_{6+\delta}$ along the [100]-zone axis which is the direction of the orthorombic superstrucure. The orthorombic and monoclinic superstructure change with varying Pb content. (a) y=0: Monoclinic and orthorombic superstructures are present. (b) y=0.05. (c) y=0.2: The monoclinic superstructure has disappeared. Only the orthorombic superstructure remains. (d) y=0.3. (e) y=0.6: Also the orthorombic superstructure has vanished.*

Bi cuprate Bi2201. For the latter it has been shown that the substitution of Sr by La in the SrO layer leads to monoclinic and orthorombic fractions in the crystal[91]. The origin of this $\approx$ 5x1 superstructure has been, and still is, a source of debate. Two models are considered here: the misfit between the BiO-rocksalt-structure and the perovskite structure of the CuO-SrO block[92,93], and the incorporation of non-stochiometric oxygen[94]. The rocksalt structure of the BiO planes and the perovskite block containing the CuO_2 and SrO layer do not fit onto each other[95]. The crystal has to adapt to this misfit which has been argued to lead to the observed buckling of the CuO_2 plane[95,96] which can be conceived as a tilting of the CuO_6 octaheder. Another possiblility to account for the rocksalt-perovskite misfit is the periodic intercalation of non-stochiometric oxygen into the BiO plane which has been suggested to cause the superstructure. It could be shown that the substitution of Pb for Bi increases the periodicity for the discussed superstructure[97]. This is illustrated in fig. 2.2 where electron diffraction patterns of single layer Bi cuprate Bi2201 samples with different Pb substitution levels are shown. For Pb=0 the orthorhombic and monoclinic superstructure is present. The latter has vanished at a substitution level of Pb=0.2, where only the orthorombic superstructure exists. When further increasing the Pb content, the superstructure totally vanishes. This is shown in the figure for the case of Pb=0.6. In recent scanning tunneling microscopy studies[13,98,99], it has been shown that in single layer Bi cuprates Bi2201 with La and Pb substitution the $\approx$ 5x1 superstructure is suppressed at a Pb substitution of 0.3. However, with increasing Pb content a phase mixture of so-called α- and β-phases develops. From a detailed analysis it resulted that in the single layer Bi cuprate Bi2201 a Pb content

of 0.4 is the most favorable regarding the structural cleanness [13]. Furthermore, the α- and β-phases have also been found in the double layer Bi cuprate Bi2212 where the $\approx$ 5x1 superstructure was also suppressed around a Pb substitution of 0.3 [13]. For brevity, in the following the substitution of Pb will be indicated by writing (Pb,Bi)2201 and (Pb,Bi)2212 respectively for single and double layer Bi cuprates containing Pb, while for samples without Pb substitution the notation of Bi2201 and Bi2212 will be kept.

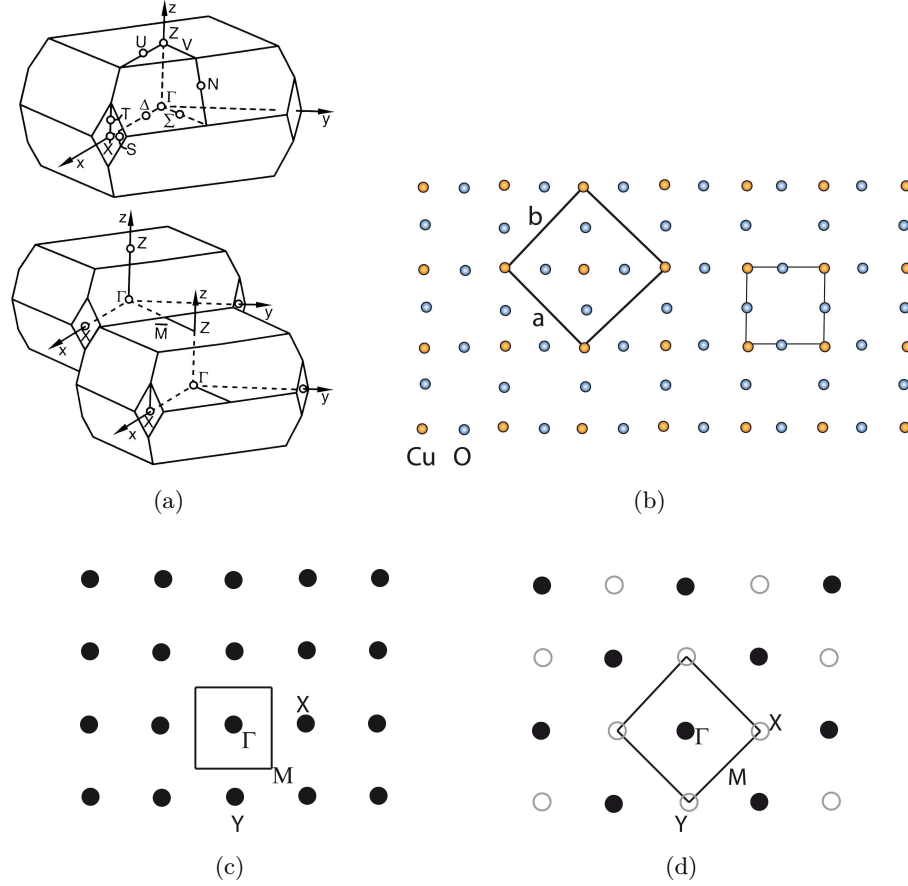## 2.2 Reciprocal space - highly symmetric directions

Figure 2.3: **(a)** *Adjacent Brillouin zone of a body-centered tetragonal lattice including symmetry points and high symmetry directions.* **(b)** *Orthorombic and pseudotetragonal Wigner-Seitz cell of the CuO$_2$ plane.* **(c)** *Respective Brillouin zones for (b).*

To derive the reciprocal unit cell of the Bi cuprates, the body-centered tetragonal cell as discussed in the section above is used. Fig. 2.3(a) shows two adjacent three-dimensional Brillouin zones. Included in the figure are the respective symmetry points and the high symmetry directions. The change from orthorombic to tetragonal description of the unit cell is also reflected in the Brillouin zone of the two-dimensional CuO$_2$

plane. This is illustrated in fig. 2.3(b) to 2.3(d) where the centered orthorombic and the simple square lattice is shown in real and reciprocal space. Thus, the Brillouin zone of the CuO$_2$ plane in the Bi cuprates reduces to the simple square lattice as discussed in section 1.2. Hereby, the notation is Γ=(0,0), M=(π,0), Y=(π, π), X=(-π, π), and the ΓM direction again points along the CuO bonds.

2.3 Doping in the Bi cuprates

As mentioned in the introduction doping can be achieved by substitution of rare earth atoms or by the variation of non-stochiometric oxygen which introduces additional holes into the CuO$_2$ plane. This is also the case in Bi-cuprates. The as-grown double layer compound is optimally doped, and the hole concentration can be changed by varying the content of non-stochiometric oxygen by annealing. This is the technique used in the present thesis. It is, however, possible to bring dopant atoms into the Ca layer between the adjacent CuO$_2$ planes. Here, it is common to replace Ca by Y atoms. Another possiblility is the substitution of Sr by La within the SrO layer, which is, however, less common.

Also, the hole concentration in single layer Bi cuprates has to be varied by annealing or cation substitution. The latter is achieved for the crystals measured within this work substituting La into the SrO layer. This introduces electrons into the CuO$_2$ plane by replacing Sr^{2+} with La^{2+}, and hence, lower hole concentrations can be reached.

The dopants not only change the hole concentration, but also induce inhomogeneities into the cuprates. This was observed and investigated by various groups using different technical methods. In Bi2212 especially interstitial (non-stochiometric) oxygen and its impact on the magnitude of the superconducting gap has been studied by scanning tunneling microscopy[2,100]. The same effect has been seen in Bi2201[101]. Effects of out of plane disorder have further been investigated by resistivity measurements[102] and angle resolved photoemission[103] to only name a few.

Eisaki et al.[104] systematized the various dopants according to their placement within the unit cell. They proposed that the nearer dopants are situated to the CuO$_2$ plane, the greater will be the impact on the superconducting properties. The scheme given by Eisaki et al.[104], and shown in fig. 2.4, makes this more plausible. In the first row of fig. 2.4, the sites that dopants can be places at are listed. Column (a) denotes dopants at the so-called A site, namely ones that are close to the apical oxygen. In the case of single layer Bi-cuprates this corresponds to the La substitution into the SrO layer. These dopants have the greatest impact on the superconducting properties since they are closest to the CuO$_2$ plane and additionally in proximity to the apical oxygen. Thus, a resulting lattice distortion can lead to a tilt of the CuO$_6$ octaheder or CuO$_5$ pyramid. In addition, the Coulomb potential caused by the dopant can directly be transmitted to the CuO$_2$ plane through the apical oxygen which is bonded to the CuO$_2$ plane. In double layer compounds there is also the possibility to induce dopants into the plane between the adjacent CuO$_2$ layers as e.g. the replacement of Ca by Y in Bi2212. This replacement given in pattern (b) is also close to the CuO$_2$ plane, but in contrast to (a)

there is no apical oxygen present. Pattern (c) finally stands for dopants further away from the CuO$_2$ plane like e.g. non-stochiometric oxygen. In the next three rows single to triple layer materials are listed. It can be seen that T$_{c,max}$ not only rises with the number of CuO$_2$ planes which is expected, but also from column (a) to (c). Hence, compounds with dopants further away from the CuO$_2$ plane have a higher T$_{c,max}$.

Legend (families):

Halogen Family	Bi Family
Pb Family	1L Tl Family
La Family	2L Family
YBCO Family	Hg Family

(a)

(a-1)	T_c
Ca$_{2-x}$Na$_x$CuO$_2$Cl$_2$	26
Pb$_2$Sr$_{2-x}$La$_x$Cu$_2$O$_z$	33
La$_{2-x}$M$_x$CuO$_4$	39
Bi$_2$Sr$_{1-x}$Ln$_x$CuO$_{6+\delta}$	38
TlBa$_{1+x}$La$_{1-x}$CuO$_5$	45

(a-2)	T_c
La$_{2-x}$Sr$_x$CaCu$_2$O$_6$	60
(La$_{1-x}$Ca$_x$)(Ba$_{1.75-x}$La$_{0.25+x}$)Cu$_3$O$_y$	80
Bi$_{2+x}$Sr$_{2-x}$CaCu$_2$O$_{8+\delta}$	90

(a-3)	T_c
Bi$_{2+x}$Sr$_{2-x}$Ca$_2$Cu$_3$O$_{10+\delta}$	110
TlBa$_{2-\varepsilon}$Ca$_2$Cu$_3$O$_{9+\delta}$	123

(b)

(b-1): —

(b-2)	T_c
Pb$_2$Sr$_2$Y$_{1-x}$Ca$_x$Cu$_3$O$_{8+\delta}$	80
Y$_{1-x}$Ca$_x$Ba$_2$Cu$_3$O$_{7-\delta}$	90
Bi$_2$Sr$_2$Ca$_{1-x}$Y$_x$Cu$_3$O$_{8+\delta}$	96

(b-3)	T_c
TlBa$_2$Ca$_{2-\varepsilon}$Cu$_3$O$_{9+\delta}$	131

(c)

(c-1)	T_c
Sr$_2$CuO$_2$F$_{2+x}$	46
La$_2$CuO$_{4+\delta}$	45
Tl$_2$Ba$_2$CuO$_{6+\delta}$	93
HgBa$_2$CuO$_{4+\delta}$	98

(c-2)	T_c
YBa$_2$Cu$_3$O$_{7-\delta}$	93
TlBa$_2$CaCu$_2$O$_{7+\delta}$	110
Tl$_2$Ba$_2$CaCu$_2$O$_{8+\delta}$	110
HgBa$_2$CaCu$_2$O$_{6+\delta}$	120

(c-3)	T_c
TlBa$_2$Ca$_2$Cu$_3$O$_{9+\delta}$	133
Tl$_2$Ba$_2$Ca$_2$Cu$_3$O$_{10+\delta}$	125
HgBa$_2$Ca$_2$Cu$_3$O$_{10+\delta}$	135

Figure 2.4: *Systematics of cuprates according to the site of disorder and the number of CuO$_2$ planes as taken from Eisaki et al.[104] The color marks different families. Details to the sites denoted by (a) to (c) can be found in the text.*

Besides the disorder from La substitution (Pb,Bi)2201 also suffers from disturbances caused by Bi atoms sitting on Sr sites. According to Eisaki et al.[104], who studied the dependence of T$_{c,max}$ on the type of dopant around the apical oxygen (A-site), the induced disorder is severer when replacing Sr by Bi compared to the replacement by La.

Bi is smaller and has furthermore an asymmetrical shape originating from the lone pair in the Bi^{3+} ion. Thus the La atom is much more similiar in size as well as electronic configuration to the Sr atom than the Bi atom is.

2.4 Crystal growth

Figure 2.5: *Single crystals in the circonium oxide crucible after growth.*

The crystals investigated within this work were grown within our group thanks to the long-term experience in crystal growth of Dr. Alica Krapf. The crystal growth using the flux method was described elsewhere[13,99] in great detail, and shall, therefore, be only briefly laid out here. The basis components Bi_2O_3, $SrCO_3$, $CaCO_3$ and CuO are mixed according to the desired composition in the resulting crystal. The mixture is homogenized by solving in ethanol and grounding. Then the mixture is calcined to dissolve the carbonates. When growing crystals containing Pb or La, LaO and PbO are added after calcination. Then the composition is again solved in ethanol and grounded. Afterwards the mixture is heated beyond the liquidus temperature in a circonium crucible. This temperature is held for a few hours for homogenization. Then the mixture is cooled first to the cristallization temperature and then to the solidus temperature. After stabilization of the system it is rapidly cooled to room temperature. The respective cooling rates are essential for the growth process and depend on the desired result. This also applies to all other details of the growth procedure. E.g. for growth of double layer Bi2212 crystals with a high Pb-content additional air is supplied during the growth prcess, whereas for single layer Bi2201 additional oxygen is needed. After growth various patches of single crystals developed in the circonium pot (fig. 2.5). They can be cleaved off and characterized as described in the following.

2.5 Sample characterization

After growth the samples are investigated regarding their chemical composition by energy dispersive x-ray analysis (EDX). The superconducting properties are examined by ac susceptibility. Informations about structure and orientation are obtained by low energy electron diffraction (LEED) or Laue diffraction. In the following the employed methods of sample characterization shall be introduced shortly.

2.5.1 Chemical composition - energy dispersive x-ray analysis (EDX)

The crystal growth can be checked by determining the actual stochiometric composition of the sample. This can be achieved by placing the sample into an electron beam using a scanning-electron-microscope. The resulting lines of the characteristic x-ray spectrum

are measured energy dispersive with a semiconductor detector. Then the different atoms and their concentration within the crystal can be calculated using the PUzaf[105] correction by commercial software. Note that with this method oxygen content cannot be determined straightforwardly. The crystals used within this work were investigated with an electron beam of 20 keV and a resolution of $\approx$135 eV[106]. In fig. 2.6 a typical EDX spectrum of a double layer Bi cuprate Bi2212 is shown.
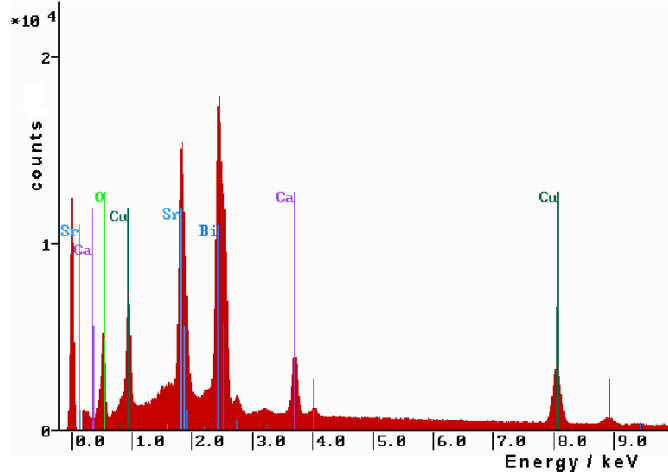
Figure 2.6: *The graph shows a spectrum of an EDX-analysis of a Bi 2212 single crystal. One can observe the spectrum of bremsstrahlung and the characteristic lines. The respective elements are indicated.*

2.5.2 Superconducting properties - ac-susceptibility

Cuprates are type II superconductors, meaning they exhibit two critical magnetic fields H_{c1} and H_{c2} as shown in fig. 2.7(a). Below H_{c1} the superconductor is in the Meissner phase, and hence, behaves like an ideal diamagnet. Between H_{c1} and H_{c2} the magnetic field penetrates the superconductor in form of flux vortices. This is called the Shubnikov phase. The phase diagram of magnetic induction versus temperature for the type II superconductor is given in fig. 2.7(b). Field and magnetization are related by M=χH, where χ is the susceptibility. The change from paramagnetic to diamagnetic characteristics when becoming superconducting can be deduced from the susceptibility, and thus T_c can be determined. The ac-susceptibility is measured in an alternating magnetic field with a PPMS 6000 (Quantum Design). At high frequencies the magnetization is lagging behind the magnetic field. A 'complex susceptibility' can be measured where the real part is the susceptibility χ and the imaginery part is a measure of the dissipative energy loss. The latter can be used to judge the quality of the sample. Inhomogenic samples have more than one maximum. Furthermore high quality samples can be distinguished by a sharp superconductig transition which is marked by a small ΔT in the χ(T) curve. ΔT is defined as the temperature difference between 10% and 90 % of χ(T=T_c). Fig.

2.7(c) and 2.7(d) shows typical ac-susceptibility measurements of a single and double layer Bi cuprate respectively. In each figure real and imaginary part of χ are included.
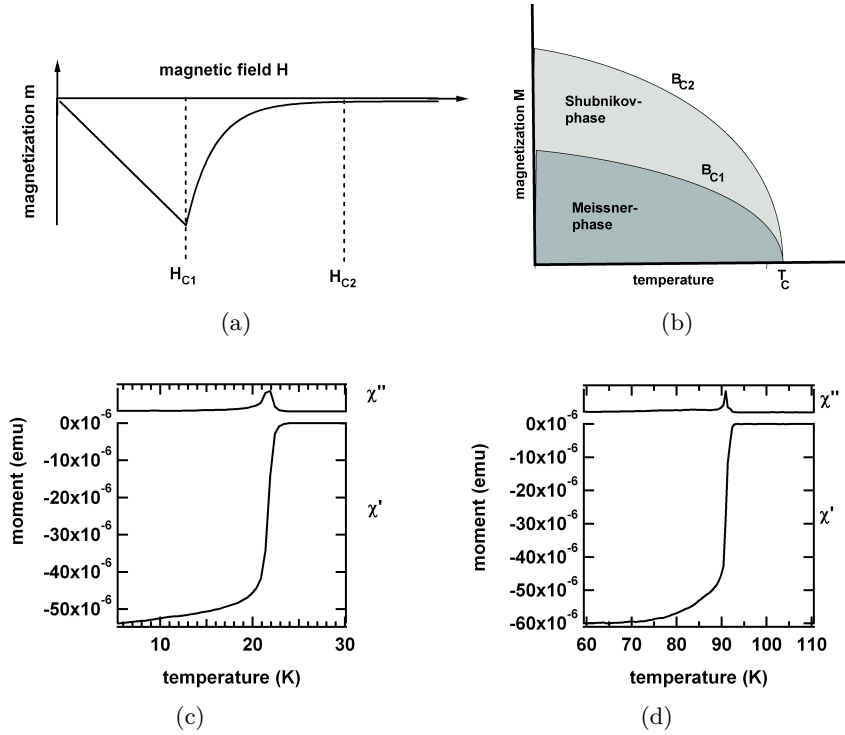
Figure 2.7: *(a) Magnetization M versus applied magnetic field. Upon the critical field H_{c1} the superconductor changes from the Meissner into the Shubnikov phase where the magnetic field penetrates the superconductor in form of flux vortices. Above H_{c2} is the normal conductor. (b) Phase diagram of magnetic induction versus temperature for the type II superconductor. (c) AC-susceptibility over temperature of a La doped (Pb,Bi)2201 single crystal with a Pb substitution of y=0.5 and a La content of x=0.35, T_c=22 K and ΔT=2.5 K. (d) The same as (c) for a double layer (Pb,Bi)2212 single crystal with a Pb substitution of y=0.23, T_c=92 K and ΔT=3 K.*

2.5.3 Structural properties - Laue diffraction and LEED

The structual quality of the sample can be verified by Laue diffraction and low energy electron diffraction (LEED). Only structurally clean samples will exhibit sharp, and for the crystal structure typical reflexes in a diffraction experiment. Additionally, the orientation of the sample is determined which is essential in angle resolved photoemission experiments which will be conducted within this work. For the Laue experiment the sample is exposed to a continually x-ray spectrum. This contains besides the continuous bremsstrahlung, the characteristic lines of the employed cathode material. In the case shown in fig. 2.8(a) this is a Cu cathode. The wave lengths that fulfill the Bragg relation will produce reflexes according to the three-dimensional Ewald sphere. The diffraction reflexes are detected using x-ray sensitive negativ or polaroid film. The continuous

radiation creates lines, while the characteristic radiation gives the distinct spots. The x-ray radiation penetrates into the sample and thus the diffraction comes from the bulk. Laue diffraction patterns can be highly complex, but, in the case of Bi cuprates the analysis is simplified since Bi cuprates cleave between the adjacent BiO planes. Hence, the **c**-axis is always normal to the sample surface. Placing the sample normal to the x-ray beam, thus, gives the typical pattern of the **ab** plane of the orthorombic unit cell shown in fig. 2.8(a).

In contrast, in the LEED experiment the sample is placed into a beam of low energy electrons. These have a small penetration depths and, thus, the LEED experiment is surface sensitive. The spots of the reciprocal lattice become bars in the third dimension, and hence, the Ewald construction is two-dimensional in the LEED experiment. Another consequence of the surface sensitivity is the need for clean surfaces and vacuum. Hence, the samples have to be cleaved to carry out LEED. From this point of view Laue diffraction may be advantagious. Of course, also the interpretation of LEED patterns is easy in Bi cuprates because of the predetermined cleaving plane. For illustration the LEED pattern of the same sample of which the Laue pattern in fig. 2.8(a) was taken is shown in fig. 2.8(b).

(a)   (b)
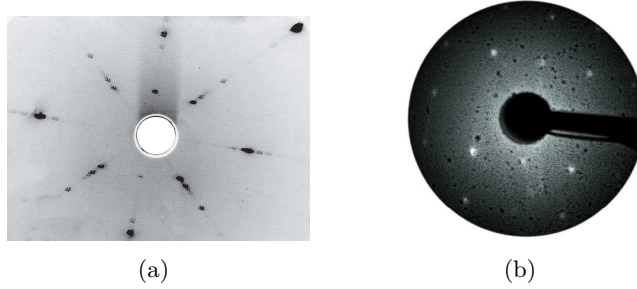
Figure 2.8: *(a) Laue and (b) LEED pattern of the same double layer cuprate (Pb,Bi)Bi2212. The sharp spots of the orthorombic unit cell can be seen in each case.*

3

Angle resolved photoemission (ARPES)-Principals and apparatus

In this chapter a short introduction into the technique of photoemission is given. First the photoemission process itself and the three-step-model are discussed in more detail. The latter is a generally used approximation for derivation of the photocurrent that breaks the photoemission process down into three steps. Besides allowing the possibility of calculable predictions, those three steps also give an intuitive understanding of photoemission. Then the one-step-model, the quantum mechanical correct derivation of the photocurrent, is briefly outlined. Following that, the spectral function and its line forms are introduced which will be needed in later chapters. Finally, this introductory chapter concludes with some remarks regarding the experimental setup. All of the above, the three-step-model, the one-step-model, the spectral function and experimental setup of photoemission and especially, angle resolved photoemission is extensively discussed in the literature, as e.g. in the books of Hüfner [107] and Schattke and Van Hove [108] as well as in various review articles [9,109].

3.1 The Photoemission process and the three-step-model

A sample exposed to light will emit electrons. This phenomenon, called the photoeffect [110,111], is the basis of Photoemission spectroscopy. Fig. 3.1 shows a simplified sketch not only of the photoeffect, but already of angle resolved photoemission (ARPES). In ARPES the photoelectrons are measured regarding their kinetic energy and their emission angle. To leave the sample the outcoming electrons have to gain a sufficient amount of energy from the incoming photons to overcome their binding energy E_B as well as the material specific work function Φ. Therefore, the kinetic energy of the photoelectrons will be related to the energy $h\omega$ of the exciting photons like

$$E_{kin} = h\nu - e\Phi - E_B \tag{3.1}$$
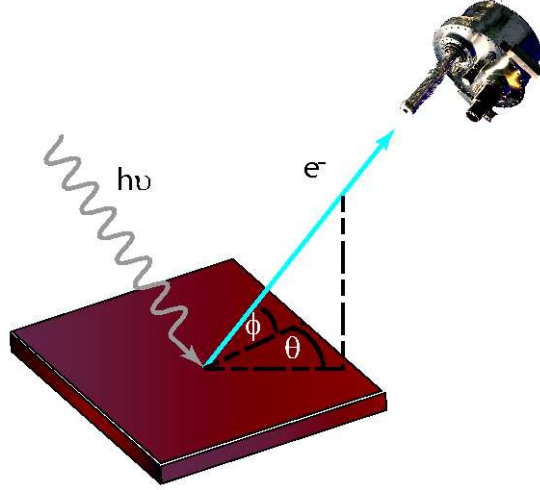
Figure 3.1: *A sketch of the photoemission process. Photons with energy hν imping on the sample. Electrons are detected regarding their kinetic energy and emission angle Θ and Φ.*

As stated in ARPES also the emission angle is detected. That facilitates to record the actual band structure in the Brillouin zone of a crystal, since the electron impuls outside the crystal and the wave vector **k** inside the crystal are related. Plotting the intensity of emitted electrons over their kinetic energy gives a so-called energy distribution curve (EDC). Fig. 3.2(a) shows EDC's as measured at different emission angles while in fig. 3.2(b) the corresponding energy distribution map is shown, where intensity is indicated by color and plotted over emission angle and energy.

In a simple way the photoemission process can be explained within the so-called three-step-model. It is based on the work of Berglund and Spicer [112] and gives a phenomenological description of the photoemission process which is here divided into:

1. Excitation of electrons within the solid

2. Transport to surface and scattering

3. Escape of the electron into vacuum

In the following each of the above shall be discussed in more detail.

Excitation of electrons

Assuming the one-particle approximation the photoemission excitation process can be described quantum mechanically by Fermi's Golden Rule which gives the probability ω_{fi} of the excitation from an initial state Ψ_i into a final state Ψ_f:

$$\omega_{fi} = \frac{2\pi}{\hbar} \left| \langle \Psi_f(\boldsymbol{k_f}) \left| H \right| \Psi_i(\boldsymbol{k_i}) \rangle \right|^2 \delta \left(E_f - E_i - \hbar\omega \right) \tag{3.2}$$
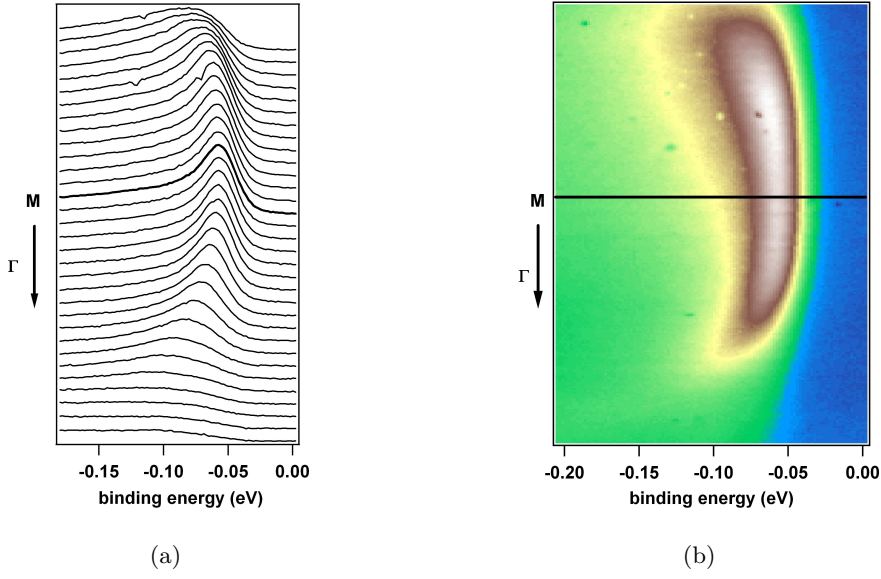
Figure 3.2: *(a) EDC at different emission angles around M along the ΓM line of a Bi2212 single crystal. The M point is indicated by the bold line. (b) Energy distribution map of (a): Intensity of photoelectrons (color code) plotted over binding energy and emission angle.*

Here the Hamilton operator $H = \frac{e}{2mc} \boldsymbol{A} \cdot \boldsymbol{p}$ with the vector potential $\mathbf{A}$ of the photon field and the impuls of the electron $\mathbf{p}$ are all given in the dipole approximation. In principal the whole photoemission process can be described by equation (3.2). However, the matrix element cannot be exactly calculated which complicates the matter considerably. Therefore, in the simple model discussed here, instead of dealing with the emission process in its whole, only the excitation *within* the solid is considered. This means, the final state describes an excited electron which is still in the solid, although it already has its final energy. Thus, Ψ_f and Ψ_i are bulk Bloch waves. The internal energy distribution of photoexcited electrons is then:

$$N_{int}(E, \hbar\omega) \propto \sum_{f,i} |M_{if}(\boldsymbol{k})|^2 \, \delta \left(E_f - E_i - \hbar\omega \right) \delta \left(E - [E_f - \phi] \right) \qquad (3.3)$$

$M_{if}(\boldsymbol{k})$ is the matrix element of the transition from initial to final state. The first δ-function secures the energy conservation of the excitation process while the second δ-function provides for energy conservation once the electron is measured outside the sample.

Transport to the surface

Still within the sample the excited electron will experience scattering on its way to the surface. While scattering at phonons is taking place only in the low energy regime, electron-electron scattering is the dominant scattering channel and influences the elec-

tron mean free path $\lambda(\epsilon)$ considerably. The latter is dependent on the dielectric function $\epsilon(q, \omega)$ and therefore varies from material to material. Within the theory of Fermi liquids, however, λ is solely dependent on the plasma frequency, which in turn depends on the mean distance r_s of electrons. Crystals that can be described in this model follow a "universal" function[107]:

$$\lambda^{-1} \approx \sqrt{3} \frac{a_0 R}{E_{kin}} r_s^{-\frac{3}{2}} \ln \left[\left(\frac{4}{9\pi} \right)^{\frac{2}{3}} \frac{E_{kin}}{R} r_s^2 \right] \tag{3.4}$$

where $a_0 = 0.529$ Å is the Bohr radius und R = 13.6 eV Rydberg energy. r_s is given in units of a_0. Fig. 3.3 shows the theorectical curve for λ as well as measured values for some metals. As can be seen, at typical ARPES photon energies of several eV electrons have an escape length of only a few Ångstrom. This emphasizes the surface sensitivity of photoelectron spectroscopy.
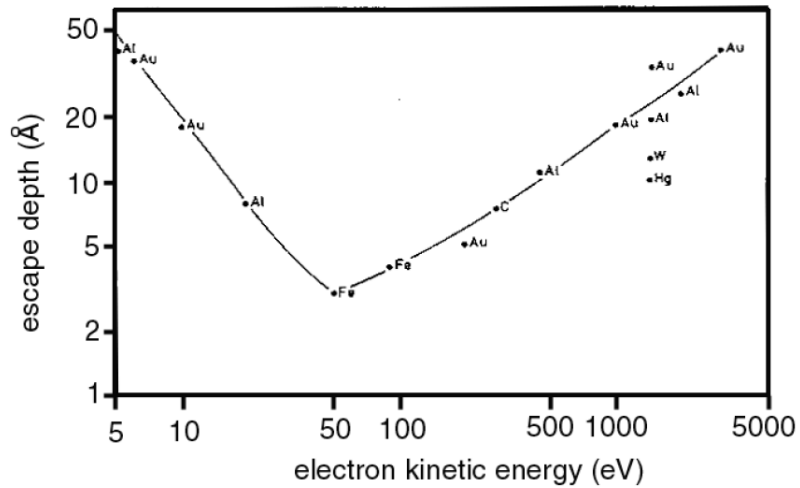
Figure 3.3: *Electron mean free path λ vs. kinetic energy of electrons. The "universal" curve and measured data for different metals are shown.[107].*

Berglund and Spicer[112] found in a classical treatment that the transport can be described by just a factor $d(E, k)$ in the calculation of the photocurrent.

Escape of the electron into vacuum

This step is treated in a purely classical manner disregarding quantum mechanical scattering processes at the surface. To leave the sample the excited electron has to have enough impuls normal to the surface ($\mathbf{k}_\perp$) to be able to overcome the potential barrier. As illustrated in fig. 3.4, passing the surface the electron experiences diffraction where only the parallel component of the wave vector $\mathbf{k}$ is conserved according to the Fresnel equations.
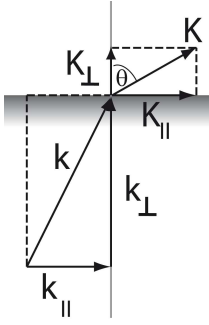
Figure 3.4: *Emission of the photoelectron. Only the parallel component of k is conserved when the electron passes the surface.*

Therefore in angular resolved measurements only $\mathbf{k}_\parallel$ can be directly detected. It results to:

$$\boldsymbol{k}_\parallel = sin\theta \left(\frac{2m}{\hbar^2} E_{kin}\right)^{\frac{1}{2}} \quad (3.5)$$

Within the three-step-model the escape into vacuum is described by a total transmission factor $T(E_f, \mathbf{K}_\parallel)^2$ which includes all the transmission factors of the individual Bloch waves.

In order to formulate the photocurrent within the three-step model all three steps have to be combined. The above given equation (3.3) for the internal energy distribution thus becomes:

$$N(E, \boldsymbol{k}_{\parallel,\boldsymbol{int}}, \hbar\omega) \propto \sum_{f,i} |M(\boldsymbol{k_f}, \boldsymbol{k_i})|^2 \, d(E_f, \boldsymbol{k_f}) \left|T(E_f, \boldsymbol{K}_\parallel)\right|^2$$

$$\times \delta\left(E_f - E_i - \hbar\omega\right) \delta\left(E - [E_f - \phi]\right) \quad (3.6)$$

3.2 Outline of the one-step model

The three-step-model is a good starting point for considering the photoemission process. It does, however, not treat the impact of scattering within the sample and surface effects in an exact manner. In fact often these are set to unity. To derive the photocurrent in a quantum mechanically exact way the Fermi Golden Rule (eq. (3.2)) would have to be calculated straightforwardly. An Ansatz for this was given first by Pendry [113] which was called the one-step model. If the initial and final state wave functions are known, all of the physics of the photoemission process is covered by eq. (3.2). The initial state Ψ_i has to be an Eigenstate of the N-electron system and the final state Ψ_f one of the ionised (N-1)-electron system of the semi-infinite crystal. Ψ_f contains a component propagating in the vacuum which resembles the photoelectron to be detected. Furthermore Ψ_f also has to have an amplitude within the crystal in order to compute the transition matrix element $M_{if}(\boldsymbol{k}) = |\langle \Psi_f(\boldsymbol{k_f}) |H| \Psi_i(\boldsymbol{k_i}) \rangle|^2$. Adequate wave functions for the final state to fulfill those premisses can be deduced from the time-reversed LEED-states. But still, various approximations have to be made to make an actual calculation possible. The reader may be refered to the book of Hüfner [107] or Schattke and Van Hove [108] and references therein.

3.3 Interpretation of spectra - line forms

After discussing the photoemission process, the line forms of the resulting spectra shall be considered. Here, especially the impact of strong correlations existent in the cuprates

is of interest. This can be treated within the Green's function formalism Mahan for details see e.g.[114], Nolting for details see e.g.[115]). The Green's function for the case of non-interacting electrons is given as:

$$G^0(\boldsymbol{k}, E) = \frac{1}{E - E^0(\boldsymbol{k}) - i\delta} \tag{3.7}$$

Electron-electron interaction can be included by adding the so-called self-energy $\Sigma(\boldsymbol{k}, E) = Re\Sigma + iIm\Sigma$ to the single-particle electron energy E^0. The Green's function then becomes:

$$G(\boldsymbol{k}, E) = \frac{1}{E - E^0(\boldsymbol{k}) - \Sigma} \tag{3.8}$$

The imaginary part of the Green's function is related to the one-particle spectral function which covers the spectrum of possible excitations. (Nolting see for instance[115]):

$$A(\boldsymbol{k}, \omega) = -\frac{1}{\pi} Im\left[G\left(\boldsymbol{k}, \omega\right)\right] \tag{3.9}$$

using eq. (3.8) the one-particle spectral function results to:

$$A(\boldsymbol{k}, \omega) = \frac{1}{\pi} \frac{Im\Sigma}{(E - E^0(\boldsymbol{k}) - Re\Sigma)^2 + (Im\Sigma)^2} \tag{3.10}$$

It can be deduced from the above equation that the real part of the self-energy rescales the electron dispersion while the imaginary part mainly changes the width of the spectral function compared to the non-interacting case. Then assumptions have to be made about the actual form of the self-energy. For instance in Fermi-liquid theory the self-energy would be: $\Sigma = aE + ibE^2$.

This influence on the lineshape is caused by electron-phonon and electron-electron interactions. Thus, there are self-energy corrections as discussed above for the inital state. Furthermore, broadening of the final state linewidth, which is primarily due to electron damping, and inelastic scattering occurs. Additionally, the interaction of photo-electron and photo-hole has to be considered. Smith et al.[116] showed that final state broadening can be neglected in quasi-two-dimensional materials. Moreover, if the 'sudden approximation' is valid, also the interaction between photo-hole and photoelectron can be neglected. Within the 'sudden approximation' it is assumed that the electron system reacts instantaneous to the disturbance of the excited electron and that the emitted photoelectron does not interact with the remaining electron system of the crystal. In the cuprates a case can be made for the validity of the 'sudden approximation'[109]. Thus, in cuprates the photocurrent can be interpreted in terms of the initial state spectral function:

$$I(\boldsymbol{k}, \omega) \propto \{M\left(\boldsymbol{k}\right) \times A(\boldsymbol{k}, \omega) f(\omega, T)\} \otimes R(\boldsymbol{k}, \omega) + B(\omega) \tag{3.11}$$

$M\left(\boldsymbol{k}\right)$ transition matrix element

$A(\boldsymbol{k}, \omega)$ one-particle spectral function
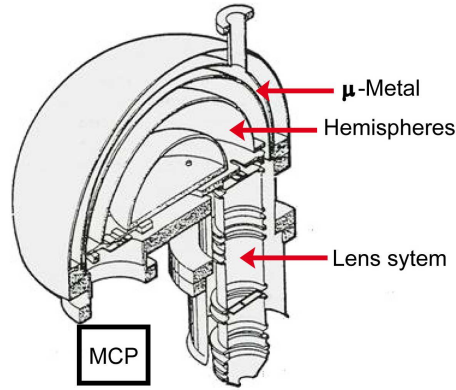
Figure 3.5: *Sketch of a hemispherical analyzer. The two hemispheres and the electron lens system is indicated. One can also see the μ-metal shielding which screens from magnetic fields.*

$f(\omega, T)$ Fermi function

$R(\boldsymbol{k}, \omega)$ resolution of the experiment folded over the spectral function

$B(\omega)$ background

Within this equation further broadening by the resolution of the measuring setup and thermal effects are included. Both of them can be seen as Gaussians folded over the spectrum. These issues are more extensively discussed in books and reviews[9,107,109,117].

3.4 Remarks to experimental setup

As discussed in section 3.1 the mean free path of electrons is not very high for photon energies of 5-50 eV which is the typical range for valence band photoemission. Therefore samples have to have a clean surface. This in turn makes high vacuum of 10^{-10}mbar obligatory for photoemission experiments. But it is also mandatory for maintaining a good intensity of photons considering that some gases, like oxygen or nitrogen, already absorb photons with an energy of 6 eV.

The hemispherical analyzer

For detecting the emission angle and energy of the photoelectrons, hemispherical analyzers are the most prominent choice. In the sketch of fig. 3.5, the two hemispheres can be seen. Between the two an electrical field is applied which lets the electrons pass according to their kinetic energy. For better energy resolution over a wide energy region, the electrons are all accelerated to a certain energy, the pass energy, before entering the

hemispheres. This is done by the electronic lenses. They also sort electrons coming in at different angles onto different spots on the multi-channel-plate which is situated behind the exit slit. This way, a two-dimensional image like that of fig. 3.2(b) can be recorded in one measurement.

Synchrotron radiation

Photoemission experiments require a highly monochromatized photon source with high intensity. This can be a Helium lamp but synchrotron radiation additionally provides the possibility of tuneable photon energies. In a synchrotron ring electrons are circling with relativistic velocities kept on their orbit by bending magnets. While radially accelarated, the electrons emit the so-called synchrotron radiation. Its spectrum and angular dependence can be calculated. Here, it shall only be pointed out that synchrotron radiation is linearly polarized in the plane of the particle orbit, and that the spectrum of synchrotron radiation behind a bending magnet is continuous in a frequency range from the infrared to the x-ray region. Photons with a smaller energy range can be produced within an undulator. Here an array of magnets is arranged to produce a periodically changing field, which redirects the electrons on a sinusoidal curve. The electrons will then emitt radiation directed along the axis of the undulator. Because of interference almost monochromatized light is produced, which is also greatly enhanced in intensity.

An undulator, however, cannot monochromatize the radiation sufficiently to carry out high resolution experiments. Additionally, depending on the application and desired energy range and brilliancy, different monochromators are used like Normal-Incidence- (NIM) or Plane-Grating-Monochromators (PGM). As the name suggests, a PGM works with a plane grating. Optical abberrations are corrected by mirrors. The type and positioning of mirrors depends on the specific setup of the beamline. An advantage of a PGM is the great energy range and the high throughput. The photoemission experiments reported in this thesis were done at the Synchrotron Radiation Center (SRC) and the Berliner Elektronen Speicherring für Synschrotronstrahlung (Berlin Electron Storage Ring for Synchrotron Radiation - BESSY) using a PGM at the undulator beamlines U3 and U-112, respectively.

4

X-ray Absorption Spectroscopy

In this chapter theoretical aspects of X-ray absorption spectroscopy (XAS) will be presented. After an introduction into the basic concepts, excitonic effects and line forms at absorption edges are discussed. Then, the here employed technique of 2p core XAS in cuprates is described. At the end details about instrumentation and data processing are given.

4.1 Introduction

XAS is a powerful local probe that measures the unoccupied density of states at the site of the excited atom and provides information about bonding characterictics, oxidation states and geometry around the absorbing atom. Especially for transition metal oxides 2p-core-XAS served as a sensitive tool experimentally resolve open questions regarding the ground state in these materials[118]. Exploiting polarization effects gives additional information about orbital occupation, crystal fields or spin[119].

Radiated on a sample, x-ray photons are either scattered or absorbed by the sample's electron system. This absorption and hence the absorption coefficient of the sample is measured in XAS. The absorbing electron can be excited either into the continuum, which means the creation of a photoelectron, or into an unoccupied state below the vacuum level. In the latter case two relaxation processes may occur, both of which are sketched in fig. 4.1:

1. The relaxation of the excited electron into its ground state under emission of a fluorescence photon containing the energy difference between initial (ground state) and final (excited state) state.

2. The Auger-process, where the core hole is filled by an outershell electron and another electron with an energy equal to the difference in orbital energies can be emitted.
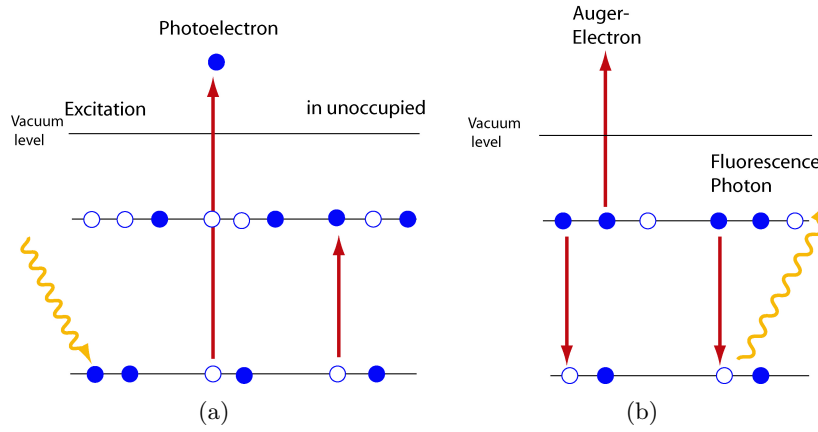
Figure 4.1: *(a) After absorption of the incoming x-ray photon either a photoelectron is emitted or the absorbing electron is excited into unoccupied states.The relaxation of the latter takes place via emission of a fluorescence photon or Auger electron as illustrated in (b).*

The most direct way of measuring the absorption coefficient is to detect the transmitted photons. This is not always experimentally possible and, as will be mentioned later, by detecting the relaxation processes rather than the absorption itself additional information can be gained. The absorption coefficient can be derived from both, Auger emission and fluorescence. They are, however, competing processes. Their occurance is strongly related to the atomic number of the absorbing atom in the probed sample and to the absorption edge. Generally, the probability of Auger emission is higher in light elements, and that of fluorescence in heavy elements. At the atomic number Z=30 both processes are equal in ocurrence for absorption measurements at K-edges, at the L_3, L_2 or L_1 edge, however, the Auger process dominates up to elements with Z=90.[120] Details of the detection of both processes are given in section 4.3. In principle the absorption process can be described like the excitation process of ARPES with Fermi's Golden Rule (3.2). So the absorption coefficient results from:

$$\mu(E) \sim \sum_{i,f} \langle i \mid \mathbf{er} \mid f \rangle \delta(E_f - E_i - \hbar\omega) \tag{4.1}$$

where the Hamilton operator of the electron-photon interaction

$$H = -i\hbar \frac{e}{c} \mathbf{A} \sum_j^N e^{ik \cdot \mathbf{r}_j} \mathbf{n} \cdot \bigtriangledown_j \tag{4.2}$$

has been reduced to a dipole operator since the wave vector $\mathbf{k}$ of the photons is small and the exponential function can be set to unity. The initial and final states denoted $\langle i \mid$ and $\mid f \rangle$ in eq. 4.1 are single particle states assuming that the wave functions of the passive electrons and the unoccupied states are not affected by the core hole. From eq. 4.1 the whole process can be computed. The difference to the ARPES measurement lies in the
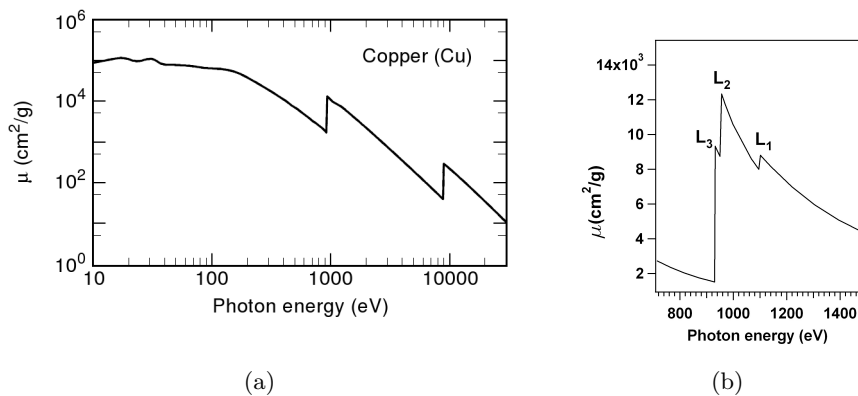
Figure 4.2: *(a) Absorption coefficient of copper. (b) Enlargement of the energy region of the L-edges.*

final state. While in ARPES the final state is an emitted photoelectron, in XAS the final states are the unoccupied density of states. The measured spectra are a convolution of initial and final states, and therefore, in XAS one is basically measuring a convolution of both, occupied and unoccupied states. The occupied states are, however, core states which are represented by δ-peaks in the density of states. Hence, in case the one-electron theory and above made assumptions are valid, one can probe the unoccupied density of states in XAS. Since in the whole process strict dipole selection rules apply it is possible to gather exact information on the ground state because possible final states depend strongly on the initial state. The rough evolution of the absorption coefficient over energy is shown exemplary in fig. 4.2. Absorption increases drastically at the so-called absorption edge. There, the absorbed energy is just sufficient to excite an electron from one specific shell into the continuum. The edges are labeled according to the shells the electrons are escaping from.

The whole excitation process basically takes place within the range of one atom, and thus XAS is a very local probe[121]. Even in solid samples the XAS spectra can be interpreted as if only one atom or molecule would be measured. In transition metal ions also the ligand has to be included since energy levels change by ligand field splitting as discussed in chapter 1.2.1.

On their way out of the sample, the electrons experience scattering with other electrons. While electrons with high kinetic energy have a single-scattering path, electrons with low kinetic energy are multiply scattered (see fig. 4.3). The latter results in oscillations of the absorption signal from which structural information can be gained. Different XAS regions can be derived accordingly as depicted in fig. 4.3. In this work only the edge region is studied, and therefore features further away from the edge, especially above mentioned oscillations, will not be discussed in this introduction.
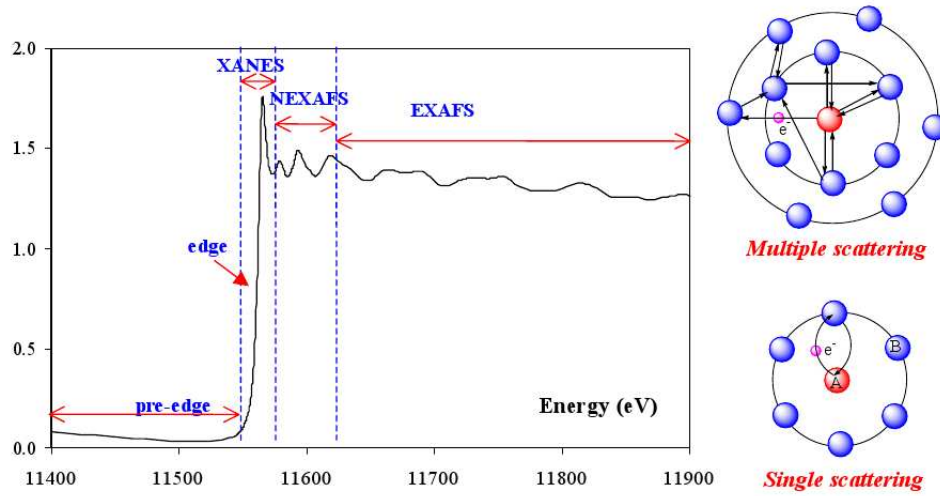
Figure 4.3: *Shown is an examplary XAS spectrum. In the X-ray absorption near edge spectroscopy (XANES) and Near edge x-ray absorption fine structure (NEXAFS) region multi-electron scattering dominates. In the Extended x-ray absorption fine structure (EXAFS) region there is only single scattering. Interesting for the work presented here is the edge and XANES region. On the right multi- and single-electron scattering are sketched.*

4.2 2p XAS - edges and excitons

The creation of a core hole in a 2p core shell and hence the absorption at L-edges is refered to as 2p XAS. The 2p-core electron is close to the core and therefore shows considerable splitting from spin-orbit-coupling. This results in different L-edges, namely L_2 and L_3, for the spin quantum numbers j=$\frac{1}{2}$ and j=$\frac{3}{2}$, respectively. In the inset of fig. 4.2 the L-edge is magnified to show this structure.

While the picture given in the introduction so far is adequate for ideal cases, especially in correlated electron systems a closer look at the edge (fig. 4.3) reveals extra spectral feature that are unaccounted for in the model discussed so far. When the core hole is not anymore efficiently screened by the surrounding electron system, the one-electron approximation used in the section above becomes insufficient[122–124]. Core hole and excited electron interact constituting an exciton which is visible below the continuum threshold as a high intensity peak - a so-called white line. The core hole potential acts so strongly that the excited electron is kept closely around the atom in a bound state. Thus in the absorption measurement only some intensity results from excitation from 2p to 3d which are not bound into the exciton. This intensity is measured above the threshold. All other intensity remains in the bound excitonic state and gets piled up at lower binding energies forming the white line. Hence, the shape of the distribution of the unoccupied density of states cannot be revealed anymore by the absorption experiment.

However, the intensity is still related to the number of unoccupied states. Such excitons arise particularly at the L-edges of transition metals and are therefore relevant in the L_3 edge of copper as studied in this thesis.

Because of the sudden creation of the core hole potential multi-electron excitations may occur which lead to satellites in the spectrum. These can have a higher or lower binding energy and are sometimes named shake-up and shake-off satellites accordingly. Moreover, the Coulomb potential of the core hole lowers the energy of the states of the absorbing atom. Thus, charge can be transfered from the ligand to the transition-metal-ion in materials with narrow bands and strong correlations[107,123,124]. The resulting satellites are named charge-transfer satellites. In XAS the excited electron is still around the core hole and adds to its screening. Thus, only small charge-transfer satellites appear in XAS as in opposition to X-ray photoemission, where satellites are much more important[124].

4.3 Instrumentation

The most direct way of an absorption experiment is the measurement of the transmission signal. Due to experimental limitations like sample thickness this is usually not feasible for high-T_c single crystals. Hence, processes that are proportional to the absorption of the photons, like fluorescence and Auger emission (see section 4.1), have to be detected. The simultaneous detection of these is favorable since the first gives information about the bulk properties of the sample, while the second originate within 30 Å of the surface. The fluorescence signal, however, suffers from selfabsorption. Because of the great penetration depth of the x-ray photons, the fluorescence photons are absorbed on their travel to leave the surface. Thus secondary fluorescence photons are produced. In opposition to that, the electron yield correlates directly with the absorption coefficient[124,125].

Measurements presented in this work were done at the ISIS, PM3 and U41-PGM beamline of BESSY. ISIS and PM3 are dipole beamlines equipped with a Plane Grating Monochromator (PGM), while U41-PGM is an undulator beamline with a PGM. Some remarks on synchrotron radiation and PGM's are given in chapter 3.4. The experiments were carried out using the HU/BESSY XAS chamber FLUORO which is sketched in fig. 4.4. The sample sits on a manipulator with 5 degrees of freedom. Electron and fluorescence yield are recorded simultaneously with a Ge-detector and a channeltron, respectively. The fluorescence-detector utilizes the semiconducting characteristics of Ge. X-rays excite electron-hole pairs proportional to the number of impacting photons. Thus a pulse can be measured. A channeltron is basically a vacuum-tube with a high resistance coating on the inside. Incoming electrons colliding with the wall induce emission of secondary electrons which are accelerated by the voltage between cathode and anode. Electrons are multiplied from wall to wall on their way towards the anode. There a whole cascade of electrons has developed.

In the experiments reported here only electrons above a certain energy are collected what is called partial electron yield. The cutoff energy is set to 100 eV. Therefore all Auger and photoelectrons with a kinetic energy of more than 100 eV are counted at every energy step. Secondary electrons are cut off which greatly improves the signal to noise
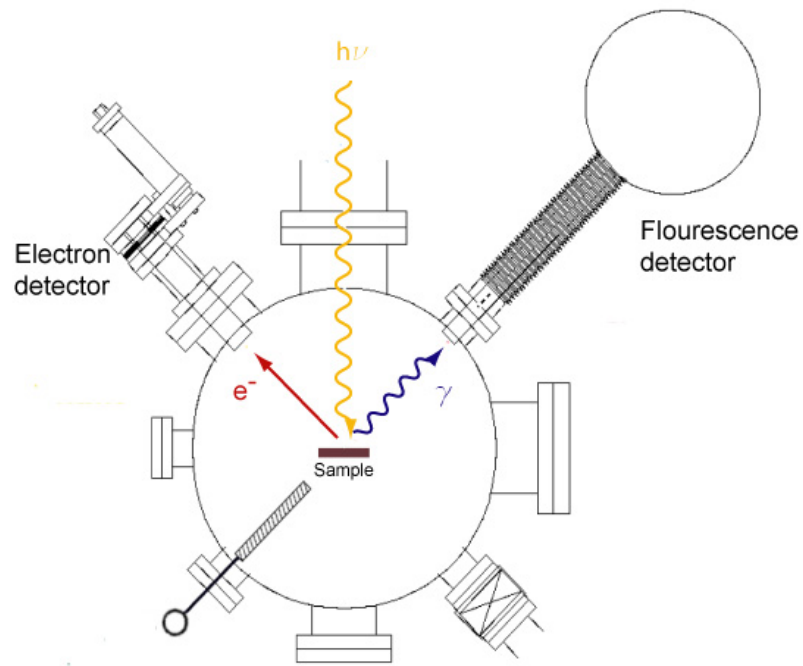
Figure 4.4: *Sketch of the HU/BESSY XAS chamber FLUORO. Electron (red arrow e⁻) and fluorescence yield (curved blue arrow γ) detector are indicated as well as the position of the beamline (yellow curved arrow hν).*

Transition	K1s	$L_1$2s	$L_2$2p$_{1/2}$	$L_3$2p$_{3/2}$	$M_1$3s	$M_2$3p$_{1/2}$	$M_3$3p$_{3/2}$
	8979	1096.7	952.3	932.7	122.5	77.3	75.1

Table 4.1: *Electron binding energies in eV for Cu. From the X-ray Data Booklet*[126]

ratio. Since the contribution of the primary photoelectrons varies with photon energy and, when studying single crystals, also with sample orientation, their direct detection is not desireable. Considering the possible photoemission peaks (see table 4.1) it is evident that at the edge only the Auger emission is measured while relevant photoemission lines are the same in the scanned region below and above the edge so that they have the same contribution to the background over the whole spectrum. Photoemission from the valence band comes into play above the edge but not within the XAS region of interest.

5

Polarization dependent XAS on (Pb,Bi)2201

The ground state of cuprates including the orbital occupation can be investigated by XAS at the CuL_3 and OK edge. Furthermore, using CuL_3 XAS the hole concentration can be determined directly in the CuO_2 plane. Within this thesis polarization dependent XAS studies were carried out on the single layer Bi-cuprate (Pb,Bi)2201. While previously only out-of-plane polarization dependencies were studied, now a polarization dependence within the CuO_2 plane has been detected. It modulates spectral features related to the Zhang-Rice singlets (ZRS). Its characteristics over angle reveals signatures that move beyond the $d_{x^2-y^2}$ symmetry expected from one-band models based on $d_{x^2-y^2}$ symmetric ZRS and point towards the inclusion of axial orbitals as proposed by Andersen et al.[58].

Furthermore, accounting for the found in-plane polarization dependence allows to refine the method of hole content determination by CuL_3 XAS making it applicable on single crystals. A detailed study of the superconducting dome in single crystalline single layer Bi cuprates (Pb,Bi)2201 was conducted by Ariffin et al.[127].

In the following chapter, first, the line shape at the CuL_3 and OK edges and the method of measuring the hole concentration in polycrystalline cuprates using CuL_3 XAS will be explained. Then, after introducing the well known out-of-plane polarization dependence, the newly found polarization dependence within the plane and possible origins will be discussed. Furthermore, the results will be put in relation to the theory of the electronic structure of the cuprates. Finally, the refinement of the method of hole content determination for single crystals[127] is briefly explained, and the phase diagram specific to the single and double layer Bi cuprates is given. The latter will complete the introduction of the Bi cuprates given in chapter 2 and be a preliminary for the discussion of the photoemission measurements of the next chapter.

5.1 *CuL_3 lineshape in cuprates*

In transition metal compounds and especially in the cuprates the unoccupied states lie in the Cu3d shell. The initial state configuration for the undoped cuprates is $Cu3d^9$. Hence,

the core electron is excited into this shell. In the charge-transfer model of the cuprates introduced in chapter 1.2.2 this corresponds to filling the Cu3d states of the upper Hubbard-band. This excitation is dipole allowed and consequently has good intensity creating the white line in the XAS spectra. It can be written as:

$$2p^6 3d^9 \longrightarrow 2p^5 3d^{10} \tag{5.1}$$

The excitonic character of this transition can be observed in fig. 5.1 where a CuL_3 spectrum of a doped Bi-2201 single crystal is shown. The assignement of the excitation could be achieved by comparison to CuO [128].
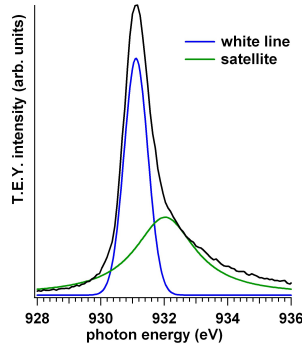
Figure 5.1: *XAS spectrum of the CuL_3 edge consisting of white line and satellite which are represented by two Voigt profiles as derived by fitting.*

Doping of the cuprates adds holes on the ligand oxygen [129] and leads to a satellite situated at higher photon energies (lower binding energies) in the XAS spectra. This satellite can also be seen in fig. 5.1. It stems from the excitation:

$$2p^6 3d^9 L^{-1} \longrightarrow 2p^5 3d^{10} L^{-1} \tag{5.2}$$

where L denotes the ligand, and L^{-1} a ligand hole. The physical explanation of this satellite however was at first debated. The satellite's energy position corresponds to formally trivalent $Cu3d^8$ as can be derived from a comparison with trivalent Cu compounds, like e.g. $NaCuO_2$ [128,130]. This led to the opinion that doped cuprates are a mixture of divalent and trivalent Cu sites which shall be explained now in more detail. Divalent Cu compounds have an initial state configuration of $3d^9$. By charge transfer from the oxygen ligand, a second initial state with a hole on the ligand becomes possible. Both states mix and lead to the initial state configuration:

$$\alpha \mid 3d^9 > + \beta \mid 3d^{10} L^{-1} > \tag{5.3}$$

where α and β depend on the degree of hybridization. Since in the second initial state the Cu3d shell is filled, there results no additional final state from eq. 5.1. This is the situation in undoped cuprates. In trivalent Cu compounds like e.g. NaCuO, however, the initial state is $Cu3d^8$. Two additional initial states become possible by charge transfer. The complete initial state configuration is then:

$$\alpha \mid 3d^8 > + \beta \mid 3d^9 L^{-1} > + \gamma \mid 3d^{10} L^{-2} > \tag{5.4}$$

and now there exist two final states:

$$2p^6 3d^8 \longrightarrow 2p^5 3d^9 \tag{5.5}$$
$$2p^6 3d^9 L^{-1} \longrightarrow 2p^5 3d^{10} L^{-1}$$

But actually, in doped cuprates the $2p^5 3d^9$ final state of eq. (5.5) could not be observed[128,130]. Therefore, also the explanation of a mixture of divalent and trivalent copper sites in doped cuprates became questionable. Instead the occurence of the charge-transfer satellite could be established[128,131,132]. It is one argument in favor of doped holes in cuprates being located rather on oxygen than on copper[122,129]. Having one hole on the Cu and one on the ligand oxygen which results from doping, the initial state of the satellite transition corresponds to a Zhang-Rice singlet as discussed in chapter 1.2.2. Hence, probing this state gives information on the Zhang-Rice singlet state in the CuO_2 plane.

5.2 OK lineshape in cuprates

The electronic structure of the cuprates is dominated by that of the CuO_2 plane as discussed in chapter 1.2.2. Cu and oxygen are strongly hybridized. The Zhang-Rice singlet and the Upper Hubbard band are each made up of Cu3d and O2p states. XAS CuL_3 edge introduced in the previous section probes the contribution of Cu. It is, of course, also possible to probe that of oxygen by performing XAS at the OK edge.

In opposition to the situation at the CuL_3 edge, the core hole at the OK edge is better screened allowing only small excitonic effects. Hence, the determination of the actual shape of the unoccupied density of states is viable as expected from a simple one-electron picture as discussed in the introduction of this chapter. This is supported by comparison of OK spectra with theoretical calculations[133,134].

A specialty of the charge-transfer insulators is the possibility to fill the UHB by charge transfer of an electron from the ligand oxygen into the Cu3d level ($3d^{10}L^{-1}$). This is the initial state for the x-ray absorption process that creates an O1s core hole on the ligand oxygen. The excited electron then fills the hole from the charge transfer in the O2p orbital. Thus the initial state of the undoped compound eq. (5.3) leads to the transition

$$3d^{10}L^{-1} \longrightarrow O1s^{-1}3d^{10} \tag{5.6}$$

where the O2p states mixed into the Upper Hubbard Band (UHB) get filled by an oxygen core electron. Hence, probing the transitions of eq (5.1) and (5.6) the O2p and Cu3d states of the UHB can be detected.

In the doped compound the initial state configuration changes to that of eq. (5.4). Now at the OK edge two additional transitions are possible:

$$3d^9 L^{-1} \longrightarrow O1s^{-1}3d^9 \tag{5.7}$$
$$3d^{10}L^{-2} \longrightarrow O1s^{-1}3d^{10}L^{-1}$$

The latter initial state has low probability and therefore mainly the first transition occurs which is that with a strong Zhang-Rice singlet character. Here again it becomes evident that by performing CuL_3 and OK XAS the contribution of Cu3d and O2p to the electronic structure can be probed. Fig. 5.2(b) shows an absorption spectrum of the OK edge of doped Bi2201. There the first pre-peak is indicated with (A). It is assigned to
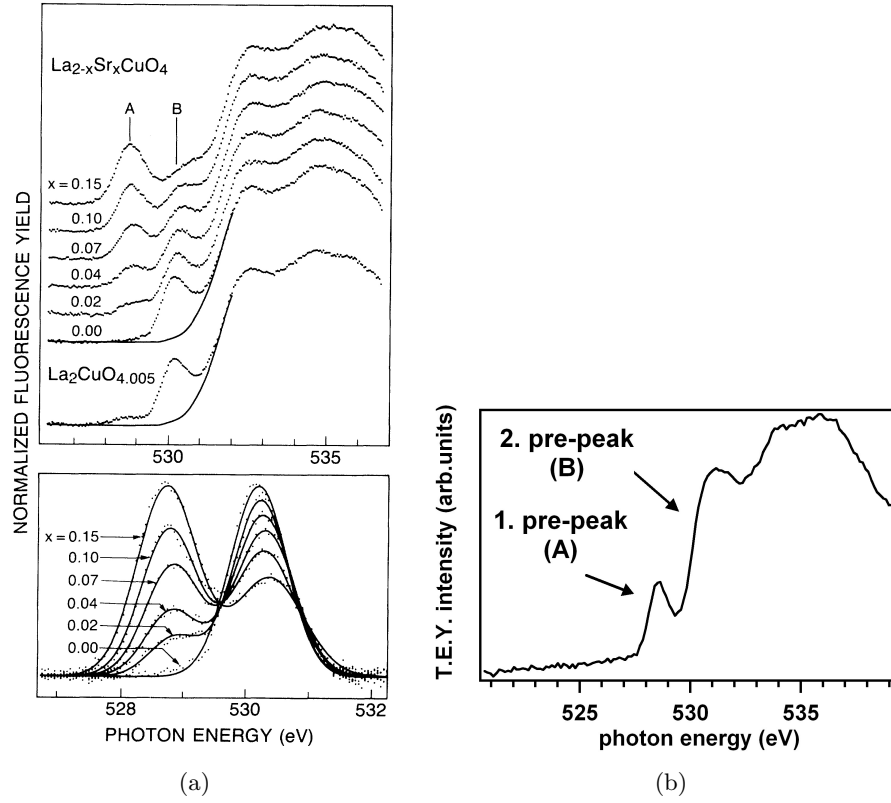
Figure 5.2: **(a)** *Shown in the upper graph are OK XAS spectra on $La_{2-x}Sr_xCuO_4$ at different doping levels taken from[135]. Dotted curves give the data, solid lines the background which was substracted to extract the first pre-peak labeled (A) and the second pre-peak labeled (B). The thus obtained pre-peaks A and B are plotted in the bottom graph. Here the solid lines represent the fit by Gaussians. It is evident that with higher doping A grows as B vanishes.* **(b)** *OK XAS on an Bi2201 single crystal with a hole concentration of n_h=0.19. The first pre-peak A can be well extracted while the second pre-peak B is partly covered by BiO states.*

the transition of eq. (5.7) and thus arises in doped cuprates only. The second pre-peak (B) stems from the transition of eq (5.6) and can be related to the UHB states. In other cuprates, as e.g. LSCO, this second pre-peak forms a real shoulder (see fig. 5.2(a)) and the UHB can be investigated. In Bi-cuprates, however, the BiO states overlapp with the UHB and thus this spectral feature cannot be as easily extracted. In Mott-Hubbard and charge-transfer insulators an anomalous transfer of spectral weight occurs from high to low energy, meaning states are transfered from the UHB to the ZRS band[136]. In the XAS spectra this is reflected by the rapid growth of the ZRS related first pre-peak and the concurrent decrease of the UHB related second pre-peak with doping as shown in fig. 5.2. This is not expected from standard band theory. In semiconductors for example the spectral weight is not influenced by doping. This anomalous transfer of spectral weight results solely from the strong correlations. It shall be mentioned here that the although weak excitonic effects occuring at the OK edge lead to the second pre-peak being an excitonic peak.

5.3 Hole content determination in polycrystals

The cuprates show a plethora of phases when doped with holes (see chapter 1.2.3). To study the physics of those different phases experimentally, the hole concentration of investigated samples has to be determined. Now, the determination of the hole content by CuL_3 XAS, a for high T_c research salient application of XAS, is described disregarding polarization effects. Hence, the method explained here is only applicable in polycrystals where the crystallographic directions are distributed statistically.

As discussed in chapter 2.3, in Bi(Pb)-2201 doping is not only achieved through cation substitution, also non-stoichiometric oxygen adds holes into the system. A merely chemical approach is thus difficult, especially, since the measurement of oxygen content is an experimentally formidable task. Additionally, all layers in the Bi-cuprates contain oxygen, but only the non-stochiometric oxygen in the BiO-layers is supposed to contribute to the hole doping in the CuO_2 plane (see sec. 2.3). Among the several methods to determine the hole content, there are some that measure it indirectly like e.g. thermopower and Hall measurements[137,138]. Others probe only the holes induced by non-stoichiometric oxygen but not by the cation substitution[139].

From the facts of the previous sections it is clear that the CuL_3 satellite and the first pre-peak in the OK spectra result from states directly related to doped holes. The white line will appear at the CuL_3 edge regardless of hole content because it is a process taking place locally on the Cu atom. The satellite, however, is a charge-transfer satellite. With rising hole concentration the intensity of the satellite will increase since the probability for the initial state of the corresponding transition increases. The process of charge transfer will thereby become more likely. Hence, the intensity of the satellite relative to that of the white line is a measure of the doped holes. It could indeed be shown that the satellite gains intensity with higher doping level and thus rising hole concentration[140]. The scaling factor between relative intensity and hole content was found to be one in polycrystals. So, to obtain a numerical value for the hole content simply the relative

intensity of white line and satellite has to be evaluated:

$$n_h = \frac{I_S}{I_{WL} + I_S} \tag{5.8}$$

where n_h are holes per Cu atom and I_S and I_{WL} are intensity of satellite and white line, respectively. CuL_3 XAS probes the holes directly in the CuO_2 plane regardless of being induced by non-stoichiometric oxygen or cations. That makes it a very straightforward tool for the determination of the hole content.

This method gave good results for polycrystalline materials, e.g. on $La_{2-x}Sr_xCuO_4$ by Ronay et al.[140], on $Bi_2Sr_2CaCu_2O_{8+\delta}$ by Ghigna et al.[141] and Pham et al.[142], on $Bi_{2-x}Pb_xSr_2Ca_{1-x}Y_xCu_2O_{8+\delta}$ by Merrien et al.[143] and recently by Schneider et al.[144] also on $Bi_2Sr_{2-x}La_xCuO_{6+\delta}$ and $Bi_{2-y}Pb_ySr_{2-x}La_xCuO_{6+\delta}$.

The work of Schneider et al.[144] also showed that a determination of hole content from the OK edge is more complicated. The first pre-peak grows in intensity with rising hole concentration and its area should also give a measure for doped holes. However, as shown in fig. 5.3(a), for Bi2201 single crystals the growth of the intensity of the first pre-peak seems to saturate in the overdoped regime. Or, at least the rate of spectral weight transfer changes drastically. This behavior was recently also found for LSCO, Tl-2201 and YBCO by Peets et al.[145] which is given for reference in fig. 5.3(b). Therefore, only the evaluation of the CuL_3 white line and satellite provide a reliable tool for hole content determination within the whole superconducting region.

(a)

(b)
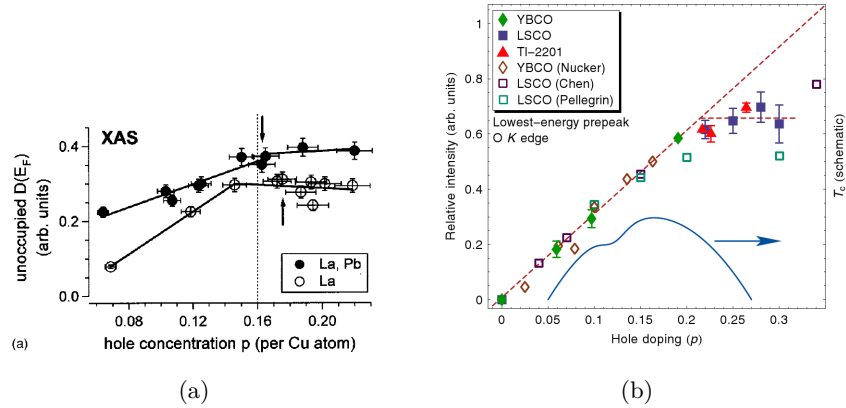
Figure 5.3: *The intensity of the first pre-peak over hole concentration, here referenced with p, saturates in the overdoped regime.* **(a)** *shows the measurement for La substituted, Pb-free Bi2201 polycrystals (open circles) and La and Pb substituted (Pb,Bi)2201 polycrystals (full circles). The figure is taken from Schneider et al.[144]* **(b)** *is taken from Peets et al.[145] and shows the same for LSCO, YBCO and Tl-2201 as denoted in the inset. Furthermore, the $T_c(p)$ curve is given schematically.*
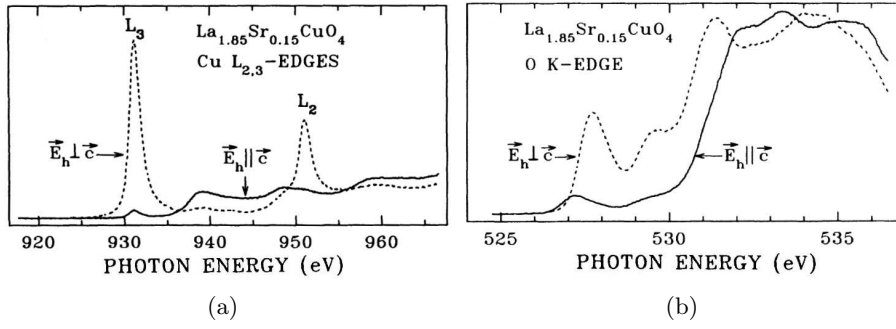
Figure 5.4: *Polarized XAS for in-plane and out-of-plane polarization taken from Chen et al.[3] (a) CuL_3 and CuL_2 edge of LSCO measured with $E \perp c$ and $E \parallel c$ as indicated. (b) Same for the OK edge. The spectral features connected to intrinsic and doped holes have highest intensity for polarization $\perp c$ and thus within the CuO_2 plane. With polarization perpendicular to it, the intensity is almost vanished.*

5.4 Polarization dependent XAS

After considering the transitions at the CuL_3 and OK edge of the cuprates, polarization effects shall be discussed. XAS is commonly done using synchrotron light which is either linearly or circularly polarized. Mostly, this is exploited in X-ray Magnetic Circular Dichroism (XMCD) or X-ray Magnetic Linear Dichroism (XMLD) where the intensity of excitations with defined polarization settings are related to orbital magnetic momentum or the alignment of spins[124]. A linear dichroism, however, can also be caused by asymmetric orbital occupation or crystal field splitting. The dependence on orbital occupation results from matrix element effects which are discussed in detail in Pellegrin et al.[146]. Considering as an example the excitation from s to p orbitals, it is evident that with x-,y-, or z-polarized light only the p_x, p_y, or p_z orbital, respectively, can be reached. Since s is always even, only polarization along the considered orbital gives a nonzero value of the matrix element $\langle s | \mathbf{x}, \mathbf{y}, \mathbf{z} | p_{x,y,z} \rangle$.

5.4.1 Out-of-plane polarization in cuprates

Asymmetric or non-cubic orbital occupation exists in the cuprates. According to the discussion in chapter (1.2.1) the hole of the $Cu3d^9$ configuration sits in the $3d_{x^2-y^2}$ orbital and thus within the CuO_2 plane. This has been experimentally probed by using linearly polarized light. Fig. 5.4(a) and 5.4(b) shows CuL_3 and OK spectra from Chen et al.[3] with the polarization vector of the incoming light parallel and perpendicular to the crystallographic **c** direction. At the CuL_3 and CuL_2 edge white line and satellite, the latter visible from the asymmetric lineshape, have high intensity with the vector **E** of the incoming light perpendicular to the crystallographic **c** direction, and thus polarization within the plane. With **E** parallel **c**, and thus perpendicular to the CuO_2 plane, the intensity of white line and satellite vanishes almost totally. The same effect occurs at the OK edge where first and second pre-peak have high intensity for **E** perpendicular **c** and

very low intensity for **E** parallel **c**. Hence, intrinsic and doped holes reside mainly within the plane as expected from theory. There is, however, some residual intensity in both spectra for polarization parallel to **c**. From this Chen et al.[3] calculated for intrinsic holes ~ 1 % Cu$d_{z^2-r^2}$ and ~ 4 % O2p$_z$ character. For doped holes the estimation is more complicated because of spectral weight transfer and hybridization effects. But it was deduced that the dominant out-of-plane orbital for doped holes is O2p$_z$. This dependence on the polar angle θ between the crystal **c**-axis and the **E**-vector of the incident light was explored in great detail also for other cuprate materials, e.g for Bi2212[147–149] and for YBCO[150].

5.4.2 Exploration of in-plane polarization dependencies

The last section introduced polarization dependent XAS on the cuprates. There, the discussed effect results from asymmetrical orbital occupation of in-plane and out-of-plane orbitals. This asymmetric occupation can be derived from the octahedral symmetry of the CuO$_6$ unit (refer to chapter 1.2.1). Within the plane, however, the unit cell has four-fold symmetry and no polarization dependence should occur. But, nevertheless, such an in-plane polarization dependence has been found within this work. In the following this polarization dependence will be treated in detail. Special attention will be paid to the angular distribution of intensity upon changing the in-plane polarization setting. Furthermore, a possible reason for the occurence of this unexpected polarization dependence will be given and implications for the electronic structure will be discussed.

This unexpected effect was explored by studying the absorption signal at the CuL$_3$ and OK edge of (Pb,Bi)2201 single crystals. Measurements in the surface sensitive total electron yield (TEY) mode and the bulk sensitive flourescence yield (FY) mode gave the same result. The changes occurring in the CuL$_3$ and OK spectra under variation of polarization geometry within the plane are illustrated in fig. 5.5(a) and 5.5(c). Especially the CuL$_3$ charge-transfer satellite and the first (low energy) OK pre-peak vary in intensity at different angles. Both are connected to the doped holes, and hence, related to the ZRS states. The intensity distribution over azimuthal angle of this modulated singnal is more complex than the d$_{x^2-y^2}$ symmetry expected from the hybridization of in-plane Cu3d$_{x^2-y^2}$ and O2p$_{x,y}$ orbitals. Thus, the observations point towards the inclusion of out-of-plane orbitals, specifically the axial hybrid orbital as proposed by Andersen et al.[58].

To achieve the desired polarization settings, the x-ray beam was incident normal to the sample and therewith also normal to the CuO$_2$ plane. Hence, the electrical field vector **E** of the incoming light lies within the CuO$_2$ plane. Polarization effects resulting from **E** lying out of the CuO$_2$ plane as described in the previous section are thus irrelevant in this setup. The XAS signal at the CuL$_3$- and OK-edge was recorded while rotating the sample continuously about 180° around the surface normal with a minimum increment of 2°. Thereby, the polarization geometry defined by the orientation of **E** with respect to the orbitals in the CuO$_2$ plane was altered.

The experiments were performed at the PM3- and ISIS-Beamline at BESSY using the HU/BESSY XAS chamber FLUORO. The synchrotron radiation was monochromatized
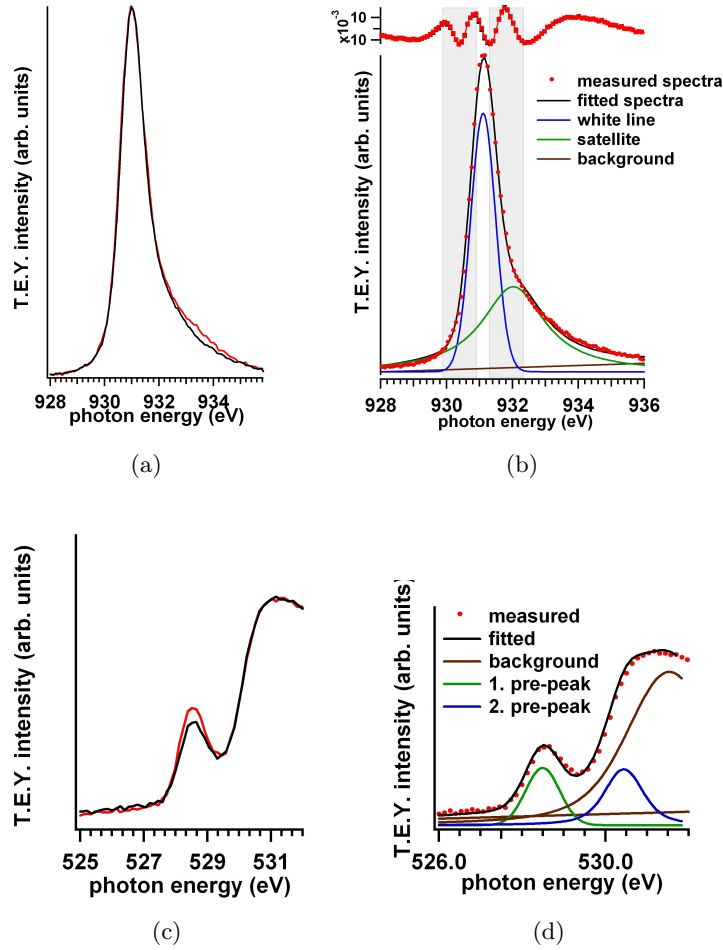
Figure 5.5: *(a) and (c) Spectra of the CuL_3 and OK edge for two different angles. Upon variation of polarization the spectra visibly differ in the spectral features connected to the doped holes. (b) Illustration of the fitting with Voigt profiles for CuL_3 spectra. Additionally, the residuals of the fit are drawn over the upper axis. Shaded regions indicate maximum deviation of the fit. There the line forms cross. (d) Example of the fitting model for OK spectra. The overlapp with BiO states was modeled with a Voigt-profile which is regarded as background. Hence, it is drawn with a solid brown line as the linear background.*

with a plane grating monochromator (PGM) behind a bending magnet with respective energy resolutions at the CuL$_3$ edge of <100 meV and <600 meV and at the OK edge of <75 meV and <200 meV. Beamlines and the experimental chamber were described in more detail in chapter 4.3. However, it shall be emphasized once again that the setup of the chamber allows the recording of both, TEY and FY, simultaneously with the respective detectors positioned on opposite sides each tilted 45° from the incident beam. The single crystals were cleaved in vacuum at a base pressure of better than $1 \cdot 10^{-9}$ mbar. All measurements were conducted at room temperature.

Single crystals of three systems of the single layer Bi cuprate (Pb,Bi)2201 have been studied covering almost the whole superconducting dome. In these three systems the hole doping was achieved by either La substitution or the variation of non-stochiometric oxygen (see also chap. 2):

1. $Bi_2Sr_2CuO_{6+\delta}$
   In four single crystals without cation substitution the varied doping level resulted from the different oxygen concentrations δ.

2. $Bi_2Sr_{2-x}La_xCuO_{6+\delta}$
   Two single crystals were doped by La substitution. The La concentration was x=0.62 and x=0.65.

3. $Bi_{2-y}Pb_ySr_{2-x}La_xCuO_{6+\delta}$
   5 single crystals had a La concentration of x=0.27, x=0.4, x=0.42, x=0.46, x=0.65 and a Pb level ranging from y=0.4 to y=0.5.

For a detailed analysis all spectral features - CuL$_3$ white line and satellite as well as both OK pre-peaks - were fitted with Voigt-profiles. The overlapp with BiO states at the OK edge was modeled with an additional Voigt-profile similiar to Moodenbaugh et al. [151] Furthermore, in both spectra a linear background was included. Since especially the evaluation of the CuL$_3$ satellite can be expected to be strongly dependent on background substraction, other types of background functions as e.g. cubic polynomial were tested giving no remarkable change in the results. Within the analysis of the CuL$_3$ edge only relative intensities will be evaluated, and hence, no special normalization is required. The spectra at the OK edge, however, were normalized to the spectral weight comparable to Chen et al. [135]. An example of the fitting procedure is depicted in fig. 5.5(b) and 5.5(d).

Four parameters shall be studied regarding their detailed dependence on the azimuthal angle. These are at the CuL$_3$ edge:

- the hole concentration n$_h$ serving as a measure of satellite intensity

- the energy gap between white line and satellite.

The corresponding parameters at the OK edge are:

- the area of the first pre-peak

- the gap between first and second pre-peak.

In section 5.3 it was explained how a value for the hole concentration can be derived in polycrystals from the relative intensities of the CuL_3 white line and satellite. As will be seen in section 5.5, in single crystals the actual hole content has to be derived by dividing the average of n_h over the azimuthal angle ϕ by the scaling factor 1.5 (see also Ariffin et al. [127]). Already within this section, all values for n_h will be divided with 1.5 to prevent missconceptions regarding the doping level of the investigated samples. The area of the first pre-peak in the OK spectra was calculated by substracting all other spectral features - second pre-peak, linear background and additional Voigt-profile modelling the BiO states - and then integrating the spectral weight of the remaining spectrum in an energy window containing the first pre-peak.

The found in-plane polarization dependence is consistent at the CuL_3 and OK edge. The defined parameters in both spectra exhibit the same characteristics under variation of the azimuthal angle as can be seen in fig. 5.6(a). The data in this figure stem from an overdoped La and Pb substituted $Bi_{2-y}Pb_ySr_{2-x}La_xCuO_{6+\delta}$ single crystal with y=0.48, x=0.27 and T_c=19 K. n_h and the area of the first pre-peak compare to each other excellently in their variation over azimuthal angle of measurement. Also the fitted energy gap between white line and satellite varies similiarly to that between first and second pre-peak.

The fitting of the spectra has different weaknesses at the CuL_3 and OK edge. At the CuL_3 edge the spectral features strongly overlapp as is indicated by the shaded areas in fig. 5.5(b) where also the residuals of the fit are maximal. This potentially leads to errors in fitting the satellite position. Thus, the extracted gap magnitude and possibly even n_h may be slightly incorrect. But, n_h is calculated from relative intensities, and hence, not dependent on normalization. This is in contrast to the situation at the OK edge. The calculation of the area of the first pre-peak in the OK spectra is critically dependent on normalization. First and second pre-peak are, however, much better separated in energy. No constraints were given during fitting. Thus, the similarity of the fitting results at the CuL_3 and OK edge despite the differing source of error, is striking. Hence, the found in-plane polarization dependence cannot be attributed to errors in the analysis.

Furthermore, it can be shown that the in-plane polarization dependence is not a remnant of the surface sensitive TEY mode of measurement, but a bulk effect. It shall be emphasized here that the FY measurements which were recorded simultaneously to the TEY data show qualitativly the same results as can be seen in fig. 5.7. There, the analysis at the CuL_3 edge for TEY and FY data on $Bi_2Sr_2CuO_{6+\delta}$ with no cation substitution and T_c=7 K are compared. The FY signal suffers from selfabsorption which leads to a calculation of values for n_h being 30% too high as reported in Studer et al. [152] and also observable in fig. 5.7. Therefore, the TEY data was analyzed and the results were cross-checked on the FY data.

Now, the interplay of the variations in intensity, respectively area, and those of the energy gaps shall be investigated in more detail. Fig. 5.6(a) and 5.7 reveal that the latter modulate diametrically to the first. n_h and the area of the first pre-peak rise when the energy gap between the corresponding excitations diminishes. In chapter 1.2.2 the charge-transfer energy Δ has been defined as the energy required to transfer an electron from the oxygen to the Cu ion. Within the notation of the transitions given in sections

(a)

(b)
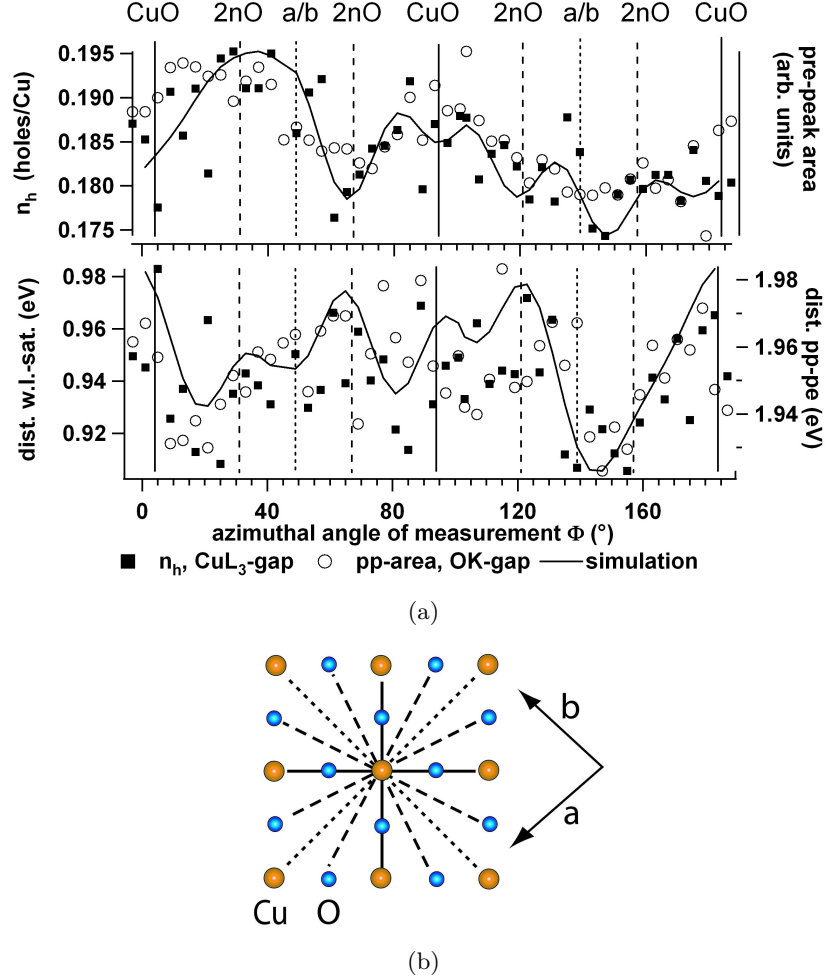
Figure 5.6: **(a)** *Analysis on TEY data of* $Bi_{1.52}Pb_{0.48}Sr_{1.73}La_{0.27}CuO_{6+\delta}$. *$T_c$=19 K. Upper scale:* n_h *(full rectangles) and area of 1st pre-peak (open circles). Lower scale: gap between white line and satellite (full rectangles) and first and fitted second OK pre-peak (open rectangles). Full, broken and dashed lines coincide with the directions as indicated in (b).* **(b)** *Schematic drawing of the CuO_2-plane. Arrows indicate the crystallographic* **a** *and* **b** *axis. The directions of CuO-bonds,* **a/b***, and second next neighbor oxygen are marked with full, dashed and broken lines respectively.*
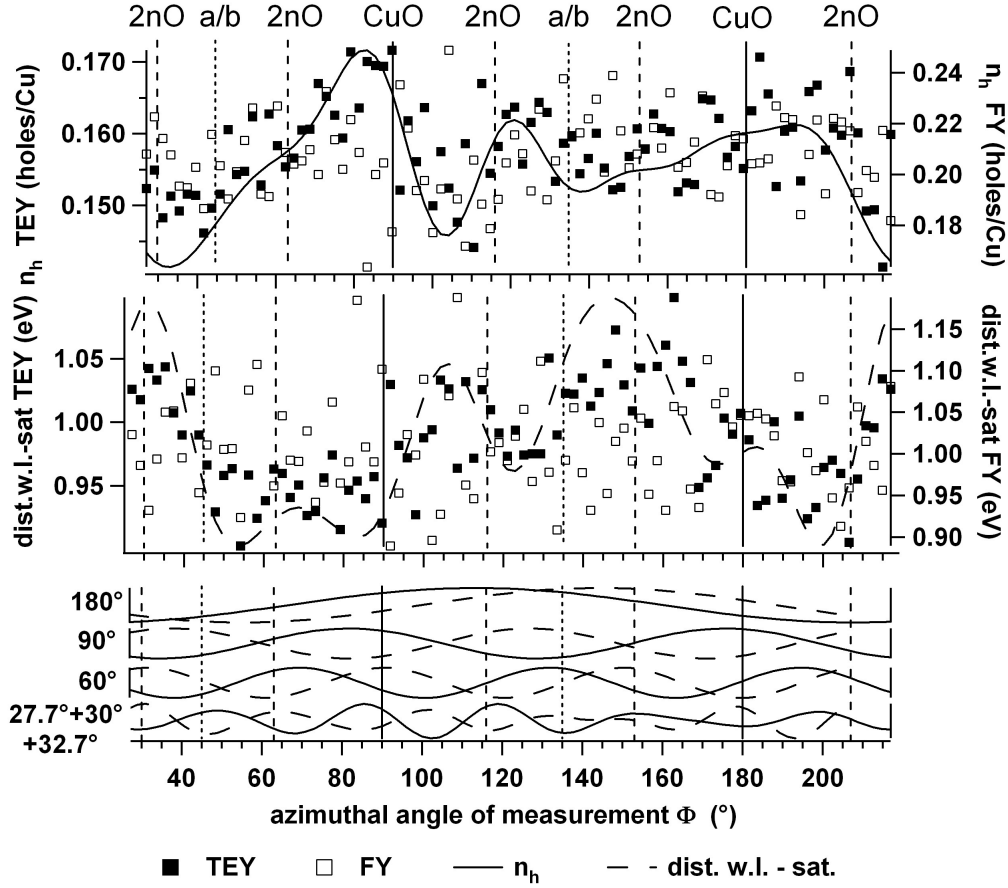
Figure 5.7: *Comparison of TEY and FY data measured at the CuL_3 edge on $Bi_2Sr_2CuO_{6+\delta}$, $T_c=7$ K. Vertical full, broken and dashed lines coincide with the directions as indicated in fig. 5.6(b). Upper scale: n_h. Middle scale: gap between white line and satellite. Full rectangles correspond to TEY, and open rectangles to FY data. The full and broken line show the sum of selected Fourier coefficients as discussed in the text. The individual Fourier components are given on the bottom scale. Full and broken lines refer to the respective functions shown above.*

5.1 and 5.2 this can be written as: $\Delta = E(3d^9 L^{-1} - 3d^{10})$. Thus, the difference in energy of the excitations of the CuL$_3$ white line and satellite, and the first and second OK pre-peak, corresponds to the charge-transfer gap. The measured energy gap, however, gives a renormalized charge-transfer gap because of excitonic effects due to the created core hole and the influence of the hopping integral t$_{pd}$. Weaker excitonic effects at the OK edge lead to less renormalization there. This manifested in our measurements by the gap at the OK edge being twice as large as that at the CuL$_3$ edge. In the same sample, the renormalization by excitonic effects should remain constant and can hardly be imagined to be angle dependent since this are rather local effects. Thus, the variation of the measured energy gaps over angle has to be caused by a varying hopping integral t$_{pd}$ or charge-transfer gap Δ. This is supported in our measurements by the fact that, within one sample, the absolute value of the variation of the energy gap is the same for CuL$_3$ and OK spectra. Since the intensities of the studied spectral features depend on t$_{pd}$ and the charge-transfer gap, changing either or both of the two should lead to variations in intensity, respectively area, as actually observed in our experiment (fig. 5.6(a) and 5.7).

Before elaborating the angular distribution of intensity and energy gap, the question shall be discussed, why this in-plane polarization occurs at all. It was already stated that such an in-plane polarization dependence should not be observable since the unit cell has fourfold symmetry. But, as explained in chapter 2.3 non-stochiometric oxygen and cation dopants cause chemical and electronic inhomogeneities[104]. The impact on electronic and superconducting characteristics depends on the site dopants are located at. La substitution taking place in the SrO layer next to the CuO$_2$ plane is believed to cause strong disturbances by creating lattice distortions and generating a Coulomb potential. Even the hopping matrix element t$_{pd}$ can be changed locally[102].

But also oxygen dopants further away from the CuO$_2$ plane cause disturbances. Furthermore, it was discussed in chapter 2.3 that with little or no La substitution singular Bi atoms tend to populate Sr sites. Since Bi is even more different in size and electronic configuration from Sr than La, also the disturbances caused are stronger. It can be summarized that all samples investigated, whether doping was achieved by La substitution or variation of non-stochiometric oxygen, show inhomogeneities due to dopants. Hence, these inhomogeneities resulting from dopants are a likely candidate for the origin of the

Figure 5.8: *Strength of the modulation of the value for n$_h$ over azimuthal angle. For each sample the difference between maximum and minimum value in percentage to the average value is plotted over the actual hole concentration n$_h$*

here reported dependence on the azimuthal angle. At the local sites of the dopants, the symmetry is broken due to lattice distortions and maybe also by a resulting Coulomb potential These effects may change the transition matrix element. The XAS spectrum

gives a sum of the sites probed by the x-ray beam. Most of these probed sites exhibit the expected symmetric behavior. But, due to sites with dopants closely around, a part of the signal is modulated under azimuthal angle rotation giving the maxima and minima in the analyzed parameters. The strength of the in-plane polarization dependence indeed correlates with the doping level, and hence, number of dopants. It rises with increasing La concentration (decreasing doping) and thus higher number of local disturbances. This is illustrated in fig. 5.8 for the angle variation of the calculated value for n_h. There, the difference of maximum and minimum value of n_h over azimuthal angle in percentage to the average value is plotted over the hole concentration n_h of the respective sample.

Finally, the detailed shape of the studied parameters under variation of the azimuthal angle shall be discussed. The intensity distribution gives information on the orbitals involved in the transition which is in the present case the Cu-O hybrid orbital. Accepting that the symmetry within the plane is broken, the variation of intensity over azimuthal angle in CuL_3 and OK spectra should exhibit maxima along the CuO bonds resembling the expected $d_{x^2-y^2}$ symmetry of the hybridization of the in-plane orbitals $Cu3d_{x^2-y^2}$ and $O2p_{x,y}$. But, the angle dependence of n_h or the area of the first pre-peak shown in fig. 5.6(a) and 5.7 indicates that the angular distribution is much more complex. Within the graphs the crystallographic directions as determined by low energy electron diffraction (LEED) are marked by lines on the axis of the azimuthal angle of measurement Φ. The sketch of the CuO_2 plane in fig. 5.6(b) references the directions in relation to the Cu and oxygen atoms. Two apparent points shall be given a closer look:

1. maxima do not exist along all CuO bonds.

2. maxima occur also along directions of second next neighbor oxygen.

Differences in intensity along orthogonal CuO bond directions have been observed as well by Saini et al.[153] carrying out CuL_3 XAS on single crystals of the double layer Bi cuprate $Bi_2Sr_2CaCu_2O_{8+\delta}$ (Bi2212). Spectra from Saini et al.[153] with the polarization set along orthogonal CuO-bond directions within the plane are shown in fig. 5.9. The calculated values for n_h of the two spectra shown in the figure are 0.18 and 0.28 holes per Cu. In the cited article no statements were made regarding the hole concentration or T_c of the sample. Assuming that the two values give maximum and minimum, the hole concentration according to eq. 5.9 is n_h=0.15. The variation Δh_h=43% is the doubled value compared to the strength of the variation of n_h in a single layer Bi cuprate (Pb,Bi)2201 with n_h=0.15 (fig. 5.8). Saini et al.[153] further collected EXAFS data which allows to determine bond lengths and deduced that within the CuO_2 plane occurs a preferential ordering of tilted CuO_2 units due to a one-dimensional electron-lattice interaction. Taking just the two data points along orthogonal CuO bonds, the detailed angle dependence shown in fig. 5.6(a) and 5.7 could not have been observed.

Above it was stated that besides the asymmetric intensity along CuO bonds also second next neighbor oxygen exhibit local maxima. This leads to the hypothesis that actually the in-plane part of the axial hybrid orbital as proposed by Andersen et al.[58] is observed. This axial hybrid orbital has been introduced in chapter 1.2.2. In fig. 5.10(a) the in-plane part of this axial hybrid orbital is illustrated. The figure clearly shows
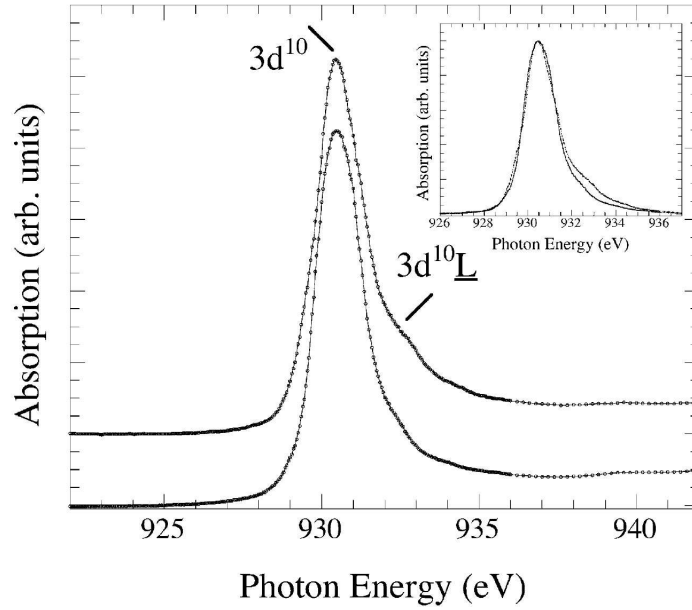
Figure 5.9: *CuL_3 spectra of a double-layer $Bi_2Sr_2CaCu_2O_{8+\delta}$ single crystal taken along two orthogonal CuO-bonds taken from Saini et al.[153]. The inset shows that the satellite differs along the two directions.*

the extra probability distributions in the direction of the second next neighbor oxygens occuring in the axial hybrid orbital. Moreover, fig. 5.10(c) to fig. 5.10(d) show n_h and the energy gap between white line and satellite at the CuL_3 edge for the two samples analyzed in fig. 5.6(a) and fig. 5.7 plotted over the in-plane part of the axial hybrid orbital. These figures again visualize the need of including second next oxygen into the interpretation of the angular distribution of the modulation, and thus, support the hypothesis of observing signatures of the in-plane part of the axial hybrid orbital within the in-plane polarization dependence of the XAS signal. Furthermore, in fig. 5.10(c) to fig. 5.10(d) a simulation of the modulation of the analyzed parameters is included. This simulation will be discussed in the following.

The interpretation of the angular distributions discussed above was further tested by a Fourier analysis. To achieve that the investigated parameters n_h, area of first pre-peak, and corresponding energy gaps as functions of the azimuthal angle ϕ were Fourier transformed. Summing up the Fourier components of 180°, 90°, 60°, 32.7°, 30°, 27.7° symmetry only is sufficient to capture the basic features of the variation of the studied parameters. This is shown by plotting this sum of Fourier components over the analyzed parameters in fig. 5.10(c) to fig. 5.10(d), and also in fig. 5.6(a) and fig. 5.7. The latter figure additionally contains the individual Fourier components all of which differ in their phase and, thus, are not just higher orders. This plot furthermore illustrates that the diametric variation of n_h and the energy gap between white line and satellite can also be found in the respective Fourier components.

(a)

(b)

(c)

(d)

(e)
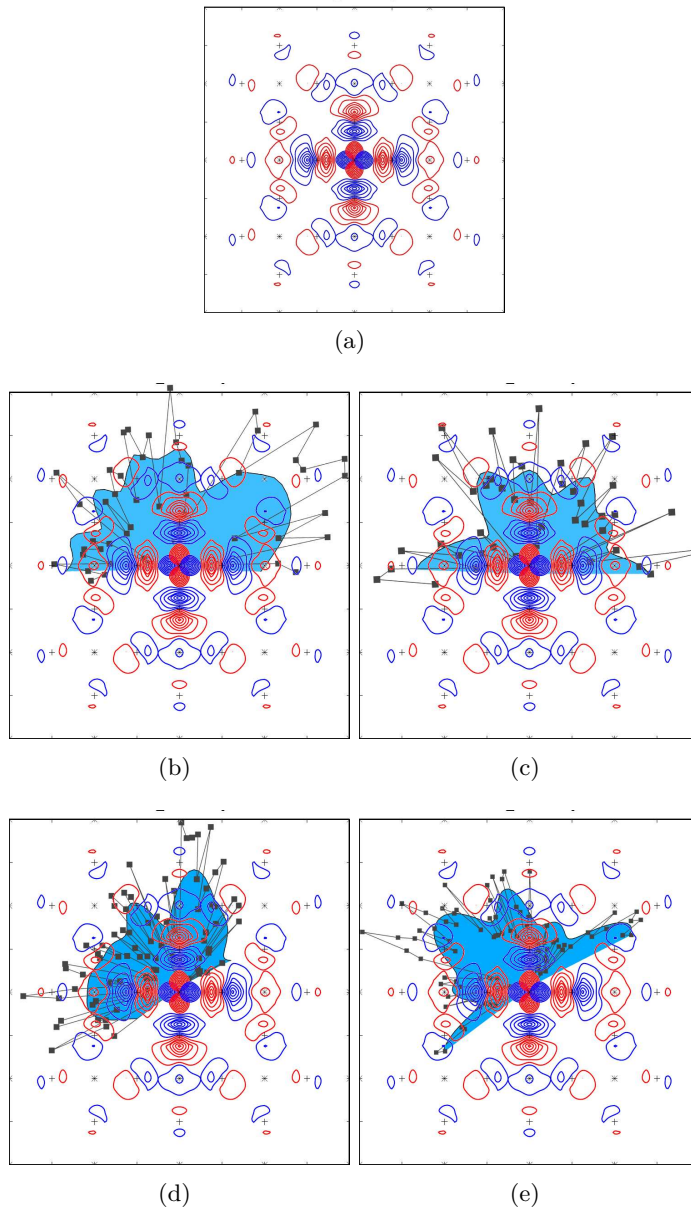
Figure 5.10: **(a)** *In-plane part of the axial orbital as calculated for the single layer La cuprate* La_2CuO_4. *There is extra probability distribution on the second nearest oxygen atoms. Picture taken from Andersen et al.* [154]. **(b)** *and* **(c)** n_h *and energy gap between* CuL_3 *white line and satellite, as well as corresponding sum by Fourier coefficients as discussed in the text for the sample shown in fig. 5.6(a) plotted over the in-plane part of the axial orbital.* **(d)** *and* **(e)** *Same as (b) and (c), but for the sample shown in fig. 5.7.*
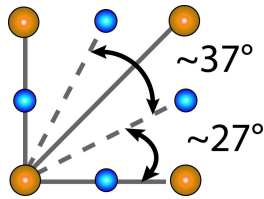
Figure 5.11: *Angles between next and second next neighbor oxygen within the CuO$_2$ plane. Respective of fig. 5.6(b) the solid line gives the a/b and CuO bond direction and dashed lines the second next neighbor oxygen.*

The individual components of the Fourier analysis can be related to crystallographic directions of the sample. The 90° cosine is maximal along CuO-bonds just as expected from hybridized Cu3d$_{x^2-y^2}$ and O2p$_{x,y}$ orbitals. Maybe the most interesting feature is the occurrence of the 27.7°, 30° and 32.7° cosines. The sum of them produces the peaks of the variation of n$_h$ pointing along the second next neighbor oxygen which should not occur assuming d$_{x^2-y^2}$ symmetry. As shown in fig. 5.11, the angles between the next and second next neighbor oxygen atoms are either slightly smaller or larger than 30°. Therefore more than one cosine is needed to account for those discrepancies to the perfect symmetry of the cosine.

Also the discussed 180° periodicity can be found in the Fourier components. The sum of Fourier components with $\sim$ 30° shows minimums and maximums along the CuO bond next neighbor oxygen and the second next neighbor oxygen directions. This behavior is further enforced by the 60° and most of all 180° cosines. The latter two cannot be stringently assigned to a crystallographic direction like the so far discussed cosines. This is probably due to the complex interplay of the individual Fourier components. But, in all samples the 180° periodicity is the lowest one and thus gives orthorhombic symmetry of the whole signal. Since a clear matching of the 180° periodicity to a crystallopgraphic direction is not possible from our measurements, it can only be hypothesized that this periodicity results from structural modulations. A number of superstructures along the **b** direction[97,98,155], which have been discussed in chapter 2.1, have been found in all systems of the Bi-family studied here. They are related to the cation and oxygen dopants in the Bi-cuprates. Besides the variations in the CuO bond distance seen in EXAFS by Saini et al. [153], there are further indications that the dopants cause a tilt in the CuO$_6$-octahedra[2]. These effects are probably interrelated.

Concluding, it can be stated, that the newly found in-plane polarization dependence has been observed in TEY and FY mode, and is consistent in CuL$_3$ and OK spectra. It probably becomes observable due to local disturbances caused by nanoscale inhomogeneities present in Bi cuprates. Intensities of ZRS related spectral features vary with azimuthal angle rotation diametrically to the energy gaps indicating a variation of t$_{pd}$ or the charge-transfer gap Δ itself. Additional to a 180° periodicity, the distribution of intensity over angle moves beyond the expected d$_{x^2-y^2}$ symmetry and shows signatures of the axial hybrid orbital[8,58]. It thus supports the inclusion of out-of-plane orbitals for modelling the electronic structure in the CuO$_2$ plane.

5.4.3 Implications on electronic structure

In the following, the results shall be put in relation to the theory of electronic structure in the CuO$_2$ plane with emphasis on the signatures of the charge-transfer insulator and ZRS states. As introduced in section 5.2, the transfer of spectral weight from first to

second OK pre-peak is characteristic of charge-transfer insulators in which ZRS form the conduction band. Thus, the spectral weight transfer with doping is a strong indication for the interpretation of the first and second pre-peak being related to ZRS and UHB respectively. Peets et al.[145] questioned the stability of ZRS in the overdoped regime on account of their XAS measurements at the OK edge which were already shortly mentioned in section 5.3. They observed the first pre-peak saturating and the second pre-peak becoming weak or absent in overdoped samples (see fig. 5.3(a)). This deviation from the transfer of spectral weight can be interpreted as the breakdown of the stability of ZRS in the overdoped regime. In section 1.2.2 of the introductory chapter the description of the electronic structure of the CuO_2 plane within the three-band model (eq. (1.1)) has been discussed, and the O2p on-site repulsion U_p has been defined. Peets et al.[145] argue that with rising concentration of doped holes, which reside at the oxygen, the impact of U_p on the electronic structure will increase. This in turn will lead to decreasing Cu-O covalency and a rising charge-transfer gap. The weaker covalency may prevent the observation of the strong-correlation-physics, specifily the spectral weight transfer, at the OK edge. Furthermore, the single-band Hubbard and t-J-model approaches within which the ZRS physics is described would breakdown because these models rely on the strong covalency as has also been discussed in section 1.2.2.

Schneider et al.[144] found the same saturation of the first pre-peak in overdoped (Bi,Pb)2201, the cuprate system under study whithin the present work. Schneider et al.[144], however, could identify the second pre-peak by fitting also in the overdoped regime[156]. This is as well the case in our measurements. The second pre-peak resulted from fitting, and in the same sample it mimicked the inverted angle dependence of the first pre-peak just as expected in the charge-transfer picture. For the overdoped sample which was analyzed in fig. 5.6(a), the area of the first pre-peak is compared to the intensity of the second pre-peak in fig. 5.12. Even in this overdoped sample the UHB related second pre-peak diminishes when the ZRS related first pre-peak grows. This means the interplay of first and second pre-peak holds also for the spectra varied by the in-plane polarization dependence.

Now, the transfer of spectral weight shall be compared between differently doped samples. Fig. 5.13(a) gives the mean first and second pre-peak calculated by averageing the parameters as acquired from the fit. These curves were normalized in energy and intensity to the first pre-peak for better visibility. Plotted are only the $Bi_{2-y}Pb_ySr_{2-x}La_xCuO_{6+\delta}$ samples with La and Pb substitution. The investigated samples with only La substitution as well as those with no cation substitution show their own systemacy. The La and Pb substituted system was chosen because most samples were measured of this series. It can be seen that with rising doping concentration the second pre-peak diminishes compared to the first pre-peak. In fig. 5.13(b) the average value over angle of the area of the first pre-peak was plotted over hole concentration for each sample that was measured at the OK edge. The trend of saturation, that has been found previously[144,145], is visible, although the optimally doped sample breaks out forming a small maximum. Thus, it can be stated that despite the changing rate of spectral weight transfer in the overdoped regime, the interplay between first and second pre-peak holds over different doping concentration as well as over varied azimuthal angles within
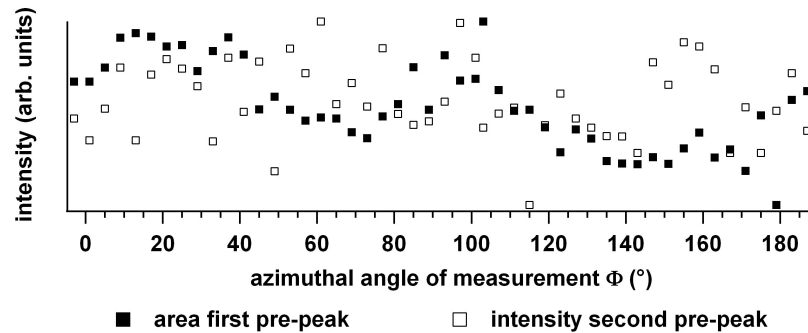
Figure 5.12: *Variation over azimuthal angle of measurement ϕ of area of ZRS related first pre-peak in comparison to the intensity of the UHB related second pre-peak. The scale of the latter is reversed. Shown are data from the overdoped sample of fig. 5.6(a).*

the same sample. Hence, even if the ZRS picture actually fails in the overdoped regime, first and second pre-peak are still correlated.

Within the measurements shown here, it was also found that the energy gap between the CuL_3 white line and satellite, as well as that between the first and second OK pre-peak, rises with higher hole concentration. This is already indicated in the plot of the angular-averaged spectra of fig. 5.13(a). The second pre-peak moves to higher energies with rising hole concentrations. The energy scale was calibrated to the maximum of the first pre-peak, therefore the plot only indicates the rising energy gap but not which peak moves in which direction. Fig. 5.14 gives the fitted energy gaps between CuL_3 satellite and white line and both OK pre-peaks for the samples with La and Pb substitution to further illustrate this point. This does not clearly prove a rising charge-transfer gap since it is not the pure charge-transfer gap that is observed in the spectra as discussed previously. It gives, however, some support to the argumentation of Peets et al.[145] that was laid out in the beginning of this section.

Finally, it shall be noted that Peets et al.[145] suggest that the first OK pre-peak saturates because of a decrease in covalency and subsequent masking of strong correlations from the OK edge. The strong correlations are, however, still visible at the CuL_3 edge. This may explain why the hole concentration can be determined at the CuL_3 edge also in the overdoped regime as has been shown by Ariffin et al.[127] on single layer Bi cuprates which will be discussed in the next section. Therefore, in a sense the ability to apply the method of hole content determination by CuL_3 XAS is also supporting the argumentation of Peets et al.[145] This may also be the case for the observation of the in-plane polarization dependence investigated in the previous section. The angular distribution of this polarization dependence was shown to go beyond the commonly assumed $d_{x^2-y^2}$ symmetry. The strict ZRS model, however, needs that $d_{x^2-y^2}$ symmetry. Therefore, it has previously been questioned by theorists[157] and other singlet states as e.g. plaquette states have been proposed[41,158,159]. To what extend the found in-plane polarization dependence follows in this vein and questions ZRS cannot be answered within this work.
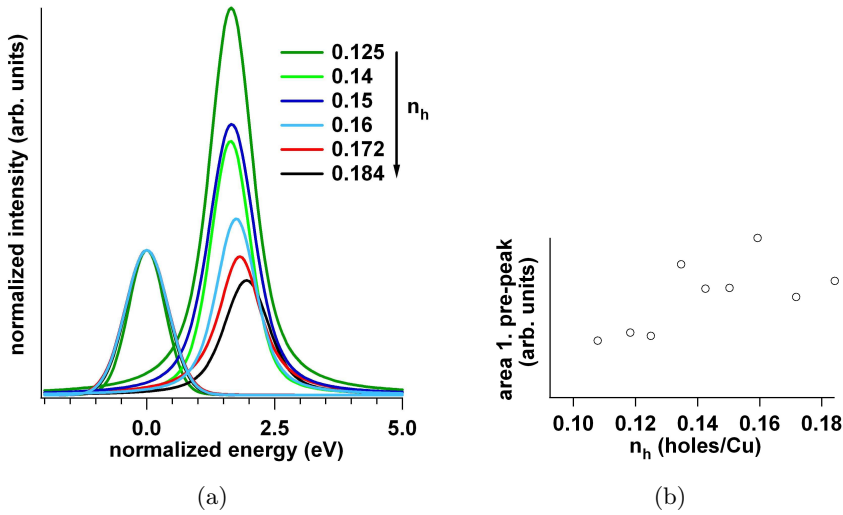
Figure 5.13: **(a)** *Illustration of spectral weight transfer for differently doped* $Bi_{2-y}Pb_ySr_{2-x}La_xCuO_{6+\delta}$ *samples with varied La substitution and a Pb level of about y=0.4. The legend indicates the doping levels of the samples. The plot shows the mean first and second pre-peak as obtained when averageing for each sample the parameters acquired from fitting the spectra taken at different azimuthal angles. For the different samples the mean spectra were normalized to the first pre-peak in intensity and energy. The second pre-peak diminishes compared to the first with rising hole concentration. It further moves to higher energies implying a rising charge-transfer gap.* **(b)** *Area of first pre-peak over hole concentration for all samples that were measured at the OK edge. The trend of the saturating intensity in overdoped samples is visble.*

Summarizing, it can be stated that the systematics of the measured samples covering almost the whole superconducting dome could be interpreted within the theory of the charge-transfer model. However, some observations, like the saturation of the area of the first pre-peak in the overdoped regime, the rising charge-transfer gap, and the detailed angular distribution of the in-plane polarization dependence, also support theories questioning the ZRS picture.

5.5 Phase diagram of single and double layer Bi cuprates

The method of hole content determination in polycrystals by CuL$_3$ XAS has been introduced in section 5.3. The hole content determination in single crystals using XAS, and most importantly, the superconducting dome in Pb substituted single layer Bi cuprates has been studied in detail by Ariffin et al.[127]. Now, only the implications of the above discussed polarization effects on the hole content determination in single crystals shall be shortly described. Then, some conclusions that have been derived in close collaboration with A. K. Ariffin regarding the superconducting dome of single layer Bi cuprates will be outlined. The comparison of single- and polycristalline single layer Bi cuprates will

Figure 5.14: *Energy gaps between white line and satellite at the CuL_3 edge (full rectangles) and between first and second pre-peak at the OK edge (open circles) plotted over hole concentration of the respective sample. Included are all (Pb,Bi)2201 samples that were Pb and La substituted.*
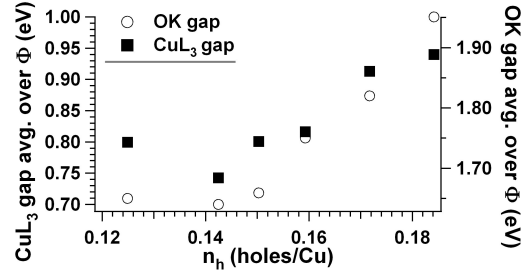
enable to deduce a relation also for single-crystalline double layer Bi cuprates. This will be made plausible on the basis of previous XAS measurements on polycristalline double layer Bi cuprates[156].

Already in section 5.3 it has been stated that eq. (5.8) has been derived disregarding polarization effects. Hence, it is only applicable in polycrystals. It is evident that, when determining the hole concentration from the relative intensity of white line and satellite in single crystals, polarization effects have to be accounted for. Out-of-plane effects as discussed in section 5.4.1 can be incorporated by conducting measurements at a certain angle of incidence, the "magic angle"[160], of $\theta=35°$. The existence of the in-plane polarization, however, makes a measurement at the polar angle $\theta = 35°$ insufficient to account for all polarization effects. To correctly derive the hole content of single crystals by XAS, first the in-plane average of the hole content, $\overline{n}_h$, has to be calculated. This is done by determining the hole content by eq. (5.8) for a representative number of measurements with varied azimuthal angle, and subsequent averaging. Finally, this in-plane average, $\overline{n}_h$, has to be scaled to the measurement on polycrystals. The detailed derivation of this scaling factor, which results to 1.5, can be found in Ariffin et al.[127]. Hence, the hole content, n_h, in single crystals can be calculated by scaling the angular average of n_h by 1.5:

$$n_h = \frac{\overline{n_h}(\phi)}{1.5} \tag{5.9}$$

Using the method described above the superconducting dome of single crystals of the Pb substituted single layer Bi cuprates, (Bi,Pb)2201, was examined[127]. A wide doping range of (Bi,Pb)-2201 single crystals with a lanthanum concentration ranging from x=0.02±0.04 to x=0.7±0.05, and with an approximately constant Pb concentration between y=0.4 and y=0.5 were studied by CuL_3 XAS. From these experiments the curve of T_c versus hole concentration n_h could be derived for La doped single layer Bi cuprates (Pb,Bi)2201:

$$T_c = T_{c,max}[1 - 256(n_h - n_{h,opt})^2] \tag{5.10}$$

This relation is plotted in fig. 5.15 where also the curve derived by Schneider et al.[144] from XAS on polycrystals with and without lead substitution, and the corresponding
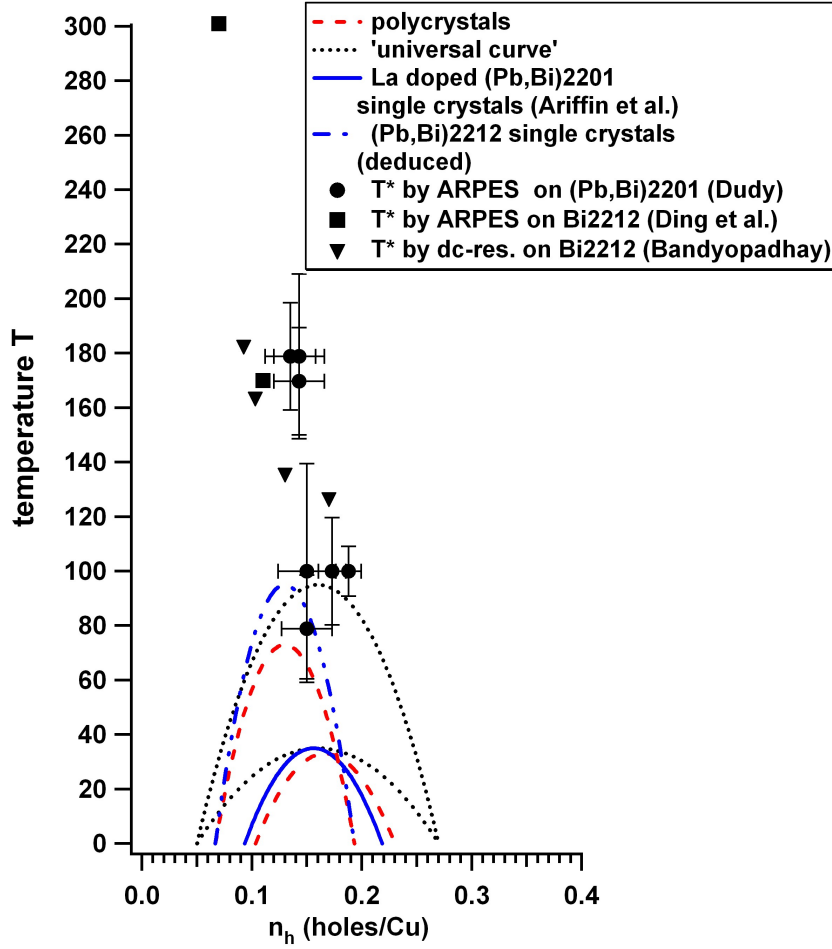
Figure 5.15: *Phase diagram of single and double layer Bi cuprates. The full blue line gives the superconducting transition temperature T_c over hole concentration for La doped (Pb,Bi)2201 single crystals with a Pb substitution level of $\approx$0.45 as derived from XAS measurements[127]. The broken red lines represent the same for Pb substituted and La doped single and double layer Bi cuprate polycrystals[144,156]. The blue dashed-dotted line is deduced as described in the text for Pb substituted double layer Bi cuprate (Pb,Bi)2212 single crystals. The black dotted line illustrates the universal relation of Presland et al.[68] for the single crystals of the single and double layer Bi cuprates. The black markers give experimental data points for the pseudogap temperature T^*. Black full circles were derived by ARPES on La doped single layer Bi cuprates (Pb,Bi)2201 with a Pb substition of 0.4[13]. Black full rectangles were measured also with ARPES, but on the double layer Bi cuprate Bi2212[161]. For the same material T^* as derived from dc-resistivity measurements is represented by black full triangles[162].*

curve of Presland et al.[68] is drawn for comparison. For the latter $T_{c,max}$ was scaled in eq. (1.5) to the maximum T_c value of 35 K in the single layer Bi cuprate single crystals. The superconducting dome of single and polycrystals does not entirely behave as suggested by Presland et al.[68]. It shows a faster drop on the underdoped and over-doped side while having the same value for optimal doping, and is, thus, narrower. This result is in qualitative agreement with previous studies by Ando et al.[137] where the hole concentration was determined by thermopower and Hall measurements and subsequent scaling to the single layer La cuprate $La_{2-x}Sr_xCuO_4$. Reasons for this narrower dome are discussed in detail in Ariffin et al.[127].

Fig. 5.15 also shows the supersonducting dome as derived from XAS measurements for Pb substituted double layer Bi cuprate polycrystals[156] ($Bi_{2-y}Pb_ySr_{2-x}La_xCaCu_2O_{8+\delta}$). The hole content of these crystals was varied by La substitution. Here, the super-conducting dome as given by the relation of Presland et al.[68] is again included in the figure. Also in this case the curve of Presland et al.[68] has been caclulated by scaling $T_{c,max}$ in eq. (1.5). By comparing the curve of single and double layer Bi cuprates, two facts become apparent. First, also the superconducting dome of the polycrystalline La doped double layer Bi cuprates is narrower than the universal[68] curve. This suggests that the effects suppressing superconductivity in the single layer Bi cuprates are also occuring in double layer Bi cuprates. And second, for the double layer Bi cuprate the value of optimum doping lies at lower hole concentrations as that for the single layer Bi cuprate. Specificly, the maximum T_c occurs at $n_{h,opt}$=0.16 in the single layer and at $n_{h,opt}$=0.13 in the double layer Bi cuprates. A lower value for optimal hole concentration of $n_{h,opt}$=0.12 was as well found in previous XAS measurements on polycristalline double layer Bi cuprates[142] ($Bi_2Sr_2CaCu_2O_{8+\delta}$). These polycrystals were not Pb sub-stituted and their hole content was varied by annealing. The same optimal value of $n_{h,opt}$=0.12 for the hole concentration was observed in polycrystalline Y doped double layer Bi cuprates[163] ($Bi_2Sr_2Y_{1-x}Ca_xCu_2O_{8+\delta}$). Within the cited work the hole content has been determined by XAS and coulometric redox analysis. There also a narrower superconducting dome was found on the underdoped side. Similar to the curve given in fig. 5.15 the supercondcting dome started at a hole concentration of n_h=0.06, but the overdoped region was not investigated.

In the next chapter angle resolved photoemission measurements on single crystals of Pb substituted double layer Bi cuprates (Pb,Bi)2212 will be discussed. Hence, from the facts discussed above a curve for the superconducting dome of single crystals of this system was deduced and included in fig. 5.15. It was calculated by using the T_c versus hole content relation of the curve derived from XAS measurements on Pb substituted La doped double layer Bi cuprate polycrystals. Only the maximum T_c was adjustet. This is justified by the observation of similar superconducting domes of polycrystals and single crystals of the Pb substituted single layer Bi cuprate. Furthermore, the cited work on double layer Bi cuprates with different doping methods - varying non-stochiometric oxygen only and substituting Ca by Y - also showed the shifted optimal hole concentration and signs of the narrower dome. As can be seen in the figure, the maximum T_c is much higher in single crystals as in polycrystals of the double layer Bi cuprates. Also for the single layer Bi cuprates the maximum T_c differs between single

and polycrystals. However, this difference is much smaller and, therefore, barely visible in fig. 5.15.

In section 1.2.3 a general phase diagram for the cuprates was given, and the existence of the pseudogap and T* was discussed. In the following, the pseudogap temperature T* will be discussed particularly for the Bi cuprates. This will not only complete the discussion of the phase diagram specific to the Bi cuprates, the estimation of T* will also be helpful in the discussion of the ARPES results of the next chapter. In fig. 5.15 some experimental data points for T* were added to the phase diagram of the single and double layer Bi cuprates. For the single layer cuprate, values for T* were included that were derived by ARPES on La doped single layer Bi cuprates (Pb,Bi)2201 with a Pb substitution of 0.4[13]. The hole content has been determined by the La content for which a formula has been derived by comparing the detailed shape and occuring depressions in the superconducting dome to the single layer La cuprate LSCO[13]. The acquired relation was in very good agreement to those derived by XAS measurements on single[127] and polycrystals[144]. The data points for T* in double layer Bi cuprates have been taken from ARPES measurements[161]. Here the hole concentration was not provided in the cited publication. Hence, it was calculated by comparing the T_c of the investigated samples with the curve that was deduced above for Pb substituted double layer Bi cuprate single crystals. Further data points were taken from dc-resistivity measurements where the hole content of the studied samples has been determined from thermoelectric power measurements[162]. It can be stated that the pseudogap temperatures T* for the single and double Bi cuprate lie very close, if they are not the same within error bars.

Finally, a note shall be made regarding the shift of the optimal hole concentration from single to double layer Bi cuprates. Such a behavior has been discussed within the model of electronic inhomogeneity which derives high temperature superconductivity from stripes (sec. 1.3.7). Within this model, it was predicted that the temperature scale of phase coherence varies for different cuprate families, but also for single and multilayer cuprates of the same family. Since the temperature of pairing stays the same for all cuprates, the superconducting dome, that emerges below the two scales, shifts. This results in higher optimal hole concentration values for single layer cuprates than for multilayer cuprates. In this context the phase diagram of the Bi cuprates of fig. 5.15 can be compared to that of fig. 1.12 of the introductory chapter. The superconducting dome of the Bi cuprates obviously shifts into the right direction from single to double layer Bi cuprates. And, above it was also seen that the pseudogap temperature T*, which is commonly associated with the pairing scale, is similar in single and double layer Bi cuprates. Hence, the prediction of the model of electronic inhomogeneity seem to be fulfilled in the Bi cuprates.

6

The sharp peak in ARPES of (Pb,Bi)2212

In the high T_c cuprates the excitations investigated by photoemission close to the Fermi surface in the antinodal direction are known to be incoherent. Only at low temperatures the so-called sharp peak emerges. The sharp peak was investigated mainly in double layer Bi cuprates, and was interpreted as a coherence peak marking, e.g. a dimensional crossover[164], the onset of quasiparticle like excitations[165], or the signature of superfluid density[89,166]. But, it was also seen as a drastic change in lineshape due to coupling to a bosonic mode[10,90]. Compared to single layer cuprates, in double layer Bi cuprates the lineshape is additionally complicated by interlayer effects between the two adjacent CuO_2 planes which cause bilayer splitting. Hence, especially in the overdoped region the sharp peak was also accounted for by the antibonding band[167] resulting from this bilayer splitting.

Polarization dependent ARPES experiments on the single layer Bi cuprate (Pb,Bi)2201 revealed that the excitations in the antinodal direction close to the Fermi surface are split into a sharp and a broader emission. The sharp emission showed an unexpected polarization dependence. Also the observed temperature dependence of this sharp emission deviated to that observed of the sharp peak in double layer Bi cuprates[11,12,89,168,169]. These characteristics question the interpretation of the sharp peak also in double layer cuprates.

Within this chapter the features close to the Fermi suface in the antinodal direction shall be investigated also on the example of the double layer Bi cuprate (Bi,Pb)2212. But, contrary to the previous investigations mentioned above, within the presented work it will be distinguished between the two bilayer split bands, by exploiting photon energy dependencies of the matrix element of bonding and antibonding band. Strong evidence will be presented for the sharp peak being made up of the antibonding band and an additional excitation which may be connected to this same band. Furthermore, it will be shown that the additional peak found within this work in double layer cuprates (Pb,Bi)2212 and the sharp emission observed in the single layer Bi cuprate (Pb,Bi)2201 exhibit a similar temperature dependence. It will be discussed that the emergence of the additional excitation in double layer Bi cuprates and the sharp peak in single layer

Bi cuprates and their characteristics can be best explained within quasi-one-dimensional models of cuprates.

The chapter is organized as follows. First general considerations regarding polarization dependencies of the photoemission matrix element in cuprates are given. Then, the polarization dependent experiments on the single layer Bi cuprate (Pb,Bi)2201 are introduced. Afterwards the experiments on the double layer Bi cuprate (Pb,Bi)2212 which were conducted within this work are presented. Here, first the bilayer splitting and the different photon energy dependence of bonding and antibonding band are introduced. Then, the dispersion and temperature dependence of the additional excitation are investigated. Finally, the results and possible interpretations will be discussed also in the context of previous work.

6.1 Polarization in ARPES of cuprates

For interpreting and discussing polarization effects in ARPES the equation for the photoemission process (eq. 3.2) has to be considered. similar to the reasoning of section 5.4, for a non-zero matrix element the combination of initial and final state, and the dipole operator has to yield even symmetry. For illustration, polarization settings for the $Cu3d_{x^2-y^2}$ orbital are shown in fig. 6.1. In the figure the **E** vector of the incident light lies within the mirror plane, giving an even dipole operator. The initial state, the $Cu3d_{x^2-y^2}$ orbital, is odd with respect to the mirror plane since lobes with opposite polarity are reflected onto each other. The final state in photoemission can be simplified as being a plane wave with even symmetry. Hence, electron emission within the shown mirror plane is not allowed. In other words: when the light is polarized along the crystallographic **b** axis, which is the ΓY direction in reciprocal space (see chapter 2.2), electrons detected along this same direction will have low intensity. In the opposing case of polarization within the crystallographic **a**, or in reciprocal space ΓX direction, the dipole operator would have odd symmetry and, thus, the whole matrix element would change to even symmetry. With polarization along ΓX, electron emission along ΓY has high intensity.

Now, another case which is variant in the course of this chapter shall be discussed. If the mirror plane is set along the CuO-bonds (along the lobes), which is the ΓM direction in reciprocal space, the initial state would be even. The final state is still even. Thus, polarization within the measured ΓM direction should give high intensity, while polarization along the perpendicular ΓM direction has low intensity. However, if the polarization is turned 45° out of the mirror plane along the ΓY direction, the dipole operator has an odd and an even part. The same case arises when turning the polarization vector into the ΓX direction. There should be no difference between both settings from symmetry considerations.
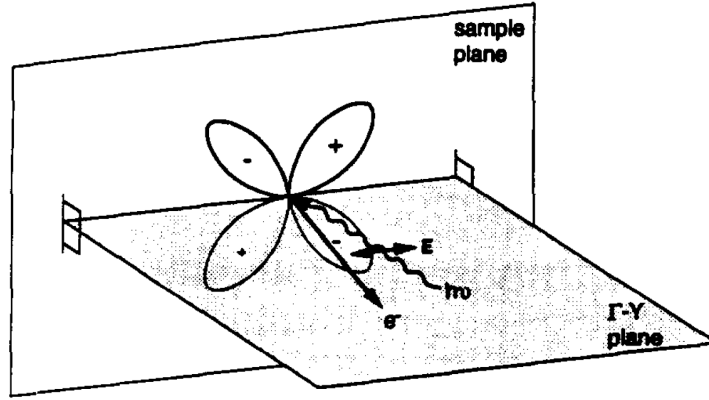
Figure 6.1: *Polarization setting for the $Cu3d_{x^2-y^2}$ orbital with the mirror plane of incoming light and detected electrons within the ΓY direction. The **E** vector of the light lies within this mirror plane in this example. Conclusions regarding the emission can be found in the text. Figure taken from Shen and Dessau*[170].

6.2 Split excitations in single layer Bi cuprates

In the following measurements on the single layer Bi cuprate Bi2201 will be shown which are contradictory to the above made considerations. Polarization dependent measurements revealed a polarization dependence of the emission close to the Fermi surface along the ΓM direction. The emission changed upon switching the polarization vector from the ΓX to the ΓY direction. Such a polarization dependence, however, was excluded above. These measurements are motivation for the experiments on the double layer Bi cuprate (Pb,Bi)2212 presented within this chapter and shall, therefore, be discussed in more detail now.

The polarization dependent experiments for the first time reported by Manzke et al.[168] were carried out at BESSY I at the U2/FSGM, crossed monochromator/undulator combination, which allows the rotation of the polarization of the synchrotron light by $90°$[172]. For photoelectron detection and analyzation a two-axis goniometer was used. The overall energy resolution was 30 meV and the angle resolution $1°$. Fig. 6.2(a) shows the polarization dependent spectra at the M point of an optimally doped Bi2201 sample. It is evident from the figure that the emission at the M point consists of two features. A broader one at higher binding energy and a sharp emission at low binding energy. The latter seems to be switched on and off when changing the polarization geometry by turning the **E** vector from ΓY to ΓX.

Further studies[11,12,169] revealed that the low binding energy emission is present at different doping concentrations and in samples with and without lead substitution. The sharp emission close to the Fermi energy can be switched on and off not only by distinct polarization geometries, but also with changing temperature as illustrated in fig. 6.2(b). The figure shows temperature dependent spectra of a weakly overdoped (Pb,Bi)2201 sample measured at the 4m-NIM at SRC with an energy resolution of 16 meV and an

(a)

(b)

(c)
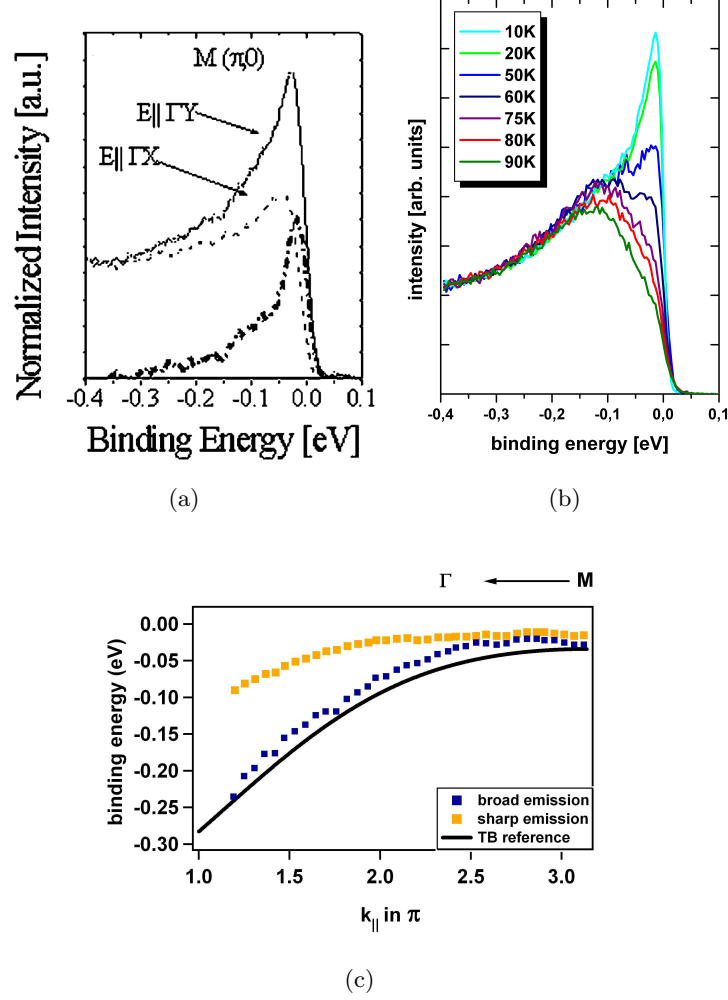
Figure 6.2: *Characteristics of the sharp emission at low binding energies in the vicinity of the Fermi energy of $(Pb,Bi)_2Sr_{2-x}La_xCuO_{6+\delta}$.* **(a)** *Polarization: Spectra at the M point of a sample with no lead, x=0.4, T_c=29 K. The measurement was taken in the normal state at T=35 K and hν=34 eV. Direction of the **E** vector for the two different polarization geometries are indicated. The bold dotted curve shows the difference spectrum. Figure taken from Manzke et al.[11].* **(b)** *Temperature dependence: Spectra at 0.75 ΓM of a sample with lead substitution, x=0.15, and T_c=25K. Measurement taken at hν=22 eV with polarization set along measured ΓM direction. The additional structure is present at 10 K and vanishes at temperatures between 60 K and 75 K.* **(c)** *Dispersion of broad and sharp emission along ΓM of sample from (a). Spectra taken at T=45 K and hν=22 eV with polarization along the measured ΓM direction. Data were published in Janowitz et al.[12]. Additionally included is the dispersion of the main band as expected from a tight-binding fit[171].*

angle resolution of 0.18°. The low binding energy emission is present in the super-conducting state, but vanishes at much higher temperatures than T_c. The observed dispersion of both emissions along ΓM is shown in fig. 6.2(c). Included is the expected dispersion of the bands as retrieved from a tight-binding fit[171]. The two emissions close to the Fermi surface are separated approximately 16 meV at the M point. Towards the Γ point they move away from each other. The broader feature follows the tight-binding fit. It can be ruled out that the sharp emission close to the Fermi surface is caused by diffraction replica stemming from the ≈(5x1) superstructure since the sharp emission has also been observed with similar characteristics, especially dispersion, in lead substituted samples without this ≈(5x1) superstructure[11].

6.3 The sharp peak in double layer Bi cuprates
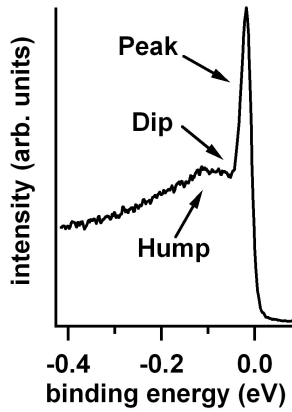

Figure 6.3: *ARPES spectrum at the M point of an optimally doped Bi2212 sample (T_c=92 K) at hν=22 eV and T= 20 K. Close to the Fermi surface there is the so-called sharp peak, followed by the dip and hump.*

The existence of these two emissions along ΓM and their characteristics shall be investigated in the double layer Bi cuprate (Pb,Bi)2212 within this chapter. The ΓM direction is especially interesting since the d-wave superconducting gap is maximal along this direction, and hence this region in the Brillouin zone is believed to be connected to the superconducting mechanism. Along the ΓX/Y direction the superconducting gap has a node. Therefore the ΓM direction is also called the antinodal direction in opposition to the nodal ΓX/Y direction. The latter terms will also be used in the following for the respective directions.

The lineshape in double layer Bi cuprates, however, is more complex than in single layer cuprates. In the antinodal direction close to the Fermi surface a peak-dip-hump (PDH) lineshape is found that is illustrated in fig. 6.3. After observing this structure, the question was - and partly is still today - whether this PDH is the intrinsic lineshape or the signature of two separate bilayer split excitations. The two CuO_2 planes within one unit cell are only seperated by a Ca layer (see also chapter 2.1). Hence, the adjacent layers are not sufficiently decoupled as in the single-layer material, and interactions between the planes are expected to lead to a splitting of the CuO-derived band into bonding and antibonding excitations. According to LDA[58] and calculations based on the Hubbard model[173,174] this splitting is maximal along the antinodal or ΓM direction. Although predicted by theory, the bilayer splitting in double layer cuprates could at first not be experimentally resolved[171,175]. Later, with higher resolution and possibly also better sample quality, the PDH lineshape was found to represent the bilayer split-
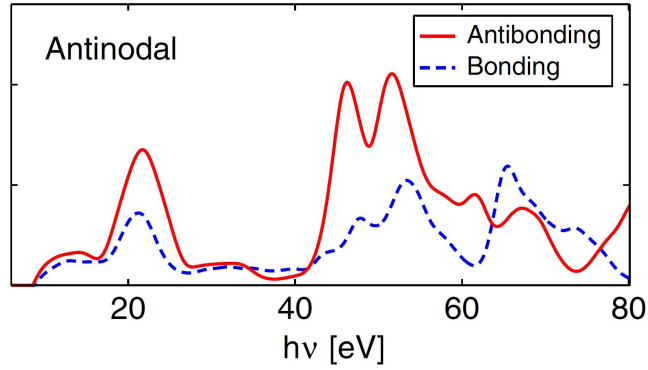
Figure 6.4: *ARPES intensity from the bonding (blue dashed lines) and antibonding (red solid lines) band along the antinodal direction of Bi2212 in dependence on photon energy as derived by one-step calculations. Figure taken from Bansil et al.* [183].

ting in overdoped cuprates [167,176,177], and soon after also in optimally and underdoped cuprates [178–181]. The PDH lineshape could be identified with the bilayer splitting because of a different polarization dependence of the two emissions [177], comparison with the lineshape of single layer Bi cuprates where no bilayer splitting exists [176–178], and most of all the strong photon energy dependence of the PDH lineshape [167,176,177]. The differing dependence on photon energy of bonding and antibonding band was also calculated using one-step calculations based on LDA derived band structures [182,183]. The photon energy dependence varies for different k points in the Brillouin zone. As shown in fig. 6.4, along the ΓM direction the antibonding band is especially strong at photon energies around 50 eV, where, additionally, the bonding band is rather weak.

To clarify the occurence of an additional excitation in the vicinity of the Fermi energy, the strongly differing photon energy dependence of the bonding and antibonding band were exploited in the present work. Thus, in the double layer cuprate (Pb,Bi)2212 the bilayer split bands could be distinguished and the complexity of the lineshape be reduced. Measurements were conducted at 50 eV photon energy, and, hence, predominantly the antibonding band was studied regarding a split excitation similar to the findings in the single layer cuprate (Pb,Bi)2201 as discussed in the previous section. The polarization was chosen to be E∥ ΓM and, thus, intermediate between the two extremal settings of E∥ ΓX and E∥ ΓY. This was donedue to the limitations of the experimental setup at BESSY II and SRC where measurements were conducted. Emphasis was put on the analysis of the dispersion and temperature dependence along the antinodal direction and especially the M point. The same polarization settings have also been used for the study of dispersion and temperature dependence of the two emissions in the single layer Bi cuprate (Pb,Bi)2201 introduced in the previous section.

Experiments with varying photon energy were conducted at BESSY II at the PGM2 beamline using the MUSTANG chamber equipped with a SPECS Phoibos electron analyzer. The angular resolution was 0.2°, the energy resolution at low photon energies ΔE=13 meV. The entrance slit of the analyzer was parallel to the polarization of the

synchrotron light and therefore also parallel to the measured ΓM direction.

The high quality optimally doped and lightly overdoped Bi(Pb)2212 samples studied were grown employing a self flux technique. The samples were characterized by EDX, AC-susceptibility and LEED as described in chapter 2.4 and 2.5. The EDX measurements showed a Pb content of y=0.2-0.3. This is in the range of the optimal suppression of the $\approx$(5x1) superstructure which could be confirmed in LEED measurements that showed the sharp spots of a pseudo-tetragonal cell. The superconducting transition temperature as derived from AC-susceptibility was T_c=95 K for the optimally doped and T_c=85 K for the overdoped sample. The transition width was ΔT_c^{opt}=5 K and ΔT_c^{od}=5 K for the optimally and overdoped sample, respectively.

In a first step the ΓM direction was measured at different photon energies in order to validate the expected photon energy dependence of bonding and antibonding band. And indeed, the photon energy dependent measurements showed a strong variation of the matrix element of bonding and antibonding band on the photoemission spectra. This can be seen in fig. 6.5 where spectra from the M point of the optimally doped sample are shown with the respective photon energy indicated. At 50 eV photon energy the bonding band is most efficiently supressed, only the antibonding band is visible. For comparison, spectra from Kordyuk et al.[167] taken at the same or similar photon energies on a strongly overdoped (Pb,Bi)2212 sample with T_c=69 K are included in this figure on the left column. The overall development of the spectra with photon energy is the same. This evolution of the matrix element with photon energies is reported to be very similar in underdoped samples[179]. Also for the overdoped sample measured within this work the same effect was visible. Thus, it seems that the photon energy dependence of bonding and antibonding band is relatively independent of hole concentration.

For a more detailed analysis the obtained spectra were fitted using a similar approach as He et al.[166]. In the follwing the derivation of the fitting function is laid out. In chapter 3.3 it has been discussed that ARPES spectra can be interpreted in terms of the one-particle spectral function. Under the assumption that the photoemission process in cuprates can be described within the framework of quasiparticles, this one-particle spectral function was given in eq. (3.10) and resulted to:

$$A(\vec{k}, \omega) = \frac{1}{\pi} \frac{\mid \Sigma''(\vec{k}, \omega) \mid}{[\omega - \epsilon_k - \Sigma'(\vec{k}, \omega)]^2 + [\Sigma''(\vec{k}, \omega)]^2} \tag{6.1}$$

with the self-energy $\Sigma = \Sigma' + i\Sigma''$ and the bare dispersion ϵ_k. The detailed expression of Σ depends on the employed theory. The scope of this work is a mainly phenomenological discussion of the excitations close to the Fermi surface and its characteristics regarding photon energy dependence, dispersion and temperature and not the presentation of an explicit theory. Therefore the spectra were modeled with plain Gaussians in a first step. For comparison with other work[166,167] in a second step a phenomenological fitting function[167] was adopted that starts at eq. (6.1) and simulates Σ'' as $\Sigma'' = \sqrt{(\alpha\omega)^2 + (\beta T)^2}$. This ansatz gave overall better fitting results. Therefore, this model will be discussed in the rest of the paper. But, it shall be emphasized here that the results obtained were essentially the same whether the excitations were simulated with a Gaussian or with the
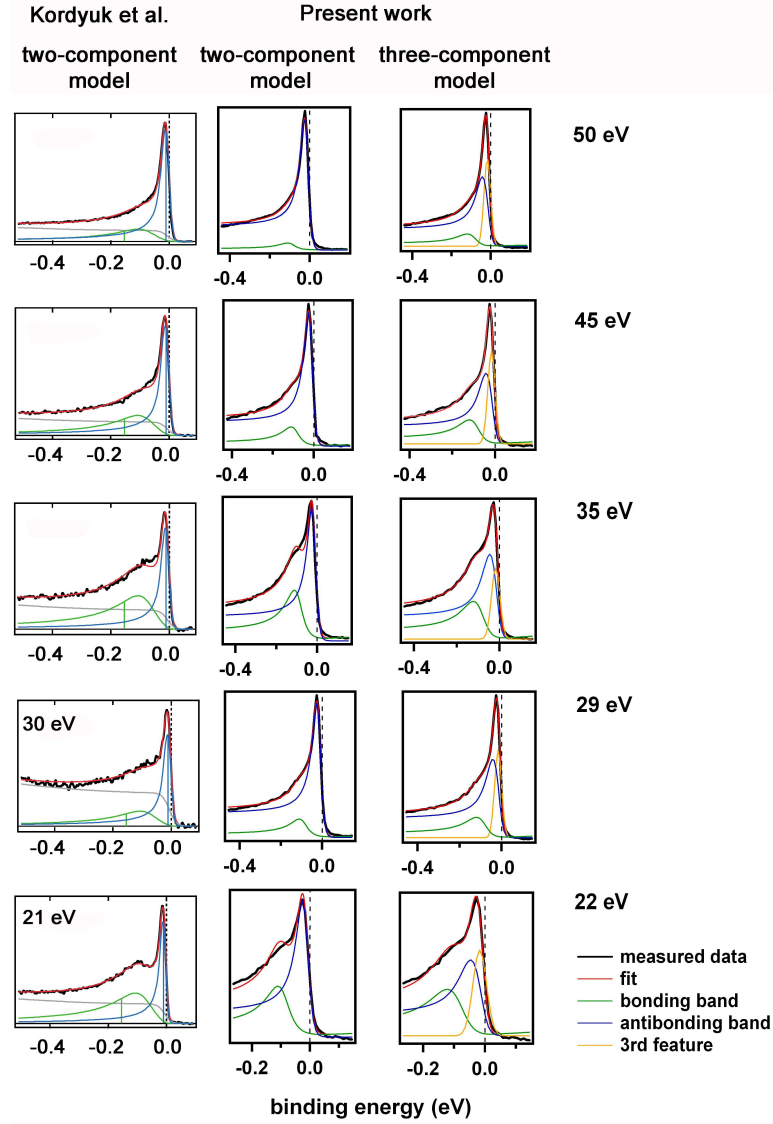
Figure 6.5: *The M point of (Bi,Pb)2212 at different photon energies.* **Left column:** *Figures taken from Kordyuk et al.* [167]. *Shown are spectra of an overdoped sample with T_c=69 K measured at 27 K with two-component fit included.* **Middle column:** *Spectra of optimally doped (Bi,Pb)2212 sample with T_c=95 K measured at 30 K and fitted with two excitations (antibonding and bonding band) using the phenomenological model of Kordyuk et al.* [167]. **Right column:** *Same Spectra as on the left but modeled with three excitations (bonding and antibonding band plus additional excitation) according to formula 6.2. Please note the shorter energy scale in the last row. The measured spectra appear in red, antibonding band in blue, bonding band in green, the additional excitation in orange and the resulting fit in black. The background is given in grey in the left column. In the middle and right column it is already substracted.*

phenomenological[166,167] model. The usage of the latter is within this work not regarded as prove for the existence of quasiparticles. In this context the argument of Kivelson and Fradkin[87] is pointed out. Depending on the parameter also the spectral function of the one-dimensional Luttinger liquid may show Fermi-liquid-like peaks[184], although the elementary excitations do not represent single electrons. Also, the spectra of the single layer (Pb,Bi)2201 cuprate[11,12,168,169] introduced in the beginning of this chapter could be modeled with a spectral function that extended the one-dimensional Luttinger liquid into two dimensions[185].

The ARPES spectra were first fitted with two excitations like a plain band model with bilayer splitting would suggest. But, in order to investigate the antinodal direction of the double layer Bi cuprates regarding the additional excitation a three-component fit was employed afterwards. Also in other work[166,167] on the antinodal excitation in the double layer cuprate (Pb,Bi)2212 a fitting procedure containing three peaks was much more successful. Like practiced by He et al.[166], within this work the additional third peak needed in the fitting procedure was modeled as a Gaussian. However, no spectral weight transfer was included in opposition to the cited work. So eventually the photoemission signal was modeled as:

$$I \propto \{|M_{ab} \cdot A_{ab}| + |M_{bb} \cdot A_{bb}| + |M_c \cdot A_c|\} \times f(\omega, T) \otimes R_\omega + B(\omega, T) \tag{6.2}$$

$$A_{ab,bb} \propto \frac{|\Sigma''(\vec{k}, \omega)|}{[\omega - \epsilon_k - \Sigma'(\vec{k}, \omega)]^2 + [\Sigma''(\vec{k}, \omega)]^2}$$

$$A_c \propto exp\left\{\left[\frac{\omega - \omega_0}{\Gamma}\right]^2\right\}$$

Here f(ω, T) is the Fermi function, R_ω the resolution function modeled as a Gaussian which is convoluted over the signal and B(ω, T) the background. The indices ab and bb correspond to antibonding and bonding band, and the index c to the additional excitation. In fig. 6.5 a comparison between the two-component and three-component fit are shown on the middle and right column. The improvement of the fitting results by using the three-component fit becomes especially clear for measurements at photon energies where the intensity for both, bonding and antibonding band, are not very different. This is also evident within the similar two-component model from Kordyuk et al.[167] on the left column of fig. 6.5. It shall be pointed out here that the ratio of the matrix element of the antibonding band in the two-component case and the combined matrix element of the antibonding band plus the additional peak in the three-component case is approximately one at every photon energy. Thus, the antibonding band and the additional excitation account for the spectral weight of the sharp peak that has been modeled within the two-component fit by the antibonding excitation only. Furthermore, in the three-component fit, the matrix element of the antibonding band and the additional excitation change similarly with photon energy which results in their ratio staying almost constant. This can also be deduced from the photon energy dependence of both excitations in fig. 6.5. Except for the 35 eV spectrum which may be a remnant of

the fitting only, antibonding band and additional excitation rise and decrease in intensity analogously. Hence, the additional excitation may be realated to the antibonding band. However, a connection between antibonding band and additional excitation cannot be rigorously confirmed within this work.

This may hint to the additional peak being a feature of the antibonding band. The additional excitation close to the Fermi surface is separated approximately 15 meV from the antibonding band. This is about the same energy separation as between the sharp emission at low binding energy and the broader emission at higher binding energy in the single layer material. There the broader emission also followed the expected main band dispersion.

To study this additional excitation in more detail, and further compare it with the one found in the single layer Bi cuprate (Pb,Bi)2201, in the following sections first the dispersion and then the temperature dependence of the excitations close to the Fermi surface along the antinodal direction will be examined. In the course of this investigation the comparison to other work will always be drawn. Interpretation and discussion of the results will follow in the last section.

6.3.1 Dispersions

As stated before, especially the ARPES spectra taken at 50 eV were studied since there predominantly the antibonding band is measured. However, as can also be seen in fig. 6.5, the fitting procedure still retrieves the remnants of the bonding band. This holds for the entire measured range along the ΓM direction. Hence, the dispersion as derived
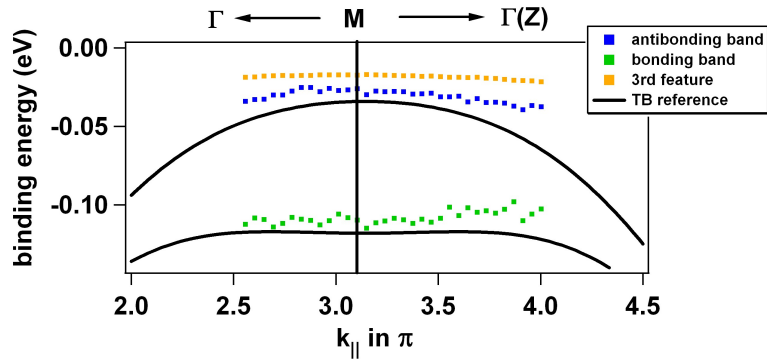
Figure 6.6: *Dispersion of the three excitations from 0.8 ΓM to 1.3 ΓM as derived from the fit. Antibonding and bonding band: blue and green squares respectively, additional excitation: orange squares. Included for comparison is the tight-binding fit from Norman et al.[171] with black solid lines.*

from the fit of all three, bonding, antibonding and additional excitation, can be plotted. This is done the entire measured region of ΓM at 50 eV photon energy in fig. 6.6. The dispersion of bonding and antibonding band are compared with a tight-binding fit, of an optimally doped Bi2122 sample from Norman et al.[171]. Basically, eq. 1.4 was employed using the parameter of Norman et al.[171]. Additionally, the dispersion for the bonding

band was modeled according to Liechtenstein et al.[173] with:

$$\Delta_{bs} = \frac{t_\perp (cosk_x - cosk_y)^2}{2} \tag{6.3}$$

where Δ_{bs} gives the energy splitting between antibonding and bonding band. Thus, the whole dispersion relation becomes:

$$\epsilon(\boldsymbol{k}) = -2t(cosk_x + cosk_y) + 4t'cosk_xcosk_y$$
$$-2t''(cos2k_x + cos2k_y) \pm t_\perp (cosk_x - cosk_y)^2/4 \tag{6.4}$$

In the measurements $t_\perp$ resulted to 44 meV which is a realistic value for the band splitting and similar to other work[176]. Hence, it can be stated that the analysis using the three-component fit yields physically sound results that are comparable to previous work from other groups.

Lastly, the observed dispersion shall be compared to other work[166,176] in which in was also argued that, at low temperatures, there exist more features in the antinodal direction close to the Fermi surface than bonding and antibonding band only. The observations made on an overdoped double layer Bi2212 sample with $T_c = 65$ K and no lead substitution is displayed in fig. 6.7. The shown dispersion was obtained from measurements with an unpolarized HeI VUV lamp. They, however, also observed these features using polarized synchrotron light. In either case, the polarization dependent feature found in the single layer Bi cuprate (Pb,Bi)2201[11,12,168,169] would be expected to be observable within the setup of Feng et al.[176] and He et al.[166]. At the synchrotron the polarization settings were similar to the experiments conducted within the present work, and unpolarized light should, of course, also show the polarization dependent feature, although maybe altered in intensity.

Fig. 6.7(a) shows the dispersion along ΓM of the components of the aforementioned PDH structure developing at low temperature as found by[166,176]. While the hump follows the expected bonding band dispersion the peak cannot be attributed to the antibonding band since the bilayer splitting decreases towards Γ, but, the observed peak moves away from the hump. This figure is shown here to illustrate that the dispersion observed of the peak in the cited publications is very similar to that of the additional excitation found in the double layer Bi cuprate within the present work, and also to that of the sharp emission found in single layer Bi cuprates[11,12,168,169]. Fig. 6.7(b) shows measurements on a similar sample as shown in fig. 6.7(a). Here, however, the measurement was conducted along the X-Y direction crossing the M point. It is to note that around the M point three excitations were found in the superconducting state. The two excitations close to the Fermi surface are separated by 20 meV, which is close to the separation of 15 meV of the additional excitation and the antibonding band studied in the present work. Within the cited publications, the two excitations close to the Fermi surface were assigned antibonding and bonding peak, while the excitation at higher binding energy was termed bonding hump (fig. 6.7(b)). The latter was observable at the same energy in the normal and superconducting state.
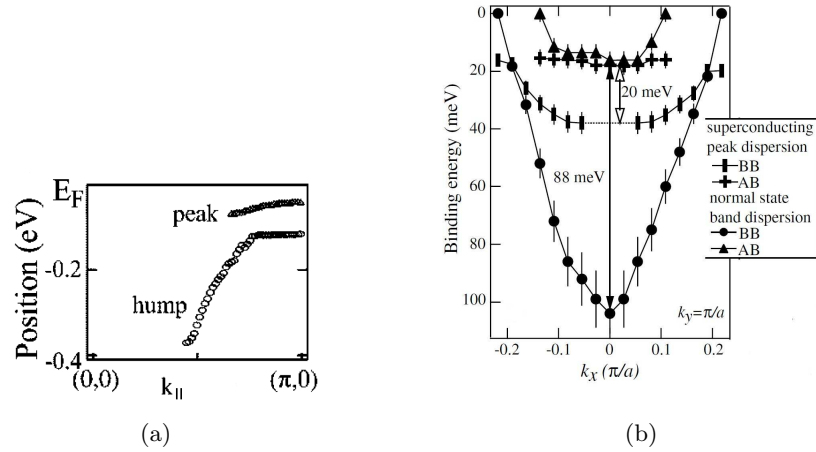
Figure 6.7: **(a)** *Dispersion of the peak and hump of a strongly overdoped sample T_c=65 K measured at T=29 K with 22.4 eV photon energy as observed by He et al.[166] where the figure is taken from. While the hump disperses as expected from the bonding band, the peak cannot be attributed to the antibonding band since this would give a rising bilayer splitting contradictory to theory.* **(b)** *Dispersion of observed excitations around the M point along X-Y on a similar sample as in (a). Measurement was conducted using He-Iα light at T=10K (superconducting state) and T=90K (normal state). At low temperatures three features are observed.*

6.3.2 Temperature dependence

Now, the temperature dependence of the spectra at the M point shall be analyzed. The temperature dependence of the features close to the Fermi surface is very important since it can to some degree distinguish between different models for high temperature superconductivity as will be discussed later. As mentioned in the last section, the antinodal region is believed to be intimately connected to superconductivity in the cuprates. Therefore, the temperature evolution of features in the antinodal direction are of special interest, and has, hence, gained a lot of attention also in the past.

Because of the temperature broadening of the spectra, an analysis of the temperature dependence of antibonding and additional excitation by fitting is, although achievable, not as useful and convincing like the analysis by fitting shown in the last section. Therefore, the procedure of peak extraction as used in other work[89] will be employed. Within this procedure the temperature dependence of spectra at the M point of an optimally doped double layer cuprate (Pb,Bi)2212 taken at 50 eV at the SRC will be compared to the temperature evolution of the single layer cuprate (Pb,Bi)2201 shown and discussed in section 6.2.

Feng et al.[89] proposed to extract the peak close to the Fermi surface at the M point in double layer Bi2212 either by a linear or Shirley background[186] type substraction or by fitting the spectra. The latter shall be done with a phenomenological function which is the product of a Fermi function with a parabolic function. Feng et al.[89] claim the fit to be very robust. Within this work, however, it was found that probably due to

the Fermi function a variety of parameters can be used for the parabolic function since the Fermi function reliably cuts it off. Thus, almost arbitrarily, a peak-like structure can be created with the parabolic function. Hence, within this work the linear and Shirley type substraction was used. It shall be noted that here just the algorithm is used to cut off a peak, but not to model a realistic background of the spectrum. After extracting the peak, Feng et al.[89] calculate what they termed the superconducting peak ratio (SPR) which they defined as ratio of peak area to area of full spectrum. They used an integration window of 500 meV to calculate the areas which will be adopted within this work for sake of comparability.

The temperature dependent measurements were conducted at the PGM beamline at the SRC with a Scienta SES2002 analyzer. The energy resolution was 21 meV at 50 eV photon energy and the angular resolution was 0.18°. Temperature dependent data of an optimally doped (Pb,Bi)2212 sample with a lead concentration of y=0.24 and T_c=91 K synthesized and characterized as described in chapter 2.4 and 2.5 is shown in fig. 6.8(a). The photon energy was 50 eV so that, as discussed above and shown with the measurements in BESSY, predominantly the antibonding band was probed. From fig. 6.8(a) it is evident that a very sharp peak structure exists at low temperatures that broadens and loses spectral weight with rising temperature. However, a peak like structure persists above the superconducting transition temperature - even at temperatures rather high above T_c. This is in opposition to the peak- and featureless spectra observed in other work at high temperatures. Fig. 6.8(a) also shows the extraction of the peak by the linear and Shirley background type method. The determination of the peak onset is not without ambiguity. At low temperatures the peak is so intensive that the rest of the spectrum has a plateau-shape. But, at high temperatures this spectral shape is lost. To solve this problem in a consequent manner, the higher binding energy point was set in the 20 K spectrum where the onset of the peak is clearly observable. This energy point was used for all temperatures. To account for temperature broadening the lower binding energy side at the Fermi energy was adjusted. But, thus, only a lower bound for the peak area can be given.

The result of this temperature analysis is given in fig. 6.9(a) where the ratio of the sharp peak and the widths of the extracted peak are plotted in dependence of temperature. First of all, it is to note that although the peak extracted by the Shirley method has approximately the same width as the linearly extracted one, the peak ratio determined by the Shirley method is higher. Therefore, error bars of ± 1.5% were added. This is the error estimated by Feng et al.[89] from the different methods of peak extraction. The points of the sample analyzed here do not all lie within each others error bars, but, the error bars itself do overlapp in all cases. Hence, the error should be set higher to ± 2.5%. However, even when assuming a higher error, the peak ratio for this optimally doped sample seems to be around 12% at 20 K. It decreases to approximately 8% around the superconducting transition temperature T_c. Above T_c its intensity seems to enter a plateau until at 200 K it has decreased to 4%. Since there were no temperature measurements made between 150 K and 200 K it cannot be said, when and how this marked change from the plateau above T_c to the almost total disappearance of the additional excitation at 200 K occurs. However, a look at the phase diagram of the Bi cuprates
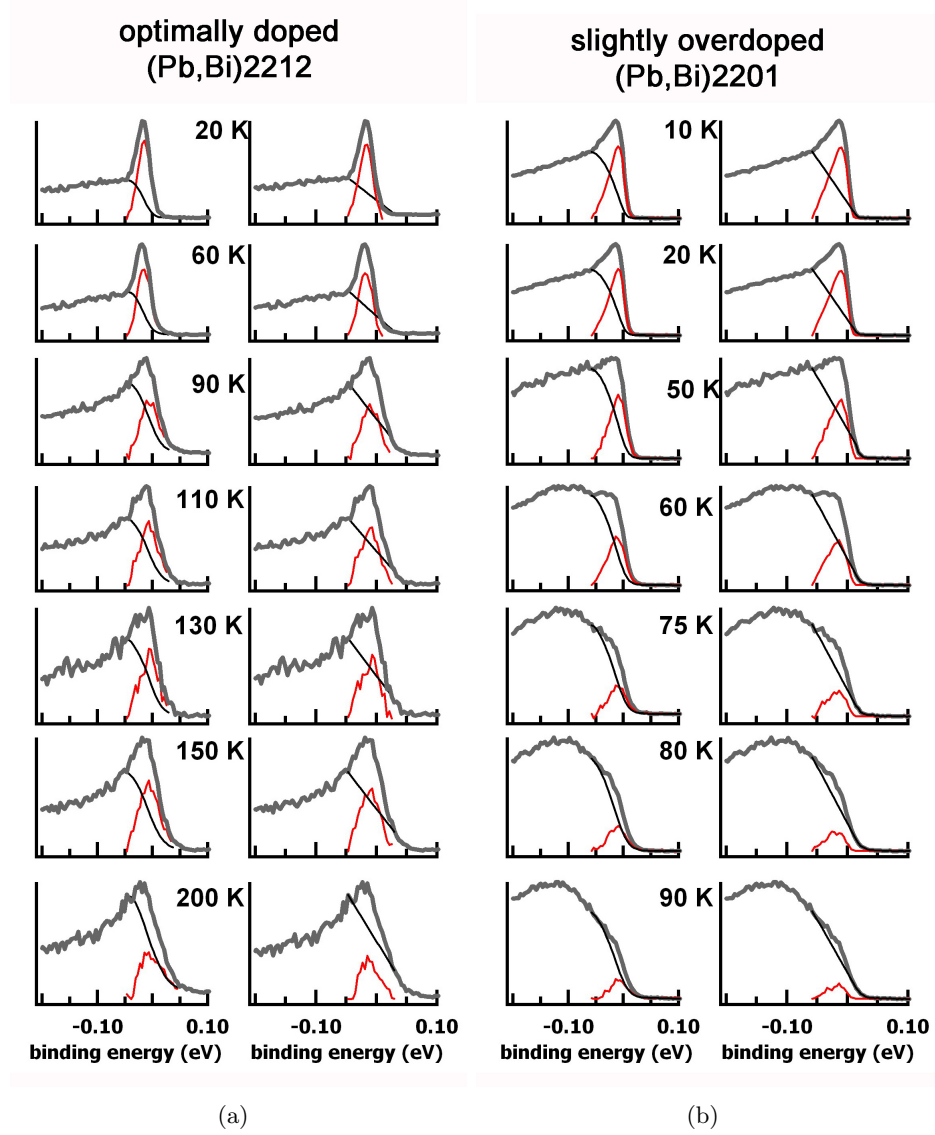
Figure 6.8: *Temperature dependent spectra.* **(a)** *M point of optimally doped (Pb,Bi)2212 sample with $T_c=91$ K and a lead concentration sufficient to suppress the $\approx(5x1)$ superstructure. Measurements were conducted at 50 eV photon energy and indicated temperature. Left and right column show the peak extraction with a Shirley and a linear background respectively. Substracted spectra are shown in black and extracted peaks in red.* **(b)** *Same as in (a) for slightly overdoped (Pb,Bi)2201 sample with $T_c=25$ K from fig. 6.2(b). The spectra, however, were not taken at the M point, but at 0.75 ΓM. In both samples the peak close to the Fermi surface persists to temperatures above T_c.*

Figure 6.9: *Results of analysis of temperature dependent data shown in fig. 6.8. **(a)** Peak ratio and widths of extracted peak versus temperature for the optimally doped (Pb,Bi)2212. The results of the Shirley background metho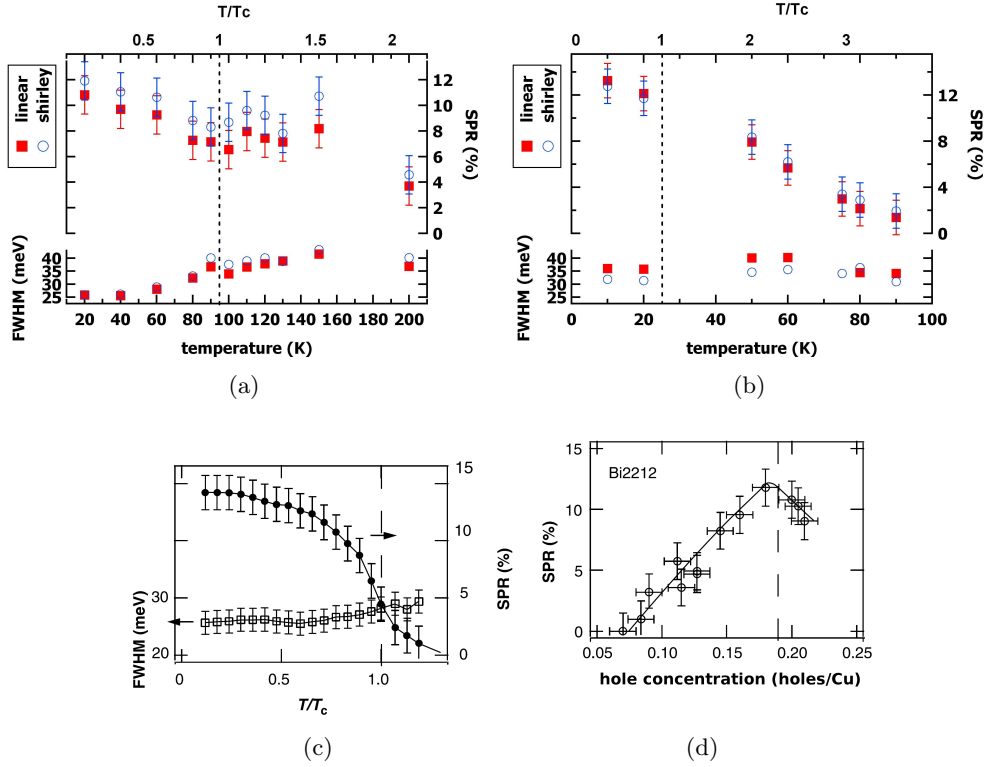d are shown with blue open circles, that of the linear extraction method with red full squares. For comparability with the figure from Feng et al.[89], here and in the other figures the peak ratio is denoted SPR on the scale, and on the top scale the temperature is given in T/T_c. Furthermore, T_c is marked with a broken line. **(b)** Same as in (a) for slightly overdoped (Pb,Bi)2201. **(c)** Peak ratio and width as observed for an overdoped Bi2212 sample with T_c=84 K by Feng et al.[89]. **(d)** Peak ratio versus hole concentration of doping series of Bi2212 also from Feng et al.[89].*

shows that the pseudogap temperature T* lies around 150 K in optimally doped double layer Bi cuprates. Hence, it can be stated that the additional excitation survives at least up to the pseudogap temperature T*. Depending on the form of the decrease between 150 K and 200 K, this would mean that the additional excitation starts to vanish or has vanished at temperatures above T*. At low temperatures the widths of the extracted peak is slightly higher than the energy resolution of 21 meV. Then it increases slightly due to temperature broadening.

This behavior shall now be compared to that found by Feng et al.[89] on a doping series of Bi2212. The results of the cited work are shown in fig. 6.9(c) and 6.9(d). The Bi2212 samples investigated by Feng et al.[89] were not substituted with lead. Their doping level was changed by varying the oxygen content. The very underdoped samples

were additionally doped by substituting Dy into the Ca layer that separates the adjacent CuO_2 planes in the double layer Bi cuprates. In fig. 6.9(c), the temperature evolution of the peak ratio and the widths of the extracted peak of an overdoped Bi2212 sample with T_c=84 K are plotted versus temperature. In comparison to the optimally doped (Pb,Bi)2212 sample probed within this work and shown in fig. 6.9(a), it is evident that the extracted peaks have a similar width, but the temperature evolution of the peak ratio is essentially different. The data of Feng et al.[89] suggest a decrease of the peak ratio with temperature, where already at T_c the peak ratio is reduced to about a third of its maximum value. And about 20 K above T_c it has totally vanished. Feng et al.[89] claim that this behavior has been observed for all samples. Hence, the differing behavior cannot be explained by the difference in hole concentration. Otherwise the compared samples vary only in that the sample studied here was substituted with lead in order to remove the $\approx$(5x1) superstructure which causes diffraction replica in the ARPES spectra. As dicussed in chapter 2, the lead substitution is known to make the system structurally cleaner and slightly raise the superconducting transition temperature T_c. It has, however, not yet been observed that the lead substitution changes the electronic structure or the high T_c superconductivity in the material in a dramatic way. Also, photoemission spectra have not been reported to differ substantially.

But, apart from differences regarding the sample, varying experimental conditions may explain the deviating observations. One essential modification done within this work is the photon energy at which the measurements were conducted. Although not given within the cited publication[89], it is stated that the experiments were done using a photon energy of 22.4 eV[187]. At such photon energy, however, the bonding band is rather strong. In opposition to that the sample studied here was measured at 50 eV photon energy where predominantly the antibonding band is probed. This can be seen when going back to the experimental spectra in fig. 6.5 and to the theoretical calculation of fig. 6.4. Especially, when comparing the experimental spectra around 21-22 eV and that of 50 eV the difference becomes apparent. Thus, it is hypothesized here that the bonding band present in the spectra at 22.4 eV covers part of the peak evolving with decreasing temperatures. Hence, at very low temperatures where the sharp peak contains the most spectral weight, the peak ratio has the same value regardless of photon energy. At higher temperatures, however, the sharp peak loses spectral weight and the features generally become broader. Thus, at photon energies with a strong bonding band, part of its spectral weight becomes covered because the onset of the sharp peak then automatically becomes defined by the dip between bonding and antibonding band. This hypothesis is further supported by the fact that the dip has been observed to vary in energy position at different photon energies. At high temperatures, finally, the bonding band which is anyway always rather broad and the antibonding band seem to merge and the featureless spectrum observed at photon energies with a strong bonding band emerges. To check that suggestion, fig. 6.10(a) shows temperature dependent ARPES spectra of the M point of an optimally doped Bi2212 sample with T_c=92 K. This sample was measured within the present work at a photon energy of 22 eV. The temperature dependent spectra clearly show the above described behavior. While at low temperatures the sharp peak and the dip between peak and hump can be observed, at higher temperatures the sharp

peak containing the antibonding band and the additional excitation are covered by the broad hump. Hence, the peak ratio over temperature (fig. 6.10(b)) shows a similar behavior as found by Feng et al.[89] (fig. 6.9(c)).

Another reason for the different conclusions regarding the temperature dependence may be that Feng et al.[89] integrated over a wider k-space region around the M point that they did not clearly specify, while within this work only the one spectrum at the M point was used. The averaging over a part of the dispersion possibly additionally enhances the effect of covering the sharp peak since the bilayer splitting changes within the Brillouin zone. At the M point both bands are seperated with the largest bilayer splitting.

Fig. 6.9(d) shows for the doping series studied by Feng et al.[89] the peak ratio as measured at T=20-30 K, but in any case below T_c, versus the hole content as determined by the relation of Presland et al.[68] (see also chapter 1.2.3 and eq. 1.5). The optimally doped (Pb,Bi)2212 sample with lead substitution measured within the present work lies within the curve of fig. 6.9(d) with its 12% SPR at optimal doping which is expectable from the argumentation from above. Since the sharp peak has the highest spectral weight at very low temperatures, the peak ratio is about the same regardless of experimental settings, at least for optimally and overdoped samples, where generally a strong sharp peak is observed.

Summarizing, it can be stated that while measuring the peak ratio at differently doped samples with consequently the same procedure and the same experimental conditions the relation over hole concentration given in fig. 6.9(d) may hold. But, the evolution of the sharp peak with temperature can only be clearly observed in double layer cuprates when suppressing the bonding band.

Finally, the results regarding temperature dependence of the optimally doped double layer Bi cuprate (Pb,Bi)2212 shall be compared to measurements on the slightly over-doped single layer Bi cuprate (Pb,Bi)2201 shown in fig. 6.2(b). In the figure, it can be seen that like in the optimally doped double layer (Pb,Bi)2212 the peak close to the Fermi surface persists to higher temperatures than T_c. This was quantified similary to the optimally doped double layer (Pb,Bi)2212 sample using the linear and Shirley background peak extraction method which can be seen in fig. 6.8(b). The temperatue dependent spectra of the single layer Bi cuprate (Pb,Bi)2201 were collected not at the M point, but at 0.75 ΓM. Therefore, the excitation that can be connected to the main band is still further away from the Fermi energy than at the M point as can also be deduced from the tight-binding plot of the band structure in fig. 6.2(c). The plot of peak ratio and width of extracted peak versus temperature are shown in fig. 6.9(b). Although slightly higher at 10 K, the peak ratio at 20 K is around the same value as that in the double layer (Pb,Bi)2212 sample of fig. 6.9(a). Since there exist no doping dependent data of the peak ratio for single layer Bi cuprates, it cannot be said, if the relation of fig. 6.9(c) is violated by the slightly overdoped single layer (Pb,Bi)2201 sample having a similar maximum value like the optimally doped (Pb,Bi)2212 sample. In any case the peak ratio decreases with rising temperature. The plateau-like behavior above T_c found in the double layer Bi cuprate cannot be observed, the decrease in intensity rather seems to be linear over the whole measured temperature region. This may result in the first
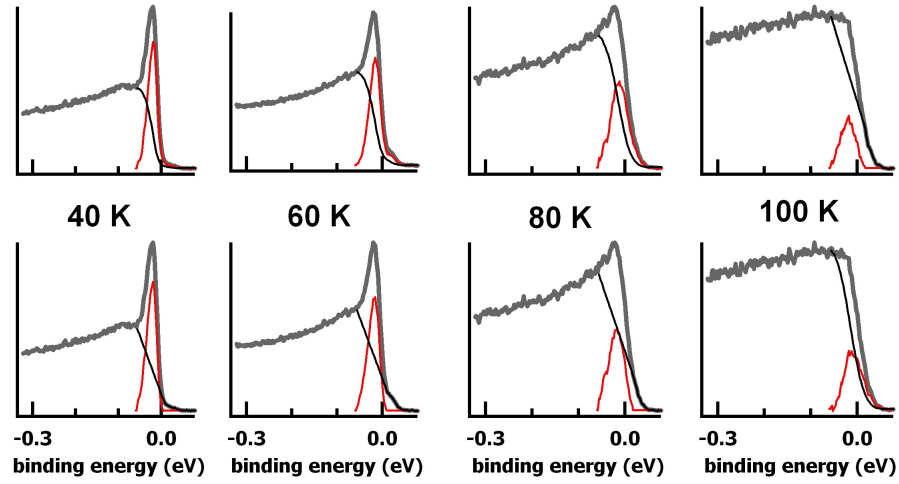
(a)
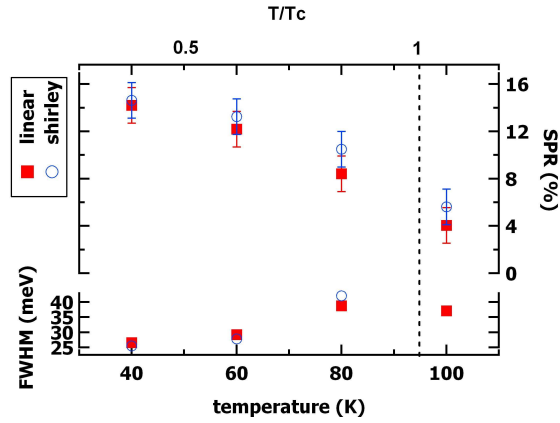
(b)

Figure 6.10: **(a)** *Temperature dependent spectra of the M point of an optimally doped Bi2212 sample with T_c=93 K and no lead substitution. Measurements were conducted at 22 eV photon energy and indicated temperature. Upper and lower column show the peak extraction with a Shirley and a linear background respectively. Substracted spectra are shown in black and extracted peaks in red.* **(b)** *Results of analysis of temperature dependent data of (a). The results of the Shirley background method are shown with blue open circles, that of the linear extraction method with red full squares. For comparability with the figure from Feng et al.[89], the peak ratio is denoted SPR on the scale, and on the top scale the temperature is given in T/T_c. Furthermore, T_c is marked with a broken line.*

place from the few available data points. The missing data points above T_c may hide the plateau-like bahvior. An other reason may be that the analyzed spectra stem from different k-points along the ΓM direction. The spectra of the single layer Bi cuprate (Pb,Bi)2201 originated at 0.75 ΓM, while the spectra of the double layer Bi cuprate (Pb,Bi)2212 were collected exactly at the M point. Furthermore, the two samples varied in their doping level. The studied sample of the double layer Bi cuprate (Pb,Bi)2212 was optimally doped. The single layer Bi cuprate (Pb,Bi)2201 was slightly overdoped. However, also in the single layer sample the pseudogap temperature T^* seems to play a role. For the slightly overdoped samples T^* lies around 70-80 K, and around 80 K the peak ratio in the single layer Bi cuprate has almost vanished reaching a value of 4% which is comparable to the peak ratio of the optimally doped double layer sample at 200 K. The widths of the extracted peak is slightly higher than in the double layer sample, although the energy resolution of the measurement on the single layer material is given as 16 meV and, thus, better than for the data of the double layer sample. It may be possible that because of the position along ΓM and the connected dispersion the extracted peak seems to be broader since the extraction is referenced at the higher binding energy excitation.

6.3.3 Summary of results

Before moving on to discussing and interpreting the results presented in this chapter they shall be shortly summarized. It could be shown that there exists an excitation additional to antibonding and bonding band close to the Fermi surface in the antinodal direction of the double layer Bi cuprate (Pb,Bi)2212. At the M point this additional excitation is separated from the antibonding excitation by approximately 15 meV. It was further demonstrated in the previous section that the determination of the temperature dependence of the spectral weight close to the Fermi surface as done by other groups[89,165] is ambiguous. The measurements conducted within this work revealed that the temperature dependence of the spectral weight at the Fermi surface clearly differs when varying the photon energy, and thus, the matrix elements of antibonding and bonding band. Within the present work the binding energy region of the sharp peak emerging at low temperatures was defined at such a low temperature where the sharp peak is strongest. The spectral weight of this region was then investigated in its temperature dependence. Since the existence of an additional emission close to the Fermi surface has been shown, it can be assumed that the studied binding energy region contains mainly this additional emission and hence, primarily the temperature dependence of this additional excitation is studied. In optimally doped double layer (Pb,Bi)2212 the spectral weight close to the Fermi surface has been found to decrease with increasing temperatures up to T_c. Above T_c it enters a plateau which ends presumably at a temperature higher than the pseudogap temperature T^*. Then this spectral weight totally vanishes.

In the beginning of this chapter the occurence of a sharp emission additional to the expected main band in the single layer cuprate (Pb,Bi)2201 was introduced. This sharp emission occurs close to the Fermi surface in the antinodal direction. It is separated from the main band at the M point by approximately 16 meV. This separation becomes larger

towards the Γ point. Furthermore, the sharp emission decreases in intensity coming from low temperatures and going towards T_c, but clearly persists up to temperatures above T_c. It vanishes at temperatures around the pseudogap temperature T^*.

6.4 Discussion and interpretation of results

In the following the physical origin of the additional excitation in double layer Bi cuprates, but also of the sharp emission found in single layer Bi cuprates, shall be explored. In section 1.2.3 the very complex phase diagram of the cuprates was laid out. Proposed models for superconductivity, some of which were introduced in section 1.3, have to account for this phase diagram and can only be experimentally probed by verifying predictions of changes of experimental parameters when crossing temperatures that separate different phases. In this regard, the ARPES results presented in the last sections shall be discussed especially in the context of the theory of charge inhomogeneity which derives high temperature superconductivity from a model of fluctuating stripe order. First, this model shall be briefly revisited focusing on predictions the model makes for observations in ARPES. Furthermore, some existing experimental evidence for stripes in cuprates is stated to put the application of this theory on more practical grounds. Then the ARPES results obtained within the present work will be interpreted in terms of the stripe model. In the end of this section, the arguments of BCS-like models that see evidence for a bosonic coupling mode in the peak-dip-hump structure will be briefly commented on, especially, from the view of the existence of the additional excitation in double layer Bi cuprates and the sharp emisison in single layer Bi cuprates.

Fig. 6.11(a) shows the phase diagram for the stripe model[73]. similar to the explanations given in section 1.3 superconductivity occurs below a pairing scale, here identified with the pseudogap temperature T^*_{pair}, and a scale of phase coherence, which is given as T^*_{3D} in the figure. Furthermore, there exists the temperature T^*_{stripe} below which stripe order forms. Recently, experimental evidence of static and dynamic stripe ordering in cuprates has been found using different methods. For instance by transport measurements in underdoped $La_{2-x}Sr_xCuO_4$[188], by elastic neutron scattering in $La_{1.62-x}Nd_{0.4}Sr_xCuO_4$[189,190], and elastic neutron scattering in YBCO[191], as well as several others[88]. It also seems the case that the whole magnetic spectrum in cuprates can best be explained when assuming stripe ordering. For a review concerning this last point see Tranquada[79]. Last not least, recent ARPES measurements on the single layer Bi cuprate (Pb,Bi)2201 conducted by our group[192] are supportive of static stripe ordering at a hole doping level of 1/10. Since the above mentioned reviews discuss the matter in great detail, it shall only be added here that static stripe order seems to destroy superconductivity, while dynamic stripe order, or fluctuations, are needed for high temperature superconductivity. But, dynamic stripe order is harder to detect, and so far has mostly been infered to exist by measurements of the magnetic excitation spectrum[79,88]. Upon entering the stripe phase, the system becomes quasi-one-dimensional and spin-charge separation is expected to occur. Because of this effect, there are no Fermi liquid-like quasiparticle excitations. The spectra close to the Fermi energy are broad and incoher-
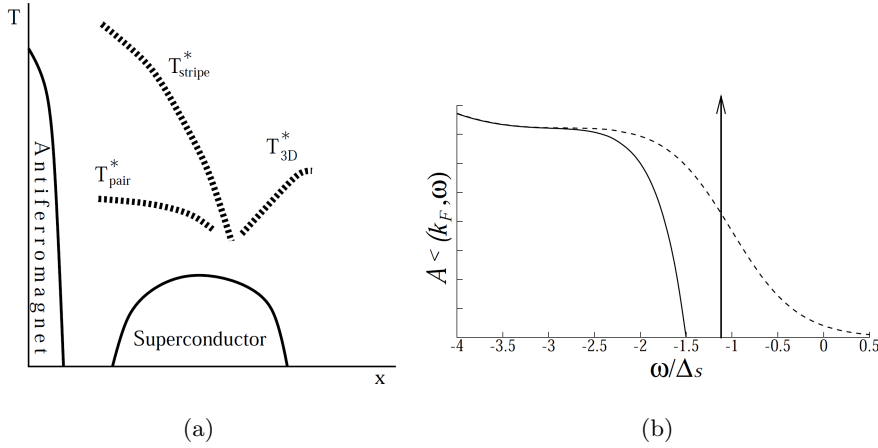
(a)   (b)

Figure 6.11: **(a)** *Phase diagram T(x), with x being the hole concentration, for the stripe model of high temperature superconductivity. Stripes appear below T^*_{stripe}, pairing starts below T^*_{pair}. T^*_{3D} marks the crossover from two- to threedimensionality. Below T^*_{pair} and T^*_{3D} the superconducting state emerges. Figure taken from Carlson et al.[73].* **(b)** *Spectral function A below (full line) and above T_c (dashed line) as given in Carlson et al.[73]. The energy scale is given in units of the spin gap Δ_s which opens below T^*_{pair}. While above T_c the excitations are incoherent, below T_c a sharp quasiparticle peak emerges (shown by the arrow). The incoherent part gets pushed to lower energies and a peak-dip-hump structure develops.*

ent. Furthermore, away from the Fermi surface two emissions become observable, one dispersing with the velocity of the holon and one with that of the spinon[73]. When entering the superconducting state the system becomes three-dimensional because of phase coherence. Thus, below T_c quasiparticles reminiscent of normal electrons appear[73,193]. Hence, there will be a rapid increase of the spectral weight, when crossing T_c. However, since the gap already opens below T^*_{pair}, the energy position of the excitation will not change considerably when crossing T_c. The same holds for the peak width. The changes in the spectral function at the Fermi energy when entering the superconducting state as theoretically treated by Carlson et al.[193] are illustrated in fig. 6.11(b). Above T_c, there is the incoherent spectrum which dramatically changes below T_c to a peak-dip-hump-like structure. The peak, symbolized by the arrow in the figure, contains the coherent spectral weight, while the incoherent part is pushed to higher energies into the hump structure. Between the two a dip develops. All these predictions are in strong contrast to the situation within the BCS meachanism. There above the superconducting state the system is a Fermi liquid. Hence, there are well defined quasiparticles above and below T_c, and the spectral weight does not change rapidly when crossing T_c. But, the superconducting gap opens below T_c. Therefore, the energy and the scattering rate of the quasiparticle is expected to change abruptly.

Now, it shall be explored to what extend the ARPES measurements conducted within the present work fulfill those predictions. First, the existence of the different temperature scales will be explored. These are T_c, T^*, and T^*_{stripe}, if T^*_{pair} is identified with

the pseudogap temperature T*. Furthermore, for the optimally doped double layer Bi cuprate and the slightly overdoped single layer cuprate of which the temperature dependence of the spectral weight at the Fermi surface has been studied, T^*_{3D} can be set to T_c. Only in highly overdoped samples the crossover to three-dimensionality may occur above T_c as can be seen in fig. 6.11(a). In addition, it shall be noted here that with rising doping the distance between T* and T^*_{stripe} becomes smaller. It is, thus, expectable that T* and T^*_{stripe} lie very close together for the slightly overdoped sample.

As discussed above, the spectral weight in the double layer Bi cuprate (Pb,Bi)2212 was found to steadily decrease with rising temperatures until T_c is reached, above which it enters a plateau. This is conform with the predictions of a marked change of the spectral weight when crossing T_c. Although the single layer Bi cuprate has a much lower T_c than the double layer such a decrease in spectral weight is also indicated. Furthermore, there is a second temperature scale visible at much higher temperatures than T_c in the double layer Bi cuprate. Namely,the point where the plateau ends, and the spectral weight again decreases. This temperature cannot be exactly quantified, but, was found to be around or above the pseudogap temperature T*. Thus, it may correlate with changes occuring upon crossing T^*_{stripe} of the phase diagram in fig. 6.11(a). Because of the few data points the behavior of the spectral weight in the single layer Bi cuprate (Pb,Bi)2201 is not as clear. In any case, the spectral weight is decreasing with rising temperature. How rapid the change above T_c is, cannot be judged, but, the sharp peak persists to temperatures far above T_c, presumably up to T*. As was mentioned above, for this slightly overdoped sample T* and T^*_{stripe} lie very close together, and can probably both be identified.

Within this interpretation, the sharp emission found in the single Bi cuprate (Pb,Bi)-2201 and the additional excitation observed in the double layer Bi cuprate (Pb,Bi)2212 have a different origin below and above T_c. Below T_c, they represent the coherent part of the spectral weight of the quasiparticle emerging upon reaching phase coherence and concomitant entrance into the superconducting state. Assuming, the temperature where the spectral weight totally vanishes above T* is the temperature of stripe formation T^*_{stripe}, the occurence of two excitations instead of the one expected from band calculations may be the signature of spin-charge separation. For the single layer Bi cuprate (Pb,Bi)2201 this interpretation was already also explored by Janowitz et al.[12]. The two dispersions measured above T_c scale with a factor of 2.7 which may be a realistic scaling factor for the spinon and holon dispersion[73,194]. However, the sharp emission has been shown to exhibit an unusual polarization dependence (sec. 6.2), which would in this context imply differing polarization dependencies of the spinon and holon excitation. According to the derivations of section 6.1, this would mean their wave functions have to be of differing symmetry. If this is possible, remains to be answered by theory. So far no theoretical treatments of this problem have come to my attention. But, within the above given interpretation a differing polarization dependence should be forbidden below T_c since sharp and broad feature are here accounted for by the PDH structure of one and the same quasiparticle excitation. Out of the same reason, there may also be a change in the dispersion of the two features below T_c. Hence, polarization dependent measurements below and above T_c are needed. Within the double layer Bi cuprate (Pb,Bi)2212

the temperature region above T_c is harder to explore because of the high T_c and the resulting temperature broadening. Here, the single layer Bi cuprate with its low T_c is a much better candidate for studying dispersions and polarization dependencies. The double layer Bi cuprate, however, is the drosophila of ARPES in high T_c cuprates. This is on the one hand because of the easy cleaving between the adjacent BiO layers which are only van der Waals bonded, and on the other hand because it could be synthesized with sufficient sample quality earlier than the single layer Bi cuprate. Hence, in order to reach a clear and uniform picture, it will always be necessary to validate findings made in the single layer Bi cuprate also on the double layer Bi cuprate and vice versa, as has been done within this work.

At this point it shall be commented that within the stripe model of high temperature superconductivity the coherent spectral weight is expected to scale with the superfluid density[73]. Thus, it should not only rapidly increase below T_c, but also scale with hole concentration as the superfluid density. Such a scaling supportive of the stripe model of superconductivity has been found by Feng et al.[89] and Ding et al.[165] as mentioned in the previous section. There it has also been discussed that this scaling should hold when it is done for all samples at the same experimental conditions, even though the extraction of spectral weight as done by Feng et al.[89] has been shown to be ambiguous.

It shall also be added here that after the proposal of the RVB state for the cuprates[43] it was suggested that the RVB state may lead to spin-charge separation[195]. But, groups studying the RVB theory seem not to follow this idea[196,197]. However, also within the RVB theory there exists a coherence temperature that rises with increasing hole concentration similar to T_{3D}^* in the stripe model (see also sec. 1.3). Hence, while the observation of signatures of spin-charge separation may be ambivalently discussed within the RVB theory, the emergence of quasiparticles below T_c marked by a rapid increase in spectral weight is also supportive of this theory[196,197], as well as the scaling of the spectral weight with hole concentration[89,165]

Finally, the observations shall also be discussed within BCS-like models that look for a bosonic pairing mode. As discussed in section 1.3, this does not have to be a phonon as in BCS theory, but could also be a magnetic mode. According to quasiparticle theory, interactions of the quasiparticle with collective modes can be accounted for by the self-energy similarly to eq. (3.10). The specifics are illustrated in fig. 6.12. At the mode energy the imaginary part of the self energy will become a step-like function, and the real part will exhibit a cusp. According to section 3.3 and eq. (3.10), this results in the spectral function acquiring a peak-dip-hump lineshape (PDH), with the dip at the mode energy. Furthermore, the real part of the self-energy rescales the non-interacting dispersion, which leads to a kink in the dispersion at the mode energy in the vicinity of the Fermi energy.

Very recently, the emergence of a sharp emission similar to that reported in section 6.2 has been observed by Wei et al.[199] in the antinodal region in single layer Bi2201. Hence, close to the Fermi surface the lineshape consists of a sharp emission at lower binding energy and a broader one at higher binding energy. Although this was not clearly stated by Wei et al.[199], it can be deduced from the data presented in the cited publication that the broad emission shows the dispersion of the main band. Close to the M point,
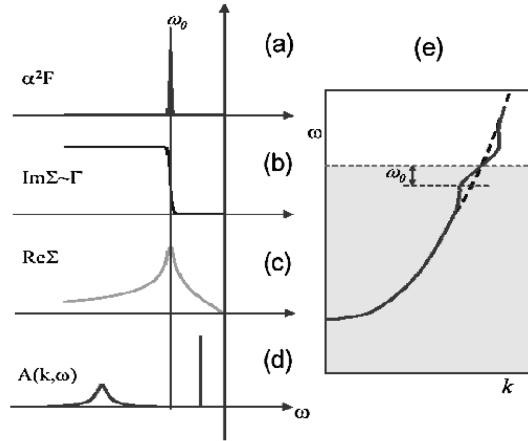
Figure 6.12: *Coupling of electrons to a collective mode. Figure taken from Johnson and Valla* [198]. *(a) Collective mode given by an Eliashberg function $\alpha^2 F$ which is represented in this simple picture by a Gaussian at the mode energy ω_0. (b) The imaginary part of the self-energy Σ will become a step function at the mode energy, and (c) the real part of the self energy Σ will exhibit a cusp at the mode energy. (d) The resulting spectral function will show a peak above, and a hump below the mode energy. At the mode energy will be a dip. (e) In the vicinity of the Fermi energy there will be a kink-like feature in the dispersion of the quasiparticle.*

the two features are almost inseparable. Fig. 6.13 shows two spectra close to the M point of optimally doped single layer Bi2201 from Wei et al. [199]. Cut number 8 (on the right og fig. 6.13) shows the dispersion of the band when crossing the Fermi surface in the antinodal region at the Brillouin zone boundary. An almost dispersionless sharp peak is observed which is deduced to consist of peak and hump since at this point peak and hump are almost inseparable. No kink is present. In cut number 5 (on the left of fig. 6.13) the band is still further away from the Fermi energy. Hence, the hump can be observed to disperse towards the Fermi energy. It is notable that the sharp emission close to the Fermi energy in cut number 8 shows again almost no dispersion. If disregarding the existence of the sharp emission, one could actually jump from the dispersion of the broad emission into the position of the sharp emission, and thus, easily create a kink. The two separate features, however, do not exhibit kinks. Hence, the broad and sharp emission found in single layer Bi cuprates forms a PDH lineshape, but, no kink could be observed. This, however, implies that the PDH lineshape, and hence, also the splitting into sharp and broad emission as discussed above, cannot be accounted for by the model of coupling to a collective mode or the dressing of charge carriers.

The peak-dip-hump (PDH) lineshape in the antinodal region of the double layer Bi cuprates has often been interpreted in terms of coupling to a bosonic mode, and also the observation of an antinodal kink has been claimed in this material [200–203]. The different groups argue about the mode being phononic or bosonic. For the respective arguments the reader can refer to reviews [10,90]. Because of the complexity of the lineshape due to bilayer splitting effects in double layer cuprates, the extraction of intrinsic effects is very
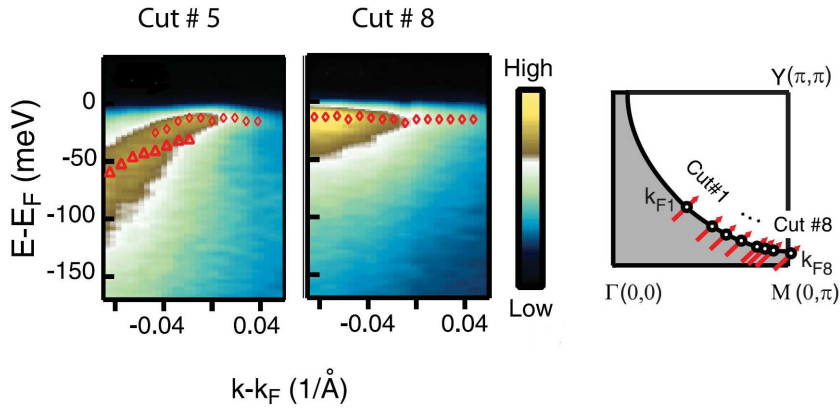
Figure 6.13: *Energy distribution maps of ARPES measurement at T=20 K of an optimally doped single layer Bi cuprate Bi2201, T_c=34 K. The measured region is indicated in the sketch of the Brillouin zone on the left.*

complicated, as has been discussed in depth in previous sections. In most investigations of possible kinks in the dispersion the lineshapes of bonding and antibonding band have only been distinguished by deduction. These publications report ARPES measurements at 20-22 eV where both bands are rather strong. Hence, an experimental separation or at least a cross check was not conducted. Only Kim et al.[203] claim to have observed a PDH lineshape and kink of the bonding band in the antinodal direction by exploiting the dependence of the matrix elements of bonding and antibonding band. They conducted ARPES measurements at photon energies of hν=38 eV where at the M point the bonding band is strong, but the antibonding band still present, and hν=50 eV, where at the M point mainly the antibonding band is present. Subsequently, the bonding band was extracted by substracting the 50 eV spectrum from the one taken at 38 eV photon energy. Besides problems on normalization when substracting spectra, the exploitation of matrix element effects away from the ΓM direction is questionable. Detailed lineshape analysis of changes in the matrix element with photon energy has so far only been conducted exactly at the M point[167] which was also verified within the present work. Also, calculations[183] of the photon energy dependence of bonding and antibonding band showed the dependence on the location in the Brillouin zone. The method of substraction has to be further questioned in light of the observation of an additional excitation close to the Fermi energy in the antinodal direction in the double layer Bi cuprate (Pb,Bi)2212 discussed in the previous section. If the additional excitation reported in the previous sections, actually is connected to the antibonding band, the bonding band will with high probability exhibit a similar behavior. This excitation additional to the bonding band may not be observable along ΓM where the bonding band is further away from the Fermi energy and rather broad. But, Kim et al.[203] investigated the bonding band off the ΓM direction close to its Fermi surface crossing. If on the other hand, the additional excitation is independent of bonding or antibonding band, it may even have a different

dependence on photon energy than bonding and antibonding band at different k points. And lastly, the argument of creating a kink when actually observing two emissions that was given in connection to the spectra of the single layer Bi cuprate from Wei et al. [199] holds also here. Regarding the interpretation of the lineshape in Bi cuprates in terms of coupling to a collective mode in the antinodal direction, it can be summarized that the observations of a PDH and a kink in the dispersion of double layer Bi cuprates is equivocal, because of the complex lineshape due to bilayer splitting and the observation of the additional excitation close to the Fermi surface.

Summarizing, it can be stated that the ARPES results obtained within this work can be explained within the stripe model regarding the observed temperature dependence in the single and double layer Bi cuprates and the dispersion of the sharp emission in the single layer Bi cuprate above T_c. The PDH lineshape resulting from the splitting in sharp and broad emission in single layer Bi cuprates cannot be explained within a mode coupling scenario. In double layer cuprates the interpretation of spectra with a bosonic coupling mode seems at least equivocal.

7

Conclusion

Within this PhD work the specific variation of matrix elements has been used to obtain spectroscopic evidence that looks beyond aspects of the electronic structure of high-T_c cuprates that are commonly regarded as established. Particularly, defined polarization settings within the CuO_2 plane revealed an unexpected polarization dependence in x-ray absorption that challenges the sufficiency of commonly used single-band models for describing the electronic structure of cuprates. Furthermore, the defined variation of the photon energy in angle resolved photoemission enabled to distinguish between the bilayer split bands. This in interplay with selective polarization settings paved the way to observe an emission additional to the ones derived by conventional quasiparticle-like theories in double layer Bi cuprates. Thus, differing previous observations on the single and double layer Bi cuprate could be reconciled.

Varying the polarization vector of the incoming light within the CuO_2 plane revealed an unexpected in-plane polarization dependence in x-ray absorption that shows signatures of the axial hybrid orbital[58]. Axial refering here to the derivation of the electronic structure by incorporating orbitals perpendicular to the CuO_2 plane and, thus, going beyond the normally infered two-dimensionality of the cuprates. Furthermore, samples with doping levels covering almost the whole superconducting dome have been investigated. Thus, it could be confirmed that the model of spectral weight transfer between Zhang-Rice-singlet and upper Hubbard band captures the basic features, however, also supporting evidence for a possible breakdown of the Zhang-Rice-singlet picture in the overdoped regime could be found. Hence, the observation of signatures of the axial hybrid orbital also within the plane, emphasize the need to keep the surrounding of the CuO_2 plane in mind, when discussing the cuprates. Moreover, the systematics over the superconducting dome shows that simplified single-band models of the strongly correlated charge-transfer insulator may not fully describe the electronic structure.

By exploiting the differing photon energy dependence of the matrix elements of bonding and antibonding band in angle resolved photoemission, both bands could be experimentally distinguished. Thus, the characteristics of the antibonding band only could be investigated and compared to the measurements on the single layer Bi cuprate. The

emergence of an excitation additional to the antibonding band which seems to be connected to the antibonding band could be shown in the double layer Bi cuprate. This additional excitation relates to the previous report of a sharp peak in the single layer Bi cuprates[11,12,168,169]. The observation of this additional excitation and its characteristics enabled to derive a unified picture of the temperature dependence of the spectral weight close to the Fermi surface in the antinodal direction in single and double layer Bi cuprates. But, also differing observations of renormalizations in the dispersion close to the Fermi surface in the antinodal region could be reconciled. The spectral weight close to the Fermi surface, and thus the additional excitation in double layer Bi cuprates and the correspoding sharp peak in single layer Bi cuprates could be shown to persist at least up to the pseudogap temperature T^*, presumably even higher. These observations could be most consistently explained within the model of electronic inhomogeneity in cuprates where high temperature superconductivity is derived from stripes.

It is undisputed that strong correlations play the essential role in the physics of the cuprates. But, simplified views of the charge-transfer insulator focussing on the two-dimensional CuO_2 plane alone probably fail to provide details that may be essential for understanding the cuprates. The results obtained within this thesis can be in their entirety best explained within the model of "dynamic inhomogeneity induced pairing" that derives superconductivity from stripe ordering.

Bibliography

[1] J.G. Bednorz and K.A. Müller. Possible high T_c superconductivity in the Ba-La-Ca-o System. *Z. Phys. B*, 64:189, 1986.

[2] J. A. Slezak, Jinho Lee, M. Wang, K. McElroy, K. Fujita, B. M. Andersen, P. J. Hirschfeld, H. Eisaki, S. Uchida, and J. C. Davis. Imaging the impact on cuprate superconductivity of varying the interatomic distances within individual crystal unit cells. *Proceedings of the National Academy of Sciences*, 105(9):3203–3208, 2008. and references therein.

[3] C. T. Chen, L. H. Tjeng, J. Kwo, H. L. Kao, P. Rudolf, F. Sette, and R. M. Fleming. Out-of-plane orbital characters of intrinsic and doped holes in $La_{2-x}Sr_xCuO_4$. *Phys. Rev. Lett.*, 68(16):2543–2546, 1992.

[4] A. J. Leggett. Cuprate superconductivity: Dependence of t_c on the c-axis layering structure. *Phys. Rev. Lett.*, 83(2):392–395, Jul 1999.

[5] Y. Ohta, T. Tohyama, and S. Maekawa. Apex oxygen and critical temperature in copper oxide superconductors: Universal correlation with the stability of local singlets. *Phys. Rev. B*, 43(4):2968–2982, Feb 1991.

[6] Sudip Chakravarty, Hae-Young Kee, and Klaus Volker. An explanation for a universality of transition temperatures in families of copper oxide superconductors. *Nature*, 428:53, 2004.

[7] T. H. Geballe and G. Koster. *Handbook of High-Temperature Superconductivity*, chapter 8, page 325. Springer, 2007.

[8] E. Pavarini, I. Dasgupta, T. Saha-Dasgupta, O. Jepsen, and O. K. Andersen. Band-structure trend in hole-doped cuprates and correlation with $T_{c,max}$. *Phys. Rev. Lett.*, 87(4):047003, 2001.

[9] A. Damascelli, Z. Hussain, and Z.-X. Shen. Angle-resolved photoemission studies of the cuprate superconductors. *Rev. Mod. Phys.*, 75:473, 2003. references therein.

[10] X. J. Zhou, T. Cuk, T. Devereaux, N. Nagaosa, and Z-X. Shen. *Handbook of High-Temperature Superconductivity*, chapter 3, page 87. Springer, 2007. references therein.

[11] Recardo Manzke, Lenart Dudy, Alica Krapf, Christoph Janowitz, and Hartmut Höchst. One-dimensional electronic structure effects of single-layer cuprates Bi-2201 and Bi(Pb)-2201. *Physica C: Superconductivity*, 408-410:780 – 782, 2004. Proceedings of the International Conference on Materials and Mechanisms of Superconductivity. High Temperature Superconductors VII – M2SRIO.

[12] C. Janowitz, R. Müller, L. Dudy, A. Krapf, R. Manzke, C. Ast, and H. Höchst. Unusual electronic ground state of a prototype cuprate: band splitting of single CuO$_2$-plane $Bi_2Sr_{2-x}La_xCuO_{6+\delta}$. *Europhys. Lett.*, 60:615, 2002.

[13] L. Dudy. *Nature and organization of the CuO$_2$-plane as experimentally probed in the prototype high-temperature superconductor Bi2201*. PhD thesis, HU Berlin, 2008.

[14] H. Kamerlingh Onnes. The resistance of pure mercury at helium temperatures. *Leiden Comm.*, 120b, 1911.

[15] W. Meissner and R. Ochsenfeld. Ein neuer Effekt bei Eintritt der Supraleitfähigkeit. *Naturwissenschaften*, 21:787, 1933.

[16] J. Bardeen, L.N. Cooper, and J.R. Schrieffer. Theory of superconductivity. *Phys. Rev.*, 108:1175, 1957.

[17] E. Maxwell. Isotope effect in the superconductivity of mercury. *Phys. Rev.*, 78(4):477, May 1950.

[18] C. A. Reynolds, B. Serin, W. H. Wright, and L. B. Nesbitt. Superconductivity of isotopes of mercury. *Phys. Rev.*, 78(4):487, 1950.

[19] H. Fröhlich. Theory of the superconducting state. i. the ground state at the absolute zero of temperature. *Phys. Rev.*, 79(5):845–856, Sep 1950.

[20] F. London and H. London. The electromagnetic equations of the supraconductor. *Proceedings of the Royal Society of London. Series A, Mathematical and Physical Sciences*, 149(866):71–88, 1935.

[21] V. L. Ginzburg and L. D. Landau. *Zh. Eksp. Teor. Fiz.*, 20:1064, 1950.

[22] G. Burns. *High-temperature superconductivity*. Academic Press Inc., 1992.

[23] C. Buzea and T. Yamashita. Review of superconducting properties of MgB$_2$. *SCIENCE AND TECHNOLOGY*, 14:R115, 2001.

[24] Jun Nagamatsu, Norimasa Nakagawa, Takahiro Muranaka, Yuji Zenitani, and Jun Akimitsu. Superconductivity at 39 K in magnesium diboride. *Nature*, 410:63, 2001.

[25] A. F. Hebard, M. J. Rosseinsky, R. C. Haddon, D. W. Murphy, S. H. Glarum, T. T. M. Palstra, A. P. Ramirez, and A. R. Kortan. Superconductivity at 18 K in potassium-doped C$_{60}$. *Nature*, 350:600, 1991.

[26] Andrei Mourachkine. *Room-Temperature Superconductivity.* Cambridge International Science Publishing, 2004.

[27] O. Gunnarsson. Superconductivity in fullerides. *Rev. Mod. Phys.*, 69(2):575–606, 1997.

[28] Serena Margadonna and Kosmas Prassides. Recent advances in fullerene superconductivity. *Journal of Solid State Chemistry*, 168(2):639 – 652, 2002.

[29] K. H. Bennemann and J. B. Ketterson, editors. *The Physics of Superconductors*, volume 1. Springer, 2003.

[30] Yoichi Kamihara, Takumi Watanabe, Masahiro Hirano, and Hideo Hosono. Iron-based layered superconductor La[$O_{1-x}F_x$]FeAs (x = 0.05-0.12) with T_c = 26 K. *Journal of the American Chemical Society*, 130(11):3296–3297, 2008.

[31] Michael R. Norman. High-temperature superconductivity in the iron pnictides. *Physics*, 1:21, Sep 2008.

[32] Zhi-An Ren, Guang-Can Che, Xiao-Li Dong, Jie Yang, Wei Lu, Wei Yi, Xiao-Li Shen, Zheng-Cai Li, Li-Ling Sun, Fang Zhou, and Zhong-Xian Zhao. Superconductivity and Phase Diagram in the Iron-based Arsenic-oxides ReFeAsO$_{1-\delta}$ (Re = rare earth metal) without F-Doping. *Europhys. Lett.*, 83:17002, 2008.

[33] N. Motoyama, H. Eisaki, and S. Uchida. Magnetic susceptibility of ideal spin 1/2 heisenberg antiferromagnetic chain systems, Sr_2Cuo_3 and $SrCuO_2$. *Phys. Rev. Lett.*, 76(17):3212–3215, 1996.

[34] Masashi Hase, Ichiro Terasaki, and Kunimitsu Uchinokura. Observation of the spin-Peierls transition in linear Cu^{2+} (spin-1/2) chains in an inorganic compound $CuGeO_3$. *Phys. Rev. Lett.*, 70(23):3651–3654, 1993.

[35] Henry Krakauer and Warren E. Pickett. Effect of bismuth on high-T_c cuprate superconductors: Electronic structure of $Bi_2Sr_2CaCu_2O_8$. *Phys. Rev. Lett.*, 60 (16):1665–1667, 1988.

[36] N.F. Mott. Metal-insulator transitions. *Proc. Roy. Soc.*, A 62:416, 1949.

[37] J. Hubbard. Electron correlation in narrow energy bands. *Proc. Roy. Soc.*, A 276: 238, 1963.

[38] J. Zaanen, G.A. Sawatzky, and J.W. Allen. Band-gaps and electronic structure of transition-metal compounds. *Phys. Rev. Lett.*, 55:418, 1985.

[39] M. Imada, A. Fujimori, and Y. Tokura. Metal-insulator transitions. *Rev. Mod. Phys.*, 70:1039, 1998.

[40] V. J. Emery. Theory of high-T_c superconductivity in oxides. *Phys. Rev. Lett.*, 58 (26):2794–2797, 1987.

[41] V. J. Emery and G. Reiter. Quasiparticles in the copper-oxygen planes of high-T_c superconductors: An exact solution for a ferromagnetic background. *Phys. Rev. B*, 38(16):11938–11941, 1988.

[42] V. J. Emery and G. Reiter. Mechanism for high-temperature superconductivity. *Phys. Rev. B*, 38(7):4547–4556, 1988.

[43] P.W. Anderson. The Resonating Valence Bond State in La_2CuO_4 and Superconductivity. *Science*, 235:1196, 1987.

[44] P. W. Anderson. New approach to the theory of superexchange interactions. *Phys. Rev.*, 115(1):2, 1959.

[45] Jozef Spalek. t-J model then and now: A personal perspective from the pioneering times. *ACTA PHYSICA POLONICA A*, 111:409, 2007. arXiv:0706.4236v1 [cond-mat.str-el].

[46] D. Vaknin, S. K. Sinha, D. E. Moncton, D. C. Johnston, J. M. Newsam, C. R. Safinya, and H. E. King. Antiferromagnetism in La_2CuO_{4-y}. *Phys. Rev. Lett.*, 58 (26):2802–2805, 1987.

[47] G. Shirane, Y. Endoh, R. J. Birgeneau, M. A. Kastner, Y. Hidaka, M. Oda, M. Suzuki, and T. Murakami. Two-dimensional antiferromagnetic quantum spin-fluid state in La_2CuO_4. *Phys. Rev. Lett.*, 59(14):1613–1616, 1987.

[48] K. B. Lyons, P. A. Fleury, L. F. Schneemeyer, and J. V. Waszczak. Spin fluctuations and superconductivity in $Ba_2YCu_3O_{6+\delta}$. *Phys. Rev. Lett.*, 60(8):732–735, 1988.

[49] Shunji Sugai, Shin-ichi Shamoto, and Masatoshi Sato. Two-magnon raman scattering in $(La_{1-x}Sr_x)_2CuO_4$. *Phys. Rev. B*, 38(10):6436–6439, 1988.

[50] G. Blumberg, P. Abbamonte, M. V. Klein, W. C. Lee, D. M. Ginsberg, L. L. Miller, and A. Zibold. Resonant two-magnon raman scattering in cuprate antiferromagnetic insulators. *Phys. Rev. B*, 53(18):R11930–R11933, 1996.

[51] P. Bourges, H. Casalta, A. S. Ivanov, and D. Petitgrand. Superexchange coupling and spin susceptibility spectral weight in undoped monolayer cuprates. *Phys. Rev. Lett.*, 79(24):4906–4909, 1997.

[52] G. Blumberg, M. Kang, M.V. Klein, K. Kadowaki, and C. Kendziora. Evolution of Magnetic and Superconducting Fluctuations with Doping of High-Tc Superconductors. *Science*, 273:1427, 1997.

[53] F.C. Zhang and T.M. Rice. Effective hamiltonian for the superconducting Cu oxides. *Phys. Rev. B*, 37:3759, 1988.

[54] H. Eskes and G. A. Sawatzky. Tendency towards local spin compensation of holes in the high-T_c copper compounds. *Phys. Rev. Lett.*, 61(12):1415–1418, 1988.

[55] H. Eskes and G. A. Sawatzky. Single-, triple-, or multiple-band hubbard models. *Phys. Rev. B*, 44(17):9656–9666, 1991.

[56] J. Orenstein and A.J. Millis. Advances in the physics of high-temperature super-conductivity. *Science*, 288:468, 2000.

[57] M. R. Norman and C. Pepin. The electronic nature of high temperature cuprate superconductors. *Reports on Progress in Physics*, 66(10):1547–1610, 2003.

[58] O. K. Andersen, A. I. Liechtenstein, O. Jepsen, and F. Paulsen. LDA energy bands, low-energy hamiltonians, t', t", $t_\perp(k)$, and $J_\perp$. *Journal of Physics and Chemistry of Solids*, 56(12):1573 – 1591, 1995. Proceedings of the Conference on Spectroscopies in Novel Superconductors.

[59] K. Tanaka, T. Yoshida, A. Fujimori, D. H. Lu, Z.-X. Shen, X.-J. Zhou, H. Eisaki, Z. Hussain, S. Uchida, Y. Aiura, K. Ono, T. Sugaya, T. Mizuno, and I. Terasaki. Effects of next-nearest-neighbor hopping t' on the electronic structure of cuprate superconductors. *Phys. Rev. B*, 70(9):092503, 2004.

[60] N. E. Hussey, M. Abdel-Jawad, A. Carrington, A. P. Mackenzie, and L. Balicas. A coherent three-dimensional Fermi surface in a high-transition-temperature superconductor. *Nature*, 425:814, 2003.

[61] T. Xiang and J. M. Wheatley. *c* axis superfluid response of copper oxide super-conductors. *Phys. Rev. Lett.*, 77(22):4632–4635, 1996.

[62] V. J. Emery and S. A. Kivelson. Importance of phase fluctuations in superconductors with small superfluid density. *Nature*, 374:434, 1995.

[63] V. J. Emery and S. A. Kivelson. Superconductivity in bad metals. *Phys. Rev. Lett.*, 74(16):3253–3256, 1995.

[64] N. E. Hussey. *Handbook of High-Temperature Superconductivity*, chapter 10, page 399. Springer, 2007.

[65] D. J. Scalapino. The case for $d_{x^2-y^2}$ pairing in the cuprate superconductors. *Physics Reports*, 250(6):329 – 365, 1995.

[66] C. C. Tsuei and J. R. Kirtley. *Superconductivity*, volume 2, chapter 16, page 869. Springer, 2008.

[67] C. C. Tsuei and J. R. Kirtley. Pairing symmetry in cuprate superconductors. *Rev. Mod. Phys.*, 72(4):969, 2000.

[68] M. R. Presland, J. L. Tallon, R. G. Buckley, R. S. Liu, and N. E. Flower. General trends in oxygen stoichiometry effects on T_c in Bi and Tl superconductors. *Physica C*, 176:95, 1991.

[69] Tom Timusk and Bryan Statt. The pseudogap in high-temperature superconductors: an experimental survey. *Reports on Progress in Physics*, 62(1):61–122, 1999.

[70] T. Timusk. The mysterious pseudogap in high temperature superconductors: an infrared view. *Solid State Communications*, 127(5):337 – 348, 2003.

[71] S. Hüfner, M. A. Hossain, A. Damascelli, and G. A. Sawatzky. Two gaps make a high-temperature superconductor? *Rep. Prog. Phys.*, 71:062501, 2008.

[72] M. R. Norman, D. Pines, and C. Kallin. The pseudogap: friend or foe of high Tc? *Advances in Physics*, 54:715, 2005.

[73] E. W. Carlson, V. J. Emery, S. A. Kivelson, and D. Orgad. *Superconductivity*, volume 2, chapter 21, page 1225. Springer, 2008.

[74] A. B. Migdal. *Zh. Eksp. Teor. Fiz.*, 34:1438, 1958.

[75] J. R. Waldram. *Superconductivity of metals and cuprates*. IOP Publishing, 1996.

[76] K. M. Shen and Z.-X. Shen. *Very high resolution photoemission*, volume 715 of *Lect. Notes Phys.*, chapter 9, page 243. Springer, 2007.

[77] K. A. Müller. *Handbook of High-Temperature Superconductivity*, chapter 1, page 1. Springer, 2007.

[78] C. P. Slichter. *Handbook of High-Temperature Superconductivity*, chapter 5, page 215. Springer, 2007.

[79] J. M. Tranquada. *Handbook of High-Temperature Superconductivity*, chapter 6, page 257. Springer, 2007.

[80] A. V. Chubukov, D. Pines, and J. Schmalian. *Superconductivity*, volume 2, chapter 22, page 1349. Springer, 2008.

[81] D. Manske, I. Eremin, and K. H. Bennemann. *Superconductivity*, volume 2, chapter 23, page 1415. Springer, 2008.

[82] S.-C. Zhang. A unified theory based on SO(5) symmetry of superconductivity and antiferromagnetism. *Science*, 275:1089, 1997.

[83] J. E. Hirsch. Two-dimensional Hubbard model: Numerical simulation study. *Phys. Rev. B*, 31(7):4403–4419, 1985.

[84] D. J. Scalapino. *Handbook of High-Temperature Superconductivity*, chapter 13, page 495. Springer, 2007.

[85] P. A. Lee. *Handbook of High-Temperature Superconductivity*, chapter 14, page 527. Springer, 2007.

[86] C. M. Varma, P. B. Littlewood, S. Schmitt-Rink, E. Abrahams, and A. E. Ruckenstein. Phenomenology of the normal state of Cu-O high-temperature superconductors. *Phys. Rev. Lett.*, 63(18):1996–1999, 1989.

[87] S. A. Kivelson and E. Fradkin. *Handbook of High-Temperature Supercondctivity*, chapter 15, page 570. Springer, 2007.

[88] S. A. Kivelson, I. P. Bindloss, E. Fradkin, V. Oganesyan, J. M. Tranquada, A. Kapitulnik, and C. Howald. How to detect fluctuating stripes in the high-temperature superconductors. *Rev. Mod. Phys.*, 75(4):1201–1241, Oct 2003.

[89] D.L. Feng, D.H. Lu, K.M. Shen, C. Kim, H. Eisaki, A. Damascelli, R. Yoshizaki, J.-i. Shimoyama, K. Kishio, G.D. Gu, S. Oh, A. Andrus, J. O'Donnell, J.N. Eckstein, and Z.-X. Shen. Signature of the superfluid density in the single-particle excitation spectrum of $Bi_2Sr_2CaCuO_{8+\delta}$. *Science*, 289:277, 2000.

[90] J. Fink, S. Borisenko, A. Kordyuk, A. Koitzsch, J. Geck, V. Zabalotnyy, M. Knupfer, B. Büchner, and H. Berger. *Dressing of the charge carriers in high-T_c superconductors*, volume 715 of *Lect. Notes Phys.*, chapter 11, page 295. Springer, 2008.

[91] V. P. Martovitsky, A. Krapf, and L. Dudy. Existence of two types of perfect $Bi_2Sr_{2-x}La_xCuO_{6+\delta}$ single crystals. *JETP Letters*, 85:292, 2007.

[92] H. W. Zandbergen, W. A. Groen, F. C. Mijhoff, G. Tendeloo, and S. Amelinckx. Models for the modulation in $A_2B_2Ca_nCu_{1+n}O_{6+2n}$, A,B=Bi, Sr or Tl, Ba and n= 0, 1, 2. *Physica C*, 156:325, 1988.

[93] H. W. Zandbergen, W. A. Groen, A. Smit, and G. Tendeloo. Structure and properties of $(Bi,Pb)_2Sr_2(Ca,Y)Cu_2O_{8+\delta}$. *Physica C*, 168:426, 1990.

[94] X. B. Kan and S. C. Moss. Four-dimensional crystallographic analysis of the incommensurate modulation in a $Bi_2Sr_2CaCu_2O_8$ single crystal. *Acta Crystallogr. B*, 48:122, 1992.

[95] C.C. Torardi, E.M. McCarron, P.L. Gai, J.B. Parise, J. Ghorohchian, D.B. Kang, M.-H. Whangbo, and J.C. Barry. Lead-doped $Bi_2Sr_2CuO_6$: a superconductor free of modulation and superstructure. *Physica C*, 176:347, 1991.

[96] H. Heinrich, G. Kostorz, B. Heeb, and L.J. Gauckler. Modelling the atomic displacements in $Bi_2Sr_2Ca_{n-1}Cu_nO_x$ superconductors. *Physica C*, 224:133, 1994.

[97] Mao Zhiqiang, Fan Chenggao, Shi Lei, Yao Zhen, Yang Li, Wang Yu, and Zhang Yuheng. Multiple $Bi_2Sr_{2-x}Ba_xCuO_y$ microstructures and the effect of element doping (Ba,La,Pb) on the 2:2:0:1 phase. *Phys. Rev. B*, 47(21):14467–14475, 1993.

[98] L. Dudy, B. Müller, B. Ziegler, A. Krapf, H. Dwelk, O. Lübben, R.-P. Blum, V.P. Martovitsky, C. Janowitz, and R. Manzke. Charge modulation driven Fermi surface of Pb-Bi2201. *Solid State Communications*, 143(8-9):442 – 445, 2007.

[99] O. Lübben, L. Dudy, A. Krapf, C. Janowitz, and R. Manzke. Structural behavior of (Pb,La)-Bi2201 depending on the lead content. *Phys. Rev. B*, 81:174112, 2010.

[100] S.H. Pan, J.P. O'Neal, R.L. Badzey, C. Chamon, H. Ding, J.R. Engelbrecht, Z. Wang, H. Eisaki, S. Uchida, A.K. Guptak, K.W. Ng, E.W. Hudson, K.M. Lang, and J.C. Davis. Microscopic electronic inhomogeneity in the high-T-c superconductor $Bi_2Sr_2CaCu_2O_{8+x}$. *Nature*, 413(6853):282–285, 2001.

[101] W. D. Wise, Kamalesh Chatterjee, M. C. Boyer, Takeshi Kondo, T. Takeuchi, H. Ikuta, Zhijun Xu, Jinsheng Wen, G. D. Gu, Yayu Wang, and E. W. Hudson. Imaging nanoscale Fermi-surface variations in an inhomogeneous superconductor. *Nature Physics*, 5:213, 2009.

[102] K. Fujita, T. Noda, K. M. Kojima, H. Eisaki, and S. Uchida. Effect of disorder outside the CuO_2 planes on T_c of copper oxide superconductors. *Physical Review Letters*, 95(9):097006, 2005.

[103] Z.-H. Pan, P. Richard, Y.-M. Xu, M. Neupane, P. Bishay, A. V. Fedorov, H. Luo, L. Fang, H.-H. Wen, Z. Wang, and H. Ding. Evolution of Fermi surface and normal-state gap in the chemically substituted cuprates $Bi_2Sr_{2-x}Bi_xCuO_{6+\delta}$. *Phys. Rev. B*, 79(9):092507, 2009.

[104] H. Eisaki, N. Kaneko, D. L. Feng, A. Damascelli, P. K. Mang, K. M. Shen, Z.-X. Shen, and M. Greven. Effect of chemical inhomogeneity in bismuth-based copper oxide superconductors. *Phys. Rev. B*, 69(6):064512, 2004.

[105] J. Heckel and P. Jugelt. Quantitative analysis of bulk samples without standards by using peak-to-.background ratios. *X-ray Spectrometry*, 13:159, 1984.

[106] S. Rogaschewski. HU Berlin.

[107] Stefan Hüfner. *Photoelectron Spectroscopy.* Springer Verlag, 1995.

[108] W. Schattke and M. A. Van Hove, editors. *Solid-State photoemission and related methods.* WILEY-VCH, 2003.

[109] J. C. Campuzano, M. R. Norman, and M. Randeria. *Photoemission in the High Tc Superconductors*, volume 2 of *Physics of superconductors*, pages 167–273. Springer Berlin, 2004. cond-mat/0209476.

[110] H. Hertz. Über einen Einfluss des ultravioletten Lichtes auf die elektrische Entladung. *Ann. Physik*, 31:938, 1887.

[111] A. Einstein. Über einen die Erzeugung und Verwandlung des Lichtes betreffenden heuristischen Gesichtspunkt. *Ann. Physik*, 17:132, 1905.

[112] C.N. Berglund and W.E. Spicer. Photoemission studies of copper and silver. *Phys. Rev.*, 136:1030, 1964.

[113] J.B. Pendry. Theory of photoemission. *Surface Science*, 57(2):679 – 705, 1976.

[114] G. D. Mahan. *Many-particle physics*. Plenum Press, 2000.

[115] W. Nolting. *Viel-Teilchen-Theorie*, volume 7 of *Grundkurs: Theoretische Physik*. Ulmen: Zimmermann-Neufang, 1992.

[116] N. V. Smith, P. Thiry, and Y. Petroff. Photoemission linewidths and quasiparticle lifetimes. *Phys. Rev. B*, 47(23):15476–15481, 1993.

[117] David W. Lynch and Clifford G. Olson. *Photoemission Studies of High-Temperature Superconductors*. Cambridge University Press, 1999.

[118] J.G. Chen. NEXAFS investigations of transition metal oxides, nitrides, carbides, sulfides and other interstitial compounds. *Surface Science Reports*, 30(1-3):1–152, 1997.

[119] F. de Groot. High resolution x-ray emission and x-ray absorption spectroscopy. *Chem. Rev.*, 101(6):1779–1808, 2001.

[120] Mau Hsiung Chen, Bernd Crasemann, and Vaclav O. Kostroun. Theoretical L_2-and L_3-subshell fluorescence yields and $L_2 - L_3$ x coster-kronig transition probabilities. *Phys. Rev. A*, 4(1):1–7, 1971.

[121] A. Bianconi. *X-ray absorption*, volume 92 of *Chemical Analysis*, chapter 11, page 573. Wiley, 1988.

[122] J. Fink, N. Nücker, E. Pellegrin, H. Romberg, M. Alexander, and M. Knupfer. Electron energy-loss and X-ray absorption spectroscopy of cuprate superconductors and related compounds. *J. Electron Spectr. and Rel. Phenom.*, 66:395, 1994.

[123] J. C. Fuggle and J. E. Inglesfield, editors. *Unoccupied electronic states*, volume 69 of *Topics in Applied Physics*. Springer-Verlag, 1992.

[124] F. deGroot and A. Kotani. *Core level spectroscopy of solids*. CRC Press, 2008.

[125] D. C. Koningsberger and R. Prins, editors. *X-ray absorption*, volume 92 of *Chemical Analysis*. Wiley, 1988.

[126] Center for X-ray Optics and Advanced Light Source and Lawrence Berkeley National Laboratory. X-ray Data Booklet.

[127] A. K. Ariffin, B Müller, R. Mitdank, L. Dudy, H. Dwelk, A. Krapf, C. Janowitz, and R. Manzke. The hole density of the CuO_2-layer of single crystals determined by XAS. *Phys. Rev. B*. submitted.

[128] D. D. Sarma, O. Strebel, C. T. Simmons, U. Neulirch, and G. Kaindl. Electronic structure of high-Tc superconductors from soft-x-ray absorption. *Phys. Rev. B*, 37:9784, 1988.

[129] N. Nücker, J. Fink, J. C. Fuggle, P. J. Durham, and W. M. Temmerman. Evidence for holes on oxygen sites in the high-Tc superconductors $La_{2-x}Sr_xCuO_4$ and $YBa_2Cu_3O_{7-y}$. *Phys. Rev. B*, 37(10):5158–5163, 1988.

[130] K. Okada, A. Kotani, B. T. Thole, and G. A. Sawatzky. Evidence of local singlet state in $NaCuO_2$ from Cu 2p x-ray absorption spectroscopy. *Solid State Comm.*, 77:835, 1991.

[131] A. Bianconi, A. Congui Castellano, M. De Santis, P. Rudolf, P. Lagarde, A. M. Flank, and A. Marcelli. $L_{2,3}$ Xanes of the high T_c superconductor $YBa_2Cu_3O_{\approx 7}$ with variable oxygen content. *Solid State Comm.*, 63:1009, 1987.

[132] A. Bianconi, J. Budnick, A. M. Flank, A. Fontaine, P. Lagarde, A. Marcelli, H. Tolentino, B. Chamberland, C. Michel, B. Raveau, and G. Demazeau. Evidence of $3d^9$-ligand hole states in the superconductor $La_{1.85}Sr_{0.15}CuO_4$ from L_3 x-ray absorption spectroscopy. *Phys. Lett. A*, 127:285, 1988.

[133] H. Eskes and G. A. Sawatzky. Doping dependence of high-energy spectral weights for the high-T_c cuprates. *Phys. Rev. B*, 43(1):119–129, 1991.

[134] Mark S. Hybertsen, E. B. Stechel, W. M. C. Foulkes, and M. Schlüter. Model for low-energy electronic states probed by x-ray absorption in high-T_c cuprates. *Phys. Rev. B*, 45(17):10032–10050, 1992.

[135] C. T. Chen, F. Sette, Y. Ma, M. S. Hybertsen, E. B. Stechel, W. M. C. Foulkes, M. Schulter, S-W. Cheong, A. S. Cooper, L. W. Rupp, B. Batlogg, Y. L. Soo, Z. H. Ming, A. Krol, and Y. H. Kao. Electronic states in $La_{2-x}Sr_xCuO_{4+\delta}$ probed by soft-x-ray absorption. *Phys. Rev. Lett.*, 66(1):104–107, 1991.

[136] H. Eskes, M. B. J. Meinders, and G. A. Sawatzky. Anomalous transfer of spectral weight in doped strongly correlated systems. *Phys. Rev. Lett.*, 67(8):1035–1038, 1991.

[137] Yoichi Ando, Y. Hanaki, S. Ono, T. Murayama, Kouji Segawa, N. Miyamoto, and Seiki Komiya. Carrier concentrations in $Bi_2Sr_{2-z}La_zCuO_{6+\delta}$ single crystals and their relation to the hall coefficient and thermopower. *Phys. Rev. B*, 61(22): R14956–R14959, 2000.

[138] Y. Dumont, C. Ayache, and G. Collin. Dragging excitation characteristics from thermoelectric power in $Bi_2(Sr_{2-y}La_y)CuO_6$ single crystals. *Phys. Rev. B*, 62(1): 622–625, 2000.

[139] B. C. Sales and B. C. Chakoumakos. Hole filling and hole creation in the superconducting compounds $Bi_2Sr_{2-x}R_xCuO_{6+y}$ (R=La, Pr, Nd, and Sm). *Phys. Rev. B*, 43(16):12994–13000, 1991.

[140] Maria Ronay, A. Santoni, A. G. Schrott, L. J. Terminello, S. P. Kowalczyk, and F. J. Himpsel. A new correlation for Tc from Cu 2p absorption. *Solid State Comm.*, 77:699, 1991.

[141] P. Ghigna, G. Spinolo, G. Flor, and N. Morgante. Correlation between hole density and oxygen excess in the $Bi_2Sr_2CaCu_2O_{8+\delta}$ superconductor. *Phys. Rev. B*, 57(21): 13426–13429, 1998.

[142] A. Q. Pham, F. Studer, N. Merrien, A. Maignan, C. Michel, and B. Raveau. Complex influence of the Bi-O reservoir and oxygen nonstoichiometry on the hole density in $Bi_2Sr_2CaCu_2O_8$. *Phys. Rev. B*, 48(2):1249–1253, 1993.

[143] N. Merrien, F. Studer, G. Poullain, C. Michel, A. M. Flank, P. Lagarde, and A. Fontaine. Redox mechanism and density of holes by XAS in the compensated series $Bi_{2-x}Pb_xSr_2Ca_{1-x}Y_xCu_2O_{8+\delta}$. *Journal of Solid State Chemistry*, 105:112, 1993.

[144] M. Schneider, R.-S. Unger, R. Mitdank, R. Muller, A. Krapf, S. Rogaschewski, H. Dwelk, C. Janowitz, and R. Manzke. Evolution of the density of states at the Fermi level of $Bi_{2-y}Pb_ySr_{2-x}La_xCuO_{6+\delta}$ and $Bi_2Sr_{2-x}La_xCuO_{6+\delta}$ cuprates with hole doping. *Physical Review B (Condensed Matter and Materials Physics)*, 72(1): 014504, 2005.

[145] D. C. Peets, D. G. Hawthorn, K. M. Shen, Young-June Kim, D. S. Ellis, H. Zhang, Seiki Komiya, Yoichi Ando, G. A. Sawatzky, Ruixing Liang, D. A. Bonn, and W. N. Hardy. X-ray absorption spectra reveal the inapplicability of the single-band hubbard model to overdoped cuprate superconductors. *Physical Review Letters*, 103(8):087402, 2009.

[146] E. Pellegrin, N. Nücker, J. Fink, S. L. Molodtsov, A. Gutiérrez, E. Navas, O. Strebel, Z. Hu, M. Domke, G. Kaindl, S. Uchida, Y. Nakamura, J. Markl, M. Klauda, G. Saemann-Ischenko, A. Krol, J. L. Peng, Z. Y. Li, and R. L. Greene. Orbital character of states at the Fermi level in $La_{2-x}Sr_xCuO_4$ and $R_{2-x}Ce_xCuO_4$ (r=nd,sm). *Phys. Rev. B*, 47(6):3354–3367, 1993.

[147] A. Bianconi, S. Della Longa, C. Li, M. Pompa, A. Congiu-Castellano, D. Udron, A. M. Flank, and P. Lagarde. Linearly polarized Cu L_3-edge x-ray-absorption near-edge structure of $Bi_2Sr_2CaCu_2O_8$. *Phys. Rev. B*, 44(18):10126–10138, 1991.

[148] N. L. Saini, D. S-L. Law, P. Pudney, K. B. Garg, A. A. Menovsky, and J. J. M. Franse. Evidence of redistribution of the itinerant holes below *Tc* in $Ba_2Sr_2CaCu_2O_8$ superconductors: A polarized x-ray-absorption study. *Phys. Rev. B*, 52(9):6219–6222, 1995.

[149] M. Abbate, M. Sacchi, J. J. Wnuk, L. W. M. Schreurs, Y. S. Wang, R. Lof, and J. C. Fuggle. Polarization dependence of the Cu 2p absorption spectra in $(Bi_{0.84}Pb_{0.16})_2Sr_2CaCu_2O_8$. *Phys. Rev. B*, 42(13):7914–7917, 1990.

[150] M. Merz, N. Nücker, P. Schweiss, S. Schuppler, C. T. Chen, V. Chakarian, J. Freeland, Y. U. Idzerda, M. Kläser, G. Müller-Vogt, and Th. Wolf. Site-specific x-ray absorption spectroscopy of $Y_{1-x}Ca_xBa_2Cu_3O_{7-y}$: Overdoping and role of apical

oxygen for high temperature superconductivity. *Phys. Rev. Lett.*, 80(23):5192–5195, 1998.

[151] A. R. Moodenbaugh, D. A. Fischer, Y. L. Wang, and Y. Fukumoto. Superconductivity, oxygen content, and hole state density in $Bi_2Sr_{1.75}Ca_{1.25}Cu_2O_{8.18+y}$ (-0.09<y≤0) and $Bi_{1.6}Pb_{0.4}Sr_{1.9}Ca_2Cu_3O_z$. *Physica C: Superconductivity*, 268(1-2):107 – 114, 1996.

[152] F. Studer, C. Gasser, L. Coudrier, H. Murray, M. Pompa, A.-M. Flank, and P. Lagarde. Hole density as seen by XAS and T_c's in the layered superconducting copper oxides. *Physica B*, 208+209:521, 1995.

[153] N.L. Saini, H. Oyanagi, M. Molle, K.B. Garg, C. Kim, and A. Bianconi. Evidence for anisotropic atomic displacements and orbital distribution in the inhomogenous CuO_2 plane of the $Bi_2Sr_2CaCu_2O_{8+\delta}$ system. *J Phys. Chem. Solids*, 65:1439, 2004.

[154] O.K. Andersen, E. Pavarini, I. Dasgupta, T. Saha-Dasgupta, and O. Jepsen. Band-structures of hole-doped cuprates; correlation with $T_{c,max}$. In *Proceedings of the 4th Asian Workshop on First-Principles Electronic Structure Calculations, Taipei, Taiwan*, 2001.

[155] Mao Zhiqiang, Xu Gaojie, Zhang Shuyuan, Tan Shun, Lu Bin, Tian Mingliang, Fan Chenggao, Xu Cunyi, and Zhang Yuheng. Relation of the superstructure modulation and extra-oxygen local-structural distortion in $Bi_{2.1-y}Pb_ySr_{1.9-x}La_xCuO_z$. *Phys. Rev. B*, 55(14):9130–9135, 1997.

[156] M. Schneider. *Photoemission and Röntgenabsorption zum Dotierungsverhalten der Bi-Hochtemperatur-Supraleiter*. PhD thesis, Humboldt University Berlin, 2005.

[157] A. Macridin, M. Jarrell, Th. Maier, and G. A. Sawatzky. Physics of cuprates with the two-band hubbard model: The validity of the one-band hubbard model. *Phys. Rev. B*, 71(13):134527, Apr 2005.

[158] H. Eskes, G.A. Sawatzky, and L.F. Feiner. Effective transfer for singlets formed by hole doping in the high-tc superconductors. *Physica C: Superconductivity*, 160 (5-6):424 – 430, 1989. ISSN 0921-4534.

[159] F. C. Zhang and T. M. Rice. Validity of the t-j model. *Phys. Rev. B*, 41(10): 7243–7246, Apr 1990. doi: 10.1103/PhysRevB.41.7243.

[160] J. Stöhr and R. Jaeger. Absorption-edge resonances, core-hole screening, and orientation of chemisorbed molecules: CO, NO, and N_2 on Ni(100). *Phys. Rev. B*, 26:4111, 1982.

[161] H. Ding, T. Yokoya, J. C. Campuzano, T. Takahashi, M. Randeria, M. R. Norman, T. Mochiku, K. Kadowaki, and J. Giapintzakis. Spectroscopic evidence for a pseudogap in the normal state of underdoped high-tc superconductors. *Nature*, 382:51, 1996.

[162] B. Bandyopadhyay and A. Poddar. Pseudogap in high-t_c cuprates. *J. of Alloys and Comp.*, 326:137, 2001.

[163] M. Karppinen, M. Kotiranta, T. Nakane, H. Yamauchi, S. C. Chang, R. S. Liu, and J. M. Chen. Layer-specific hole concentrations in $bi2sr2(y1 - xcax)cu2o8 + \delta$ as probed by xanes spectroscopy and coulometric redox analysis. *Phys. Rev. B*, 67 (13):134522, Apr 2003.

[164] T. Valla, P.D. Johnson, Z. Yusof, B. Wells, Q. Li, S.M. Loureiro, R.J. Cava, M Mikami, Y. Mori, M. Yoshimura, and T. Sasaki. Coherence-incoherence and dimensional crossover in layered strongly correlated materials. *Nature*, 417:627, 2002.

[165] H. Ding, J. R. Engelbrecht, Z. Wang, J. C. Campuzano, S.-C. Wang, H.-B. Yang, R. Rogan, T. Takahashi, K. Kadowaki, and D. G. Hinks. Coherent quasiparticle weight and its connection to high- T_c superconductivity from angle-resolved photoemission. *Phys. Rev. Lett.*, 87(22):227001, 2001.

[166] R. H. He, D. L. Feng, H. Eisaki, J.-I. Shimoyama, K. Kishio, and G. D. Gu. Superconducting order parameter in heavily overdoped $Bi_2Sr_2CaCuO_{8+\delta}$: a global quantitative analysis. *Phys. Rev. B*, 69(22):220502, 2004.

[167] A. A. Kordyuk, S. V. Borisenko, T. K. Kim, K. A. Nenkov, M. Knupfer, J. Fink, M. S. Golden, H. Berger, and R. Follath. Origin of the peak-dip-hump line shape in the superconducting-state $(\pi, 0)$ photoemission spectra of $Bi_2Sr_2CaCuO_8$. *Phys. Rev. Lett.*, 89(7):077003, 2002.

[168] R. Manzke, R. Müller, C. Janowitz, M. Schneider, A. Krapf, and H. Dwelk. Fine-structure in the low-energy excitation spectrum of a high-T_c superconductor by polarization-dependent photoemission. *Phys. Rev. B*, 63:100504(R), 2001.

[169] C. Janowitz, R. Müller, L. Dudy, R.-St. Unger, A. Krapf, R. Manzke, C. Ast, and H. Höchst. Progress in the understanding of the normal state of the cuprates. *Applied Phys. A*, 76:673, 2003.

[170] Z. X. Shen and D. S. Dessau. Electronic structure and photoemission studies of late transition-metal oxides – mott insulators and high-temperature superconductors. *Physics Reports*, 253(1-3):1 – 162, 1995.

[171] M.R. Norman, M. Randeira, H. Ding, and J.C. Campuzano. Phenomenological models for the gap anisotropy of $Bi_2Sr_2CaCu_2O_8$ as measured by angle-resolved photoemission spectroscopy. *Phys. Rev. B*, 52:615, 1995.

[172] W. B. Peatman, J. Bahrdt, F. Eggenstein, G. Reichardt, and F. Senf. The exactly focusing spherical grating monochromator for undulator radiation at bessy. *Review of Scientific Instruments*, 66(4):2801–2806, 1995.

[173] A.I. Liechtenstein, O. Gunnarsson, O.K. Andersen, and R.M. Martin. Quasiparticle bands and superconductivity in bilayer cuprates. *Phys. Rev. B*, 54:12505, 1996.

[174] Sudip Chakravarty, Asle Sudbo, Philip W. Anderson, and Steven Strong. Interlayer Tunneling and Gap Anisotropy in High-Temperature Superconductors. *Science*, 261(5119):337–340, 1993.

[175] H. Ding, A.F. Bellman, J.C. Campuzano, M. Randeira, M.R. Norman, T. Yokoya, T. Takahashi, H. Katayama-Yoshida, T. Mochiku, K. Kadowaki, G. Jennings, and G.P. Brivio. Electronic excitations in $Bi_2Sr_2CaCuO_{8+\delta}$: Fermi surface, dispersion, and absence of bilayer splitting. *Phys. Rev. Lett.*, 76:1533, 1996.

[176] D. L. Feng, N. P. Armitage, D. H. Lu, A. Damascelli, J. P. Hu, P. Bogdanov, A. Lanzara, F. Ronning, K. M. Shen, H. Eisaki, C. Kim, Z.-X. Shen, J.-i. Shimoyama, and K. Kishio. Bilayer splitting in the electronic structure of heavily overdoped $Bi_2Sr_2CaCuO_{8+\delta}$. *Phys. Rev. Lett.*, 86(24):5550–5553, 2001.

[177] Y.-D. Chuang, A. D. Gromko, A. Fedorov, Y. Aiura, K. Oka, Yoichi Ando, H. Eisaki, S. I. Uchida, and D. S. Dessau. Doubling of the bands in overdoped $Bi_2Sr_2CaCuO_{8+\delta}$: evidence for c-axis bilayer coupling. *Phys. Rev. Lett.*, 87(11): 117002, 2001.

[178] D. L. Feng, C. Kim, H. Eisaki, D. H. Lu, A. Damascelli, K. M. Shen, F. Ronning, N. P. Armitage, N. Kaneko, M. Greven, J.-i. Shimoyama, K. Kishio, R. Yoshizaki, G. D. Gu, and Z.-X. Shen. Electronic excitations near the brillouin zone boundary of $Bi_2Sr_2CaCuO_{8+\delta}$. *Phys. Rev. B*, 65(22):220501, 2002.

[179] S. V. Borisenko, A. A. Kordyuk, T. K. Kim, A. Koitzsch, M. Knupfer, J. Fink, M. S. Golden, M. Eschrig, H. Berger, and R. Follath. Anomalous enhancement of the coupling to the magnetic resonance mode in underdoped Pb-Bi2212. *Phys. Rev. Lett.*, 90(20):207001, 2003.

[180] A. A. Kordyuk, S. V. Borisenko, M. S. Golden, S. Legner, K. A. Nenkov, M. Knupfer, J. Fink, H. Berger, L. Forró, and R. Follath. Doping dependence of the Fermi surface in $(Pb, Bi)_2Sr_2CaCuO_{8+\delta}$. *Phys. Rev. B*, 66(1):014502, 2002.

[181] S. V. Borisenko, A. A. Kordyuk, T. K. Kim, S. Legner, K. A. Nenkov, M. Knupfer, M. S. Golden, J. Fink, H. Berger, and R. Follath. Superconducting gap in the presence of bilayer splitting in underdoped $(Pb, Bi)_2Sr_2CaCu_2O_{8+\delta}$. *Phys. Rev. B*, 66(14):140509, 2002.

[182] M. Lindroos, R. S. Markiewicz, and A. Bansil. Special photon energies for extracting the bosonic spectral function mediating superconductivity in $Bi_2Sr_2CaCuO_{8+}$ via angle-resolved photoemission spectroscopy. *Phys. Rev. B*, 69(14):140505, 2004.

[183] A. Bansil, M. Lindroos, S. Sahrakorpi, and R. S. Markiewicz. Role of site selectivity, dimensionality, and strong correlations in angle-resolved photoemission from cuprate superconductors. *New Journal of Physics*, 7(1):140, 2005.

[184] D. Orgad, S. A. Kivelson, E. W. Carlson, V. J. Emery, X. J. Zhou, and Z. X. Shen. Evidence of electron fractionalization from photoemission spectra in the high temperature superconductors. *Phys. Rev. Lett.*, 86(19):4362–4365, May 2001.

[185] K. Byczuk, C. Janowitz, R. Manzke, J. Spalek, and W. Wojcik. Luttinger-liquid phenomenology and angle-resolved photoemission for single-layer $Bi_2Sr_{2-x}La_xCuO_{6+\delta}$ high-temperature superconductor. *EPL (Europhysics Letters)*, 67(6):1011, 2004.

[186] D.A. Shirley. High-resolution x-ray photoemission spectrum of the valence bands of gold. *Phys. Rev. B*, 5:4709, 1972.

[187] D. L. Feng. *Electronic structure of the bismuth familiy of high temperature superconductors*. PhD thesis, Stanford University, 2001.

[188] Yoichi Ando, Kouji Segawa, Seiki Komiya, and A. N. Lavrov. Electrical resistivity anisotropy from self-organized one dimensionality in high-temperature superconductors. *Phys. Rev. Lett.*, 88(13):137005, Mar 2002.

[189] M. Fujita, H. Goka, K. Yamada, and M. Matsuda. Competition between charge- and spin-density-wave order and superconductivity in $La_{1.875}Ba_{0.125-x}Sr_xCuO_4$. *Phys. Rev. Lett.*, 88(16):167008, Apr 2002.

[190] J. M. Tranquada, B. J. Sternlieb, J. D. Axe, Y. Nakamura, and S. Uchida. Evidence for stripe correlations of spins and holes in copper oxide. *Nature*, 365:561, 1995.

[191] H. A. Mook, Pengcheng Dai, and F. Doğan. Charge and spin structure in $YBa_2Cu_3O_{6.35}$. *Phys. Rev. Lett.*, 88(9):097004, Feb 2002.

[192] C. Janowitz, V. Scherer, B. Müller, L. Dudy, A. Krapf, H. Dwelk, and R. Manzke. Evidence for static site centered stripe order by photoemission on $Bi_2Sr_{1.2}La_{0.8}CuO_{6+\delta}$. *Phys. Rev. Lett.* submitted.

[193] E. W. Carlson, D. Orgad, S. A. Kivelson, and V. J. Emery. Dimensional crossover in quasi-one-dimensional and high-Tc superconductors. *Phys. Rev. B*, 62(5):3422–3437, Aug 2000.

[194] J. Voit. One-dimensional fermi liquids. *Reports on Progress in Physics*, 58(9):977, 1995.

[195] Steven A. Kivelson, Daniel S. Rokhsar, and James P. Sethna. Topology of the resonating valence-bond state: Solitons and high-Tc superconductivity. *Phys. Rev. B*, 35(16):8865–8868, Jun 1987.

[196] Patrick A. Lee, Naoto Nagaosa, and Xiao-Gang Wen. Doping a Mott insulator: Physics of high-temperature superconductivity. *Rev. Mod. Phys.*, 78(1):17–85, Jan 2006.

[197] T. Senthil and Patrick A. Lee. Coherence and pairing in a doped Mott insulator: Application to the cuprates. *Phys. Rev. Lett.*, 103(7):076402, Aug 2009.

[198] P. D. Johnson and T. Valla. *Photoemission as probe of the collective excitations in condenced matter systems*, volume 715 of *Lect. Notes Phys.*, chapter 3, page 55. Sringer, 2007.

[199] J. Wei, Y. Zhang, H. W. Ou, B. P. Xie, D. W. Shen, J. F. Zhao, L. X. Yang, M. Arita, K. Shimada, H. Namatame, M. Taniguchi, Y. Yoshida, H. Eisaki, and D. L. Feng. Superconducting coherence peak in the electronic excitations of a single-layer $Bi_2Sr_{1.6}La_{0.4}CuO_{6+\delta}$ cuprate superconductor. *Phys. Rev. Lett.*, 101 (9):097005, Aug 2008.

[200] A. D. Gromko, A. V. Fedorov, Y.-D. Chuang, J. D. Koralek, Y. Aiura, Y. Yamaguchi, K. Oka, Yoichi Ando, and D. S. Dessau. Mass-renormalized electronic excitations at $(\pi, 0)$ in the superconducting state of $Bi_2Sr_2CaCu_2O_{8+\delta}$. *Phys. Rev. B*, 68(17):174520, Nov 2003.

[201] A. Kaminski, M. Randeria, J. C. Campuzano, M. R. Norman, H. Fretwell, J. Mesot, T. Sato, T. Takahashi, and K. Kadowaki. Renormalization of spectral line shape and dispersion below T_c in $Bi_2Sr_2CaCu_2O_{8+\delta}$. *Phys. Rev. Lett.*, 86(6):1070–1073, Feb 2001.

[202] T. Cuk, F. Baumberger, D. H. Lu, N. Ingle, X. J. Zhou, H. Eisaki, N. Kaneko, Z. Hussain, T. P. Devereaux, N. Nagaosa, and Z.-X. Shen. Coupling of the B_{1g} phonon to the antinodal electronic states of $Bi_2Sr_2Ca_{0.92}Y_{0.08}Cu_2O_{8+\delta}$. *Phys. Rev. Lett.*, 93(11):117003, Sep 2004.

[203] T. K. Kim, A. A. Kordyuk, S. V. Borisenko, A. Koitzsch, M. Knupfer, H. Berger, and J. Fink. Doping dependence of the mass enhancement in $(Pb, Bi)_2Sr_2CaCu_2O_8$ at the antinodal point in the superconducting and normal states. *Phys. Rev. Lett.*, 91(16):167002, Oct 2003.

Danksagung

Publications

Publications in International Journals

- **B. Müller**, L. Dudy, C. Janowitz and R. Manzke
  Comment on "Superconducting Coherence Peak in the Electronic Excitations of a Single-Layer $Bi_2Sr_{1.6}La_{0.4}CuO_{6+\delta}$"
  Phys. Rev. Lett. 103, 109701 (2009)

- B. Ziegler, **B. Müller**, A. Krapf, H. Dwelk, C. Janowitz and R. Manzke
  Coupling to a phononic mode in $Bi_{2-x}Pb_xSr_2CaCu_2O_{8+\delta}$: Angle-resolved photoemission
  Phys. Rev. B 77, 054520 (2008)

- J. C. E. Rasch, T. Stemmler, **B. Müller**, L. Dudy and R. Manzke
  1T-TiSe$_2$: Semimetal or Semiconductor?
  Phys. Rev. Lett. 101, 237602 (2008)

- L. Dudy, **B. Müller**, B. Ziegler, A. Krapf, H. Dwelk, Lübben, R.-P Blum, V. P. Martovitsky, C. Janowitz and R. Manzke
  Charge modulation driven Fermi surface of Pb-Bi2201
  Solid State Communications 143, 442 (2007)

Conference Proceedings

- A. K. Ariffin, C. Janowitz, **B. Müller**, L. Dudy, P. Sippel, R. Mitdank, H. Dwelk, A. Krapf, and R. Manzke
  Hole doping in the CuO_2-plane of Bi-cuprates studied by XAS: Polycrystals and single crystals
  Journal of Physics: Conference Series 150, 052084 (2009)

- L. Dudy, C. Janowitz, O. Lübben, **B. Müller**, A. K. Ariffin, A. Krapf, H. Dwelk and R. Manzke
  Structure, superstructure and charge order in Bi-cuprates
  J. Supercond. and Nov. Magn. 22(1), 51 (2009)

Submitted Publications and Publications in Preparation

- A. K. Ariffin, **B. Müller**, R. Mitdank, L. Dudy, H. Dwelk, A. Krapf, C. Janowitz and R. Manzke
  The hole density of the CuO_2-layer of single crystals determined by XAS
  Phys. Rev. B, submitted

- C. Janowitz, V. Scherer, **B. Müller**, L. Dudy, A. Krapf, H. Dwelk, R. Manzke, T. Okuda and A. Kakizaki
  Evidence for static, site centered stripe order by photoemission on $Bi_2Sr_{1.2}La_{0.8}CuO_{6+\delta}$
  Phys. Rev. Lett, submitted

- **B. Müller**, A.K. Ariffin, R. Mitdank, L. Dudy, J. C. E. Rasch, B. Ziegler, A. Krapf, C. Janowitz and R. Manzke
  Polarization dependent x-ray absorption of the CuO_2-layer of Bi(Pb)-2201
  in preparation

- **B. Müller**, L. Dudy, H. Dwelk, A. Krapf, C. Janowitz and R. Manzke
  Antinodal excitations at the Fermi surface of double layered Bi-cuprates studied by ARPES
  in preparation

Selbständigkeitserklärung

Hiermit versichere ich, die vorliegende Arbeit selbständig und ohne unerlaubte fremde Hilfe angefertigt zu haben. Ich versichere, mich nicht anderweitig um einen Doktorgrad beworben zu haben. Die dem Verfahren zu Grunde liegende Promotionsordnung der Mathematisch-Naturwissenschaftlichen Fakultät I der Humboldt-Universität zu Berlin habe ich zur Kenntnis genommen.

Berlin, den ───────────────